Technical University of Munich
Department of Civil, Geo and Environmental Engineering
Deutsches Geodätisches Forschungsinstitut (DGFI-TUM)
Prof. Dr.-Ing. habil. Florian Seitz

Nominal and observation-based attitude realization for precise orbit determination of the Jason satellites

Zeitlhöfler, Julian

Master's Thesis

Master's Course in Geodesy and Geoinformation

Supervisor(s)

Dr.-Ing. Mathis Bloßfeld
Deutsches Geodätisches Forschungsinstitut (DGFI-TUM)
Technical University of Munich

Prof. Dr.-Ing. habil. Florian Seitz
Deutsches Geodätisches Forschungsinstitut (DGFI-TUM)
Technical University of Munich

June 21, 2019

I confirm that this Master's Thesis is my own work and that I have documented all sources and material used.

Munich, June 21, 2019

Location, Date

Signature

Abstract

Geodetic satellites are a main contributor of today's monitoring of our planet. Highly accurate satellite measurements require precise satellite orbits. In this thesis, the influence of using attitude observations in contrast to a nominal yaw steering model for the Precise Orbit Determination (POD) of the three Jason satellites is investigated. The daily available attitude observation data, composed of satellite attitude quaternions and solar panel rotation angles, is analyzed and combined to weekly attitude files. The extensive and necessary preprocessing includes the detection and elimination of outliers, data resampling and the optimal interpolation of missing data. Orbits based on Satellite Laser Ranging (SLR) observations to the satellites Jason-1, Jason-2 and Jason-3 are computed for an overall timespan of approximately 25 years. Within the orbit analysis, observation outliers and maneuvers are removed. The revised orbits are recalculated using either the nominal yaw steering model for the realization of the attitude or the observation-based approach. The comparison of the resulting orbits shows an improvement in the overall mission Root Mean Square (RMS) of SLR residuals of 5.93 % (Jason-1), 8.27 % (Jason-2) and 4.51 % (Jason-3) from nominal to observed attitude realization. About 75 % of all orbital arcs calculated with the observation data result in a smaller RMS. POD-related parameters show a better coincidence with the target values in case of observation-based orbits. Orbit solutions of the GeoForschungsZentrum Potsdam (GFZ) and Centre National D'Etudes Spatiales (CNES) – both use a combination of geodetic tracking techniques which increases the orbit accuracy – are used for external orbit determination. This comparison shows an approximately 10 % better coincidence with observation-based orbits than in the nominal case. Additionally, the influence of the preprocessed orbits on estimated SLR station coordinates is investigated. The orbit characteristic draconitic period is clearly reduced in the station coordinates when using observation-based attitude data.

Zusammenfassung

Geodätische Satelliten sind heutzutage ein wichtiger Bestandteil der Erdbeobachtung. Hochgenaue Messungen der Erdoberfläche setzen dabei eine präzise Bestimmung des Satellitenorbits voraus. In dieser Arbeit werden die Einflüsse einer nominell modellierten Satellitenorientierung im Gegensatz zu einer beobachtungsbasierten Lagerealisierung auf die Satellitenbahn untersucht. Die beobachtete Satellitenlage, bestehend aus Lagequaternionen der Satellitenplattform und Rotationswinkeln beider Solarpanele, werden in einem Vorverarbeitungsschritt analysiert und von täglichen zu wöchentlichen Dateien zusammengeführt. Die aufwendige, aber notwendige Vorverarbeitung beinhaltet die Detektion und Entfernung von Ausreißern, ein Resampling der Daten und eine optimale Interpolation von fehlenden Epochen. Es werden Orbits der Satelliten Jason-1, Jason-2 und Jason-3 über einen Zeitraum von insgesamt etwa 25 Jahren unter Verwendung von Satelliten-Laserentfernungsmessungen (SLR) berechnet. Dabei werden Ausreißer in den Beobachtungen und Orbitmanöver entfernt. Die optimierten Bögen ermöglichen eine erneute Berechnung der Orbits mit entweder nominell modellierter Satellitenorientierung oder unter der Verwendung der beobachteten Satellitenlage. Der Vergleich der Orbits zeigt eine Verbesserung der Orbitgenauigkeit von nominell zu beobachtungsbasierter Lagerealisierung von 5.93 % (Jason-1), 8.27 % (Jason-2) und 4.51 % (Jason-3). Etwa 75 % aller Orbitbögen weisen eine höhere Orbitgenauigkeit auf. Parameter, welche bei den Orbitberechnungen geschätzt werden, zeigen größere Übereinstimmungen mit den Sollwerten bei Orbits unter Verwendung der beobachteten Satellitenlage. Zur externen Validierung der Satelitenorbits werden Lösungen des Geoforschungszentrums Potsdam (GFZ) und der französischen Raumfahrtagentur CNES verwendet. Beide Berechnungszentren verwenden zur Orbitberechnung eine Kombination aus geodätischen Satellitenpositionierungstechniken, aufgrund dessen die Satellitenposition genauer bestimmt werden kann. Der Vergleich beider Orbitrealisierungen des Deutsches Geodätisches Forschungsinstitut (DGFI-TUM) mit den externen Orbits zeigt eine Verringerung der Positionsdifferenzen um etwa 10 % unter Verwendung von Lagebeobachtungen. Zusätzlich wird der Einfluss der Orbits auf die Schätzung von Koordinaten einger SLR Stationen untersucht. Dabei kann eine Reduzierung der drakonitischen Periode (charakteristisch für den Satellitenorbit) festgestellt werden.

Contents

1 Introduction

Satellites are the fundament of modern Earth observation and extend the former mainly local monitoring of environmental effects to a global scale. Satellite geodesy – the science of measurement and mapping the surface of the Earth using measurements to, from, or between artificial satellites (Seeber, 2003) – provides important information for a better understanding of our planet and gives valid insight into the dynamic processes on the Earth's crust and in the Earth's interior and exterior. Various other geoscientific disciplines rely on geodetic satellite data and the derived products which are subsequently used for the development of local and global models. Satellite data is not only of scientific importance but also supports substantial arguments for political and social decisions.

Today, we are using satellites for Earth observation, navigation, communication, weather prediction and other applications. A requirement of Earth observation missions is the precise determination of the satellite orbit (POD, Precise Orbit Determination). Measurements of, e.g., the Earth's topography, gravity field or magnetic field rely on an accurate computation of the satellite position. Each mistake in the coordinates – especially in the radial satellite component – affects the derived (geophysical) parameters. Consequently, undetected orbit errors are fully included in the parameter computation. Errors in the altitude of, for example, altimetry satellites directly influence the derived sea surface height.

Due to the current climate change, altimetric measurements and products are of increasing importance. Both, eustatic and thermosteric sea level changes provoke increasing challenges for islands and coastal regions. The long-term global mean sea level rise is between 3 and 4 mm per year. It is obvious that effects of this magnitude require even more accurate satellite orbits.

In early days, the orbit accuracy of GEOS 3 was at the level of about 100 cm. Improvements in background models (e.g., Earth gravity field, solar radiation pressure), enhanced sensor performance and advanced computation techniques increased the accuracy of the POD for such satellites to the decimeter level (ERS-1). Since the early 2000s, an orbit accuracy at the centimeter level (Jason-1) was achieved. The progress in POD accuracy of altimetry satellites until current missions is illustrated in Figure 1.

POD is an essential prerequisite of nadir-directed altimeter range measurements. The third Kepler law ensures a very stable radial orbit component of a satellite in a (nearly) circular orbit (Stammer and Cazenave, 2017). To reduce the risk of orbit errors in the along- and cross-track direction, precise modeling of disturbing forces has to be considered in POD. The magnitude of these effects depends on various circumstances. Gravitational effects are coupled with the distance between the satellite and other celestial objects. Non-gravitational forces interact with the surfaces of the spacecraft and are linked to both, the altitude of the satellite and, to an even bigger extent, the orientation/attitude of the satellite in space. Surface forces can cause an acceleration as well as a deceleration of the satellite.

Thus, the precise satellite attitude is an essential requirement for the accurate calculation and the modelling of the impact of surface forces acting on the satellite. The cross-sectional area of non-spherical satellites, which is

affected by these forces, is varying along the orbit around the Earth and can only be modelled accurately if the attitude of the satellite is known. Beside the satellite body itself, the effective area comprises solar arrays which offer a comparably large influence area to surface forces. Therefore, the rotational orientation of both, the main body and the solar arrays, with respect to the direction of the acting forces is an important aspect for an accurate calculation of the accelerations.

The altimetry satellites Jason-1, Jason-2 and Jason-3 are used in this work to validate the orbit via two different approaches. In the first calculation, the attitude is realized by a model which represents the intended nominal attitude of the satellites. The second method uses observation-based quaternions and solar panel rotation angles which nearly provide the instantaneously observed orientation of the spacecraft. In this thesis, the computed satellite orbits are based on the analysis of laser ranging observations.

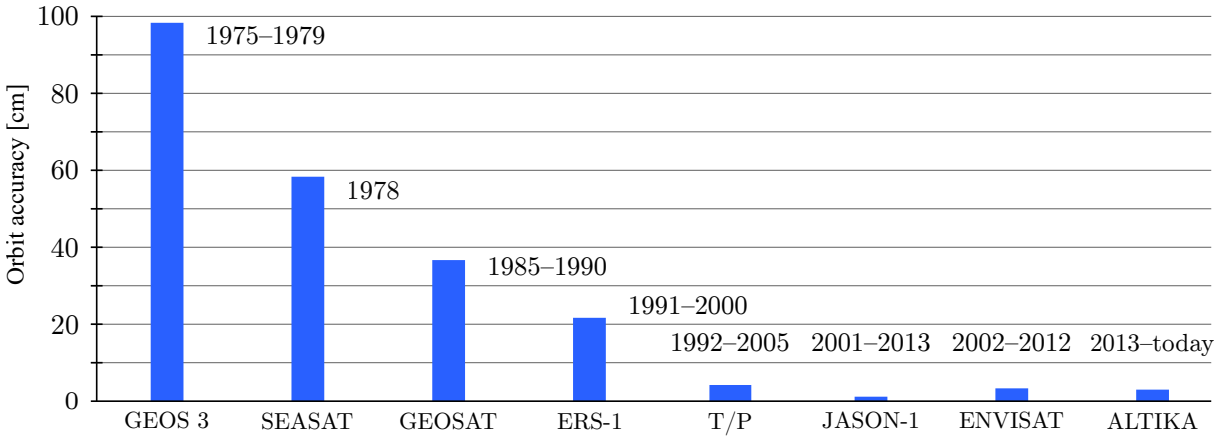

Figure 1: Development of the orbit accuracy of altimetry satellites.[1]

The Jason satellites suit this investigation in consideration of several aspects. Due to instrument payload and two laterally protruding solar arrays, the spacecraft geometry is quite complex. All significant surface forces interact with the satellite in the orbit height of about 1336 km. The impact of the atmosphere density is considerably large, and a major fraction of the satellite surfaces is exposed to solar radiation due to the continuous Sun-pointing orientation of the solar arrays. The satellites are daily tracked by a worldwide SLR (Satellite Laser Ranging) station network which provides good coverage of satellite observations for the orbit determination (Pearlman et al., 2002).

Continually improved standards of satellite-based products require constantly enhanced approaches in precise orbit determination. Thus, the above discussed issues lead to the main research question of this thesis:

> **Are attitude observations helpful to further improve the precise orbit determination of near-Earth satellites?**

To answer this question, the thesis is structured as follows. At first, the theoretical background of reference systems, attitude representation and precise orbit determination is provided (Chapter 2). Orbital, spacecraft and attitude characteristics of the chosen satellites are outlined in Chapter 3. Chapter 4 explains the preprocessing of attitude quaternions and solar panel angles and the usage of the data within the precise orbit determination. Chapter 5 provides a discussion of several obtained results and quantifies the impact of the different attitude modelling approaches on derived geodetic parameters. Finally, Chapter 6 concludes this thesis and illustrates further work in precise orbit determination and the benefit of the investigation for other disciplines.

[1] Original from Stammer and Cazenave (2017)

2 Theory

This chapter provides the theoretical background for precise orbit determination. First, the required reference systems, which represent the fundamental prerequisite of attitude determination, are explained in Chapter 2.1. Different parametrizations, their advantages and limitations, and interpolation methods are given in Chapter 2.2. Chapter 2.3 outlines perturbing forces which interact with the satellite and have to be taken into account in precise orbit determination. The geodetic observation technique SLR, which is used for the tracking of the satellites Jason-1, Jason-2 and Jason-3 within this thesis, is outlined in Chapter 2.4.

2.1 Reference systems

A fundamental requirement of satellite orbit determination is the definition of necessary coordinate systems. The following sections describe all coordinate systems used in this thesis to realize the determination of a satellite's orientation in space. First, the inertial reference system, in which the positions of a satellite are given, is defined. Afterwards, satellite specific coordinate systems are explained. All coordinate systems are 3-dimensional, rectangular and right-handed. An overview of the described systems is provided in Table 1.
Note: A reference system is defined by theoretical conventions and the modeling requirements to obtain, at any time, an n-dimensional pod of unit vectors. A reference frame is the realization of the theoretically defined reference system by observations or other specifications like basic assumptions or datum constraints.

2.1.1 Inertial reference system

The orbit determination of a satellite requires a reference coordinate system in which the position of the satellite can be expressed. Due to the motion of satellites around the Earth, a geocentric reference system fits best for this application. Furthermore, the system should not rotate with respect to the mean positions of the stars but be fixed (inertial or quasi-inertial) and the positions of celestial sources shall define the system. The positions of celestial sources are obtained from Very Long Baseline Interferometry (VLBI) measurements.

The plane of the Earth's mean elliptical orbit around the Sun is known as *ecliptic* (Vallado and McClain, 2007). The Earth's rotation axis is not perpendicular to the ecliptic but tilted with an angle of about 23.5° (see Figure 2). This angle is called *obliquity of the ecliptic* ε. Thus, the plane of the Earth's mean equator and the ecliptic intersect in one line (*line of nodes*). The points of this line on the ecliptic – and simultaneously on the equatorial plane – are called equinoctial points and form the reference points on the fundamental plane. The fundamental plane of the International Celestial Reference System (ICRS) is the Earth's mean equator. The point where the ecliptic crosses the equatorial plane from South to North is known as *vernal equinox* Υ (or spring equinox or First Point of Aries (Taff, 1985)). The second point is called autumnal equinox (transit of the ecliptic from North to South). These two events occur near March 20 and September 23, respectively.

Due to the interaction of external forces with the Earth, celestial coordinate systems are not entirely inertial. The gravitational impact of the Moon and the Sun on the Earth causes a torque which results in a slow rotation of the Earth's spin axis about the ecliptic pole (a full rotation of 360° in approximately 25700 years) (Wertz, 2002). Furthermore, this provokes a movement of the reference points along the ecliptic (~50 arcseconds per year), also known as *precession of the equinoxes*.

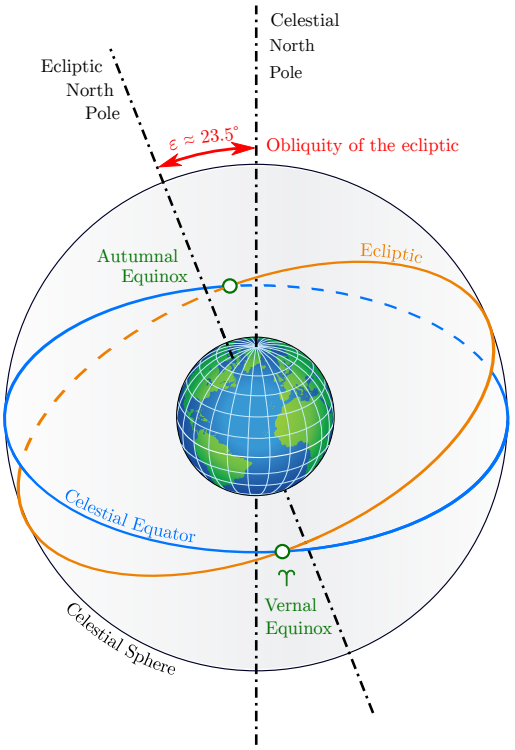

Figure 2: Orientation of the Earth in space: the plane defined by the Earth's orbit around the Sun is called ecliptic. This plane is tilted by about 23.5° (obliquity of the ecliptic) toward the equatorial plane. The intersections of both planes on the celestial sphere define the equinoctial points.[2]

The principal direction of the ICRS is defined by the vernal equinox. Due to the slight change of the equinoctial points a temporal definition of the ICRS is necessary for the precise determination of the coordinates of celestial bodies. In the following, the system at epoch J2000.0[3] is used as the ICRS. It is defined by the International Earth Rotation and Reference Systems Service (IERS) and specifies the Earth's mean equator and mean rotational axis at that epoch (Petit and Luzum, 2010). The origin of the coordinate system is the barycenter of the solar system. According to Arias et al. (1995), the ICRS at epoch J2000.0 fulfills the recommendations of the International Astronomical Union (IAU) and is consistent with the system at that epoch which is defined by the Fifth Fundamental Catalogue (FK5).

To obtain a geocentric reference frame, the ICRS is moved from the barycenter of the Solar System to the Earth's Center of Mass (CoM). The result is called Geocentric Celestial Reference System (GCRS). The GCRS experiences slight accelerations due to the motion of the Earth about the Sun. Hence, the GCRS is known as a quasi-inertial system.

According to the above-mentioned criteria, the direction of the vernal equinox at epoch J2000.0 represents axis X_{GCRS}, the Earth's mean rotation axis at that epoch forms Z_{GCRS}, and Y_{GCRS} completes the right-handed orthogonal coordinate system.

2.1.2 Orbital reference system

During the satellite's motion around the Earth, an imaginary orbital reference system accompanies the satellite. Its origin is located in the satellite's center of mass. According to Vallado and McClain (2007), the X_{ORB} axis points from the Earth's center along the radius vector towards the satellite (reverse geocentric pointing). The Z_{ORB} axis is the normal to the satellite's orbital plane (same direction as the orbital angular momentum),

[2] Globe from `https://upload.wikimedia.org/wikipedia/commons/b/b1/Globe_Atlantic.svg`), Last access: 2019-06-19

[3] J2000.0 0.0 = JD 2451545.0 = January 1, 2000, $12^h\ 0^m\ 0^s$ TDB = January 1, 2000, $11^h\ 58^m\ 55.816^s$ UTC (Urban and Seidelmann, 2012)

and the Y_{ORB} axis is perpendicular to the radius vector and points towards the flight direction of the satellite (see Figure 4). The latter axis is not necessarily parallel to the velocity vector. Y_{ORB} and the velocity vector only coincide in the case of circular orbits and the apogee and perigee of elliptical orbits. This coordinate system is primarily used for the determination of relative satellite positions and for the comparison of satellite orbits. Radial displacements are represented in differences along the X_{ORB} axis, along-track (or transverse) displacements are described along the Y_{ORB} axis and cross-track (or normal) displacements along the Z_{ORB} axis. In the literature, this coordinate system is also referred to as RTN system (radial, transverse, normal). Note that along-track differences are along (in the same direction as) the velocity vector, in-track differences are parallel to the velocity vector.

2.1.3 Local orbital reference system

A local orbital or roll-pitch-yaw (RPY) reference system is used for the analysis of orbital errors, in attitude dynamics (like in airplanes), and instrument pointing of satellite payload. As the orbital reference system described in the previous section, this tripod of axes is following the spacecraft in its orbit, too. The origin of the system is the satellite center of mass. According to the chosen mode of satellite pointing, the axes are oriented slightly different. In this thesis, we have to distinguish between a geocentric and a geodetic pointing system. In the first case, the yaw axis is always directed towards the center of the Earth. The pitch axis is the negative Z_{ORB} of the RTN system axis (normal to the orbital plane and opposite of the angular momentum) and the roll axis coincides with the RTN Y_{ORB} axis (again, the axis it not necessarily parallel to the velocity vector).

In the geodetic mode, the yaw axis is oriented towards the Earth (nadir-pointing) and is always perpendicular to the imaginary tangential plane through the piercing point on the reference ellipsoid (compare Figure 3). The angular difference of the yaw direction between both pointing modes can be separated in a roll and a pitch component. The roll and the pitch axis in the geodetic regime differ about these angular components from the direction in the geocentric mode. As a consequence, the roll axis is closer to the velocity vector in the geodetic compared to the geocentric regime.

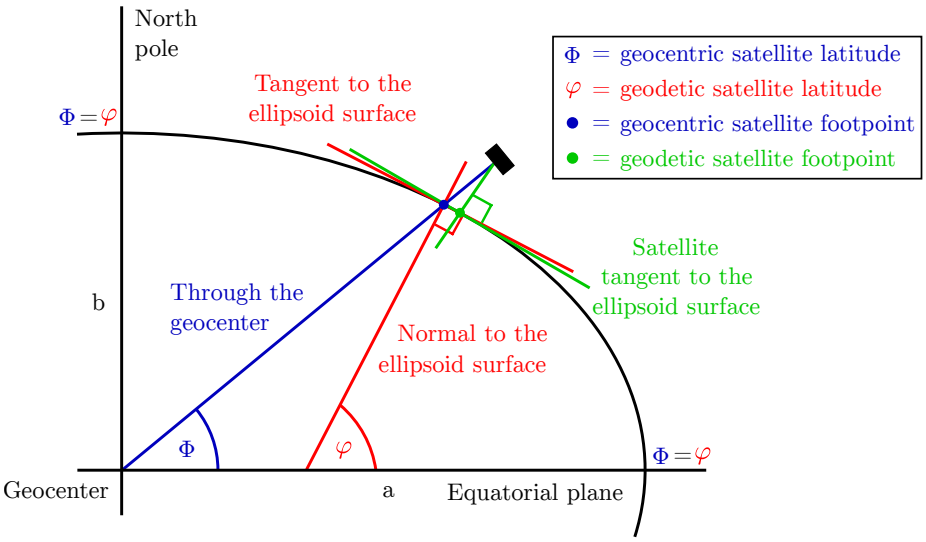

Figure 3: Visualization of the difference between geodetic and geocentric latitude.

2.1.4 Satellite body reference system

For each of the three Jason satellites, one specific satellite body reference system is defined. The satellites are constructed similarly and have roughly the same dimensions and properties. The origin of the body reference system is the center of the launcher interface ring (Cerri et al. 2010; compare Figure 34). The axis X_{SAT} points along the satellite's main direction towards the radiometer antenna and the axis Z_{SAT} is oriented towards the Earth (nadir pointing). Y_{SAT} is parallel to the rotation axis of the solar panels (positively towards the right solar panel). The axes coincide with the principle axes of inertia.

The satellite coordinate system is used for the attitude determination of the satellite (this will be discussed in detail in Section 2.2). Positions of the satellite payload (e.g., the phase center of the Global Navigation Satellite System (GNSS) receiver or the Laser Retroreflector Array (LRA)), the coordinates of the satellite's center of mass or the orientation of the satellite's solar array rotation axes are provided in this system. This system is the basic requirement of the determination of space tides (relative position between the reference points of the geodetic tracking methods, compare Section 3.3). Each of the star trackers, which determine the orientation of the spacecraft, has an own camera coordinate system. This is also referenced in the satellite body coordinate system.

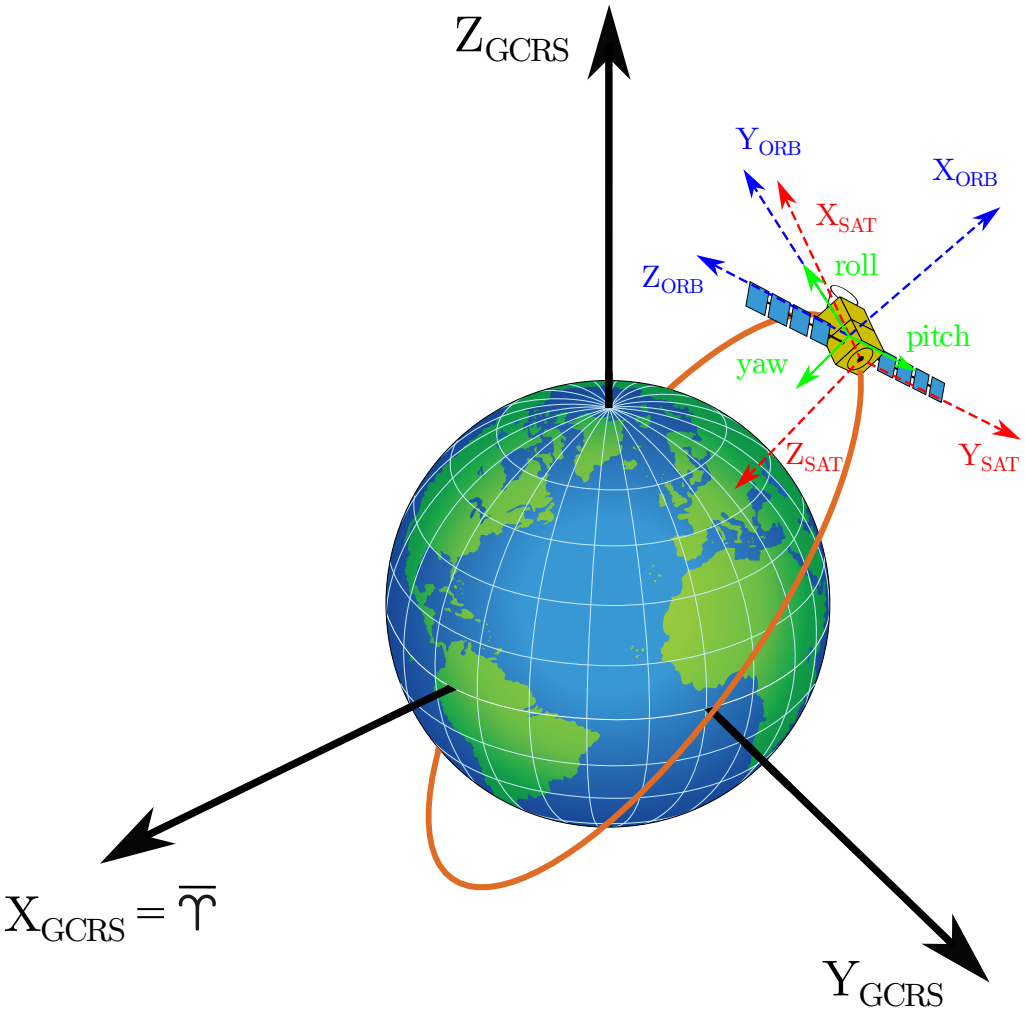

Figure 4: Coordinate systems used for orbit calculation of Jason satellites: Geocentric Celestial Reference System (GCRS) (black), satellite body reference system (SAT) (red), orbital reference system (ORB) (blue), local orbital reference system – roll-pitch-yaw (RPN) (green)[2].

Table 1: Reference systems used for the attitude determination of Jason satellites.

Reference system	X axis	Y axis	Z axis	Origin
GCRS	Towards the mean vernal equinox $\overline{\Upsilon}$	Perpendicular to the X axis towards East in the equatorial plane	The Earth's mean rotation axis	Earth's center of mass
Orbital	Radial away from the Earth's center of mass	Completes orthogonal system, along the velocity vector*	Perpendicular to radial vector and normal to orbital plane (direction of angular momentum)	Satellite's center of mass
Roll-Pitch-Yaw (geocentric pointing)	Roll: along the velocity vector*	Pitch: perpendicular to orbital plane (opposite direction of angular momentum)	Yaw: radial towards the Earth's center, perpendicular to the ellipsoid	Satellite's center of mass
Satellite	Along satellite's main direction	Parallel to the rotation axis of the solar panels	Radial towards the Earth (nadir), perpendicular to the ellipsoid	Center of the attachment ring

* Not necessarily parallel to the velocity vector (only parallel for circular orbits)

2.1.5 Coordinate transformations

The transformations between the reference systems are realized by passive rotation matrices (for detailed information about active and passive rotation matrices see Chapter 2.2.4). The starting system is denoted in the subscript and the target system in the superscript of the rotation matrix.
The satellite attitude, which is the orientation of the satellite reference system with respect to the Celestial Reference System (CRS), is expressed by

$$\begin{aligned} \boldsymbol{X}_{SAT} &= \overbrace{\boldsymbol{R}^{SAT}_{CRS}}^{\text{attitude quaternions}} \boldsymbol{X}_{CRS} \\ &= \overbrace{\boldsymbol{R}^{SAT}_{ORB} \boldsymbol{R}^{ORB}_{CRS}} \boldsymbol{X}_{CRS} \\ &= \overbrace{\boldsymbol{R}^{SAT}_{RPY} \boldsymbol{R}^{RPY}_{ORB}}^{\text{roll/pitch/nominal yaw}} \boldsymbol{R}^{ORB}_{CRS} \boldsymbol{X}_{CRS} \end{aligned} \tag{2.1}$$

with
- $\boldsymbol{X}_{SAT}$ vector in the satellite body reference system,
- $\boldsymbol{X}_{CRS}$ vector in the CRS,
- $\boldsymbol{R}^{SAT}_{CRS}$ rotation matrix from the CRS to the satellite body reference system,
- $\boldsymbol{R}^{SAT}_{ORB}$ rotation matrix from the orbital to the satellite body reference system,
- $\boldsymbol{R}^{SAT}_{RPY}$ rotation matrix from the local orbital (roll-pitch-yaw) to the satellite body reference system (roll and pitch contain the differences between the geodetic and the geocentric pointing),
- $\boldsymbol{R}^{RPY}_{ORB}$ rotation matrix from the orbital to the local orbital reference system and
- $\boldsymbol{R}^{ORB}_{CRS}$ rotation matrix from the CRS to the orbital reference system.

The matrix $\boldsymbol{R}_{CRS}^{SAT}$ can be realized by attitude quaternions or a model of the intended satellite attitude. In the case of Jason satellites, a so-called nominal yaw steering model is used (compare Chapters 2.2.3 and 3.5).

The matrix $\boldsymbol{R}_{RPY}^{SAT}$ rotates the local orbital system into the satellite reference system. The transition from geodetic to geocentric pointing is comprised by the angles roll and pitch.

$$\begin{aligned}\boldsymbol{R}_{RPY}^{SAT}(\phi,\theta,\psi) &= \boldsymbol{R}_Z(\psi)\boldsymbol{R}_Y(\theta)\boldsymbol{R}_X(\phi) \\ &= \begin{bmatrix} \cos\psi\cos\theta & \sin\phi\sin\theta\cos\psi+\sin\psi\cos\phi & -\cos\phi\sin\theta\cos\psi+\sin\psi\sin\phi \\ -\sin\psi\cos\theta & -\sin\phi\sin\theta\sin\psi+\cos\psi\cos\phi & \cos\phi\sin\theta\sin\psi+\cos\psi\sin\phi \\ \sin\theta & -\sin\phi\cos\theta & \cos\phi\cos\theta \end{bmatrix},\end{aligned} \tag{2.2}$$

with ϕ, θ, ψ being the roll, pitch and yaw angles, respectively.

Vice versa, the angles can be calculated from $\boldsymbol{R}_{RPY}^{SAT}$ by

$$\phi = -\arctan\left(\frac{\boldsymbol{R}_{32}}{\boldsymbol{R}_{33}}\right), \quad \theta = -\arcsin(\boldsymbol{R}_{31}), \quad \psi = -\arctan\left(\frac{\boldsymbol{R}_{21}}{\boldsymbol{R}_{11}}\right). \tag{2.3}$$

The matrix $\boldsymbol{R}_{CRS}^{ORB}$ can be computed from the position vector and the velocity vector ($\boldsymbol{r}_{CRS}, \boldsymbol{v}_{CRS} \in \mathbb{R}^{3\times1}$) of the satellite in the inertial system (Montenbruck, 2012):

$$\boldsymbol{R}_{CRS}^{ORB} = \left[\begin{array}{c:c:c} \boldsymbol{r} & \boldsymbol{t} & \boldsymbol{n} \end{array}\right], \tag{2.4}$$

where

$$\boldsymbol{r} = \frac{\boldsymbol{r}_{CRS}}{|\boldsymbol{r}_{CRS}|}, \quad \boldsymbol{n} = \frac{\boldsymbol{r}_{CRS}\times\boldsymbol{v}_{CRS}}{|\boldsymbol{r}_{CRS}\times\boldsymbol{v}_{CRS}|}, \quad \boldsymbol{t} = \boldsymbol{n}\times\boldsymbol{r}. \tag{2.5}$$

The matrix $\boldsymbol{R}_{ORB}^{RPY}$ is satellite independent and rotates the orbital into the local orbital system.

$$\begin{aligned}\boldsymbol{R}_{ORB}^{RPY} = \boldsymbol{R}_{X,ORB}(-90^\circ)\boldsymbol{R}_{Z,ORB}(90^\circ) &= \begin{bmatrix} 1 & 0 & 0 \\ 0 & \cos(-90^\circ) & \sin(-90^\circ) \\ 0 & -\sin(-90^\circ) & \cos(-90^\circ) \end{bmatrix}\begin{bmatrix} \cos(90^\circ) & \sin(90^\circ) & 0 \\ -\sin(90^\circ) & \cos(90^\circ) & 0 \\ 0 & 0 & 1 \end{bmatrix} \\ &= \begin{bmatrix} 1 & 0 & 0 \\ 0 & 0 & -1 \\ 0 & 1 & 0 \end{bmatrix}\begin{bmatrix} 0 & 1 & 0 \\ -1 & 0 & 0 \\ 0 & 0 & 1 \end{bmatrix} \\ &= \begin{bmatrix} 0 & 1 & 0 \\ 0 & 0 & -1 \\ -1 & 0 & 0 \end{bmatrix}\end{aligned} \tag{2.6}$$

Note: All coordinate systems are right-handed, only passive rotations are applied and the rotation angles are positive in the counterclockwise direction.

2.2 Attitude parametrization

A major task of the satellite handling is to determine the satellite attitude (rotational orientation) in space. In the three-dimensional space, three independent parameters are required to clearly represent the attitude. For reasons of simplification, we use the approximation to consider a satellite as a rigid body. In reality though, perturbing forces affecting the satellite make the determination of the attitude clearly more complex. This is discussed in detail in Chapter 2.3.

Direction cosine matrices provide one method of attitude parametrization (Chapter 2.2.1). Linked to this, the concept of Euler axis and angle is shown in Chapter 2.2.2. Afterwards, Chapter 2.2.3 explains the representation of the attitude with quaternions. Finally, Chapter 2.2.4 demonstrates the principle of Euler angles.

The conversion between the given attitude representations is provided in Appendix A.

2.2.1 Direction cosine matrix

To represent the attitude of a satellite, we need to implement two coordinate systems (Figure 5). The first system is attached to the satellite (or rigid body) and therefore called *body reference system*, $\mathcal{R}_B$. The second system represents an *inertial reference system*, $\mathcal{R}_I$. Both systems, $\mathcal{R}_I$ and $\mathcal{R}_B$, are composed of three orthogonal, right-handed unit vectors $\boldsymbol{X}$, $\boldsymbol{Y}$, $\boldsymbol{Z}$ and $\boldsymbol{x}$, $\boldsymbol{y}$, $\boldsymbol{z}$, respectively. Furthermore, positive rotation angles are used counterclockwise according to the mathematical standard.

The attitude of the satellite and simultaneously the attitude of the body reference system is described by the rotational orientation of the coordinate axes of $\mathcal{R}_B$ with respect to the axes of $\mathcal{R}_I$ (Wertz, 2002). Therefore, we need nine orientation parameters, which form the *attitude matrix* $\boldsymbol{A} \in \mathbb{R}^{3\times3}$

$$\boldsymbol{A} = \begin{bmatrix} a_{xX} & a_{yX} & a_{zX} \\ a_{xY} & a_{yY} & a_{zY} \\ a_{xZ} & a_{yZ} & a_{zZ} \end{bmatrix}. \tag{2.7}$$

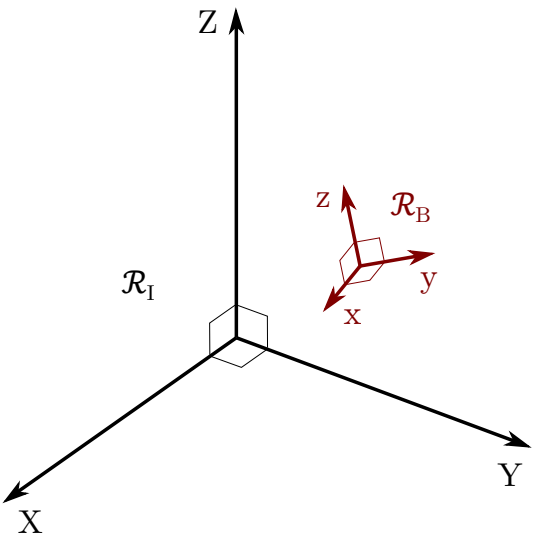

Figure 5: Attitude determination: parametrization of the satellite body reference system $\mathcal{R}_B$ with respect to the inertial system $\mathcal{R}_I$.[4]

Each element of the matrix represents the cosine of the angle between the axis of the body system and the inertial system. Hence, element a_{yX} contains the cosine of the angle between the y axis of the body system and X axis of the inertial system. As a result of this composition, matrix $\boldsymbol{A}$ is also called Direction Cosine Matrix (DCM) and can be computed according to Großekatthöfer and Yoon (2012) with

$$\boldsymbol{A} = \begin{bmatrix} \cos(\sphericalangle\, \boldsymbol{xX}) & \cos(\sphericalangle\, \boldsymbol{yX}) & \cos(\sphericalangle\, \boldsymbol{zX}) \\ \cos(\sphericalangle\, \boldsymbol{xY}) & \cos(\sphericalangle\, \boldsymbol{yY}) & \cos(\sphericalangle\, \boldsymbol{zY}) \\ \cos(\sphericalangle\, \boldsymbol{xZ}) & \cos(\sphericalangle\, \boldsymbol{yZ}) & \cos(\sphericalangle\, \boldsymbol{zZ}) \end{bmatrix} = \begin{bmatrix} \langle \boldsymbol{x}, \boldsymbol{X} \rangle & \langle \boldsymbol{y}, \boldsymbol{X} \rangle & \langle \boldsymbol{z}, \boldsymbol{X} \rangle \\ \langle \boldsymbol{x}, \boldsymbol{Y} \rangle & \langle \boldsymbol{y}, \boldsymbol{Y} \rangle & \langle \boldsymbol{z}, \boldsymbol{Y} \rangle \\ \langle \boldsymbol{x}, \boldsymbol{Z} \rangle & \langle \boldsymbol{y}, \boldsymbol{Z} \rangle & \langle \boldsymbol{z}, \boldsymbol{Z} \rangle \end{bmatrix}, \tag{2.8}$$

where $\langle \cdot \rangle$ is the dot product of both vectors.

[4] Original from Wertz (2002)

The direction cosine matrix performs a transformation between two systems and possesses some important characteristics. The matrix only contains real numbers and is composed of orthonormal unit vectors (the vectors are perpendicular to each other and have the norm unity, e.g., $|\boldsymbol{a}_x| = \left(a_{xX}^2 + a_{xY}^2 + a_{xZ}^2\right)^{1/2} = 1$). The product of matrix $\boldsymbol{A}$ with its transpose equals the identity matrix $\boldsymbol{I} = \boldsymbol{A}\boldsymbol{A}^T$. The inverse of each orthogonal matrix equals its transpose ($A^T = A^{-1}$). This means that $\boldsymbol{A}$ transforms vectors from the inertial system to the body system and both, its transpose and inverse, transform vectors from the body system to the inertial system. The determinant of $\boldsymbol{A}$ is 1, which results in $\boldsymbol{A}$ being a proper real orthonormal matrix. Due to these properties, the multiplication of vectors with a direction cosine matrix preserves the length of the vectors and the angles between them.

The transformation of a vector with a direction cosine matrix is simultaneously a rotation of a coordinate system. The difference between a vector rotation and the rotation of a coordinate system is explained in detail in Section 2.2.4.

2.2.2 Euler axis and angle

At each rotation exists a vector which is unchanged by the rotation (Wertz, 2002). This vector coincides with the axis of rotation.

In 1775, Leonard Euler proved the existence of this unaffected vector in his theorem. The theorem states that any displacement of a rigid body corresponds to a rotation about some axis. One point on the rigid body remains fixed and the rotation axis runs through this point. A combination of two consecutive rotations is a rotation, too.

Figure 6 shows a sphere which is rotated around the *Euler axis* $\boldsymbol{e}$ by the *Euler angle* θ. The position of the red point on the surface of the sphere is not affected by the rotation.

The rotation matrix according to both parameters around any axis represents the most general rotation matrix $\boldsymbol{R}$:

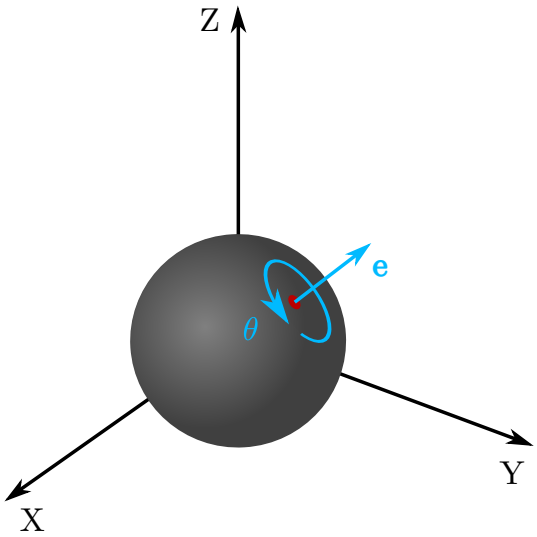

Figure 6: Euler axis and angle parametrization.[5]

$$\boldsymbol{R} = \begin{bmatrix} \cos\theta + e_1^2(1-\cos\theta) & e_1e_2(1-\cos\theta) + e_3\sin\theta & e_1e_3(1-\cos\theta) - e_2\sin\theta \\ e_1e_2(1-\cos\theta) - e_3\sin\theta & \cos\theta + e_2^2(1-\cos\theta) & e_2e_3(1-\cos\theta) + e_1\sin\theta \\ e_1e_3(1-\cos\theta) + e_2\sin\theta & e_2e_3(1-\cos\theta) - e_1\sin\theta & \cos\theta + e_3^2(1-\cos\theta) \end{bmatrix} \tag{2.9}$$

The unit vector $\boldsymbol{e} = [e_1 \;\; e_2 \;\; e_3]^T$ represents the axis of rotation and θ is the angle of rotation. This representation of the attitude depends on four parameters and is called *Euler axis and angle* parametrization.

[5] Original version from `https://upload.wikimedia.org/wikipedia/commons/5/51/Euler_AxisAngle.png`

2.2.3 Quaternions

The attitude can also be parameterized by four Euler parameters. In attitude representation, these parameters are referred to as *quaternions*.

A quaternion $\boldsymbol{q}$ consists of four elements q_s, q_x, q_y, q_z and is defined as

$$\boldsymbol{q} \equiv q_s + iq_x + jq_y + kq_z. \tag{2.10}$$

q_s, q_x, q_y, q_z are real numbers and i, j, k are imaginary numbers satisfying following conditions (Dam et al., 1998):

$$i^2 = j^2 = k^2 = -1 \tag{2.11}$$

$$ij = -ji = k, \quad jk = -kj = i, \quad ki = -ik = j \tag{2.12}$$

The vector form of a quaternion $\boldsymbol{q}$ is expressed as

$$\boldsymbol{q} = \begin{bmatrix} q_s \\ q_x \\ q_y \\ q_z \end{bmatrix} = \begin{bmatrix} s \\ \boldsymbol{v} \end{bmatrix}, \tag{2.13}$$

where the component $s \in \mathbb{R}$ represents the *scalar (real) part* and $\boldsymbol{v} \in \mathbb{R}^3$ the *vector (imaginary) part* of the quaternion. Note: In literature, the quaternion definition $\boldsymbol{q} = [\boldsymbol{v} \;\; s]^T$ is used, too.

The four components of a quaternion contain the unit vector $\boldsymbol{e} = [e_1 \;\; e_2 \;\; e_3]^T$ of the rotation axis as well as the angle of rotation θ, and can be written with trigonometric functions as following:

$$q_s = \cos\frac{\theta}{2}, \quad q_x = e_1 \sin\frac{\theta}{2}, \quad q_y = e_2 \sin\frac{\theta}{2}, \quad q_z = e_3 \sin\frac{\theta}{2}. \tag{2.14}$$

Quaternion mathematics

The conjugate of a quaternion is defined as

$$\boldsymbol{q}^* \equiv \begin{bmatrix} q_s \\ -q_x \\ -q_y \\ -q_z \end{bmatrix} = \begin{bmatrix} s \\ -\boldsymbol{v} \end{bmatrix}. \tag{2.15}$$

The norm of a quaternion is calculated by

$$|\boldsymbol{q}| \equiv \sqrt{\boldsymbol{q}\boldsymbol{q}^*} = \sqrt{q_s^2 + q_x^2 + q_y^2 + q_z^2}. \tag{2.16}$$

A quaternion with the norm $|\boldsymbol{q}| = 1$ is a *unit quaternion*. In attitude representation only unit quaternions are used.

To obtain unit quaternions, a quaternion is normalized by dividing it by its norm:

$$\|\boldsymbol{q}\| = \frac{\boldsymbol{q}}{|\boldsymbol{q}|}. \tag{2.17}$$

The normalized conjugate of a quaternion is its inverse:

$$\boldsymbol{q}^{-1} = \frac{\boldsymbol{q}^*}{|\boldsymbol{q}|}. \tag{2.18}$$

In case of unit quaternions, the inverse equals the conjugate.

The multiplication of two quaternions $\boldsymbol{p}$ and $\boldsymbol{q}$ is

$$\boldsymbol{q}' = \boldsymbol{p} \circ \boldsymbol{q} = \begin{bmatrix} s_p s_q - \langle \boldsymbol{v}_p, \boldsymbol{v}_q \rangle \\ s_p \boldsymbol{v}_q + s_q \boldsymbol{v}_p + \boldsymbol{v}_p \times \boldsymbol{v}_q \end{bmatrix}. \tag{2.19}$$

The operator $\circ$ represents the quaternion multiplication. As with matrix multiplication, quaternion multiplication is not generally commutative.

Quaternion rotation

Using the explanations of Chapter 2.2.1, a rotation of a vector from the inertial coordinate system to the body coordinate system using a cosine direction matrix is given by

$$\boldsymbol{v}_B = \boldsymbol{R}_I^B \boldsymbol{v}_I. \tag{2.20}$$

The corresponding rotation effected with a quaternion is

$$\boldsymbol{v}_B = \boldsymbol{q}^* \circ \boldsymbol{v}_I \circ \boldsymbol{q}, \tag{2.21}$$

where $\boldsymbol{v}_I \in \mathbb{R}^4$ is expressed in the quaternion notation and extended with the scalar part zero as the first element of the vector.

A composition of two consecutive quaternion rotations $\boldsymbol{q}_1$ and $\boldsymbol{q}_2$ is represented by a quaternion multiplication (an example is provided in Appendix B):

$$\boldsymbol{q} = \boldsymbol{q}_1 \circ \boldsymbol{q}_2. \tag{2.22}$$

2.2.4 Euler angles

Euler angles form a fourth possible representation of the attitude of a rigid body. This parametrization of the attitude is geometrically more apparent than the use of quaternions. Three Euler angles ϕ, θ, ψ are used in three consecutive rotations around the coordinate axes. The composed rotation can represent any orientation of the rigid body.

Here, a clear separation of a vector rotation and a rotation of a coordinate system is recommended. The coordinates of a vector are changed in both situations. The application of a vector rotation modifies the vector's coordinates actively by moving the vector itself within one system. In this case, the axes of the coordinate system stay fixed. Thus, this rotation is called active rotation.

The passive rotation affects the unit vectors of the coordinate system while keeping the vector fixed. The vector is actually transformed from the original system to a target system. Thus, this definition is generally known as (vector) transformation. Note that both conventions are inverse to each other.

The matrices of the rotations about axis X, Y or Z by the angle φ are denoted by the elementary matrices $\boldsymbol{R}_X(\varphi)$, $\boldsymbol{R}_Y(\varphi)$ and $\boldsymbol{R}_Z(\varphi)$, respectively. In the case of passive rotations (characterized by superscript P), the matrices are defined as

$$\begin{aligned}
\boldsymbol{R}_X^P(\varphi) &= \begin{bmatrix} 1 & 0 & 0 \\ 0 & \cos\varphi & \sin\varphi \\ 0 & -\sin\varphi & \cos\varphi \end{bmatrix}, \\
\boldsymbol{R}_Y^P(\varphi) &= \begin{bmatrix} \cos\varphi & 0 & -\sin\varphi \\ 0 & 1 & 0 \\ \sin\varphi & 0 & \cos\varphi \end{bmatrix}, \\
\boldsymbol{R}_Z^P(\varphi) &= \begin{bmatrix} \cos\varphi & \sin\varphi & 0 \\ -\sin\varphi & \cos\varphi & 0 \\ 0 & 0 & 1 \end{bmatrix}.
\end{aligned} \tag{2.23}$$

Vice versa, the matrices of an active rotation are

$$\boldsymbol{R}_X^A(\varphi) = \left(\boldsymbol{R}_X^P(\varphi)\right)^T, \quad \boldsymbol{R}_Y^A(\varphi) = \left(\boldsymbol{R}_Y^P(\varphi)\right)^T, \quad \boldsymbol{R}_Z^A(\varphi) = \left(\boldsymbol{R}_Z^P(\varphi)\right)^T. \tag{2.24}$$

Figure 7 explains the principle of an active and a passive rotation. In the left-handed subplot, point P is rotated in the clockwise direction by the angle φ around the Z axis of the coordinate system. The coordinates of the point are actively changed by applying the rotation on the point itself. The resulting point is displayed by P'. In subplot b), the original coordinate system (blue) is rotated around the Z axis by the same angle φ in the counterclockwise direction into the target coordinate system (green). Point P' with respect to the green coordinate system possesses after the rotation the same coordinates as point P' in the blue system in subplot a). The coordinates of the original point change without moving the point directly (passive modification of the coordinates). Both points are located on the same position but have different coordinates depending on the considered coordinate system.

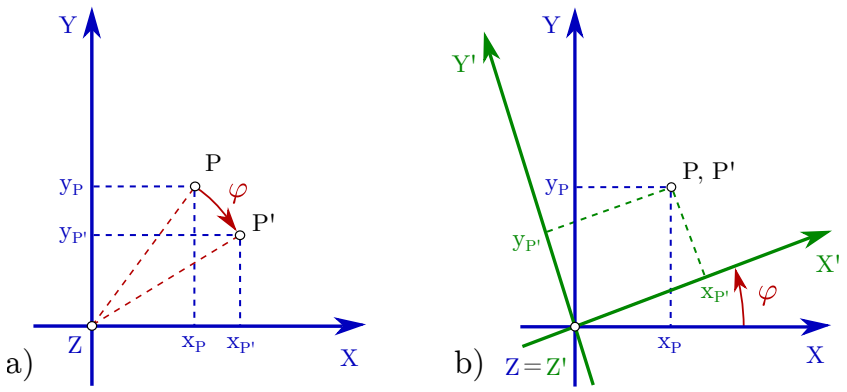

Figure 7: Comparison of rotations: (a) Active rotation of point P in the blue coordinate system. (b) Passive rotation (= transformation) of point P by rotating the coordinate system.

The attitude parametrization with Euler angles uses three consecutive rotations about the coordinate axes (passive rotations). According to Wertz (2002), four coordinate systems, which are represented by three orthogonal unit vectors, are used for the explanation of the principle of Euler angles (compare Figure 8):

$$\boldsymbol{X}, \boldsymbol{Y}, \boldsymbol{Z} \qquad \boldsymbol{X}', \boldsymbol{Y}', \boldsymbol{Z}' \qquad \boldsymbol{X}'', \boldsymbol{Y}'', \boldsymbol{Z}'' \qquad \boldsymbol{x}, \boldsymbol{y}, \boldsymbol{z}$$

The first triad of unit vectors displays the inertial coordinate system, the subsequent second and third triad represent intermediate coordinate systems after the application of the first and second rotation, respectively. The axes of the final coordinate system, represented by the last triad, are parallel to the axes of the body coordinate system.

The difference between the axes of the inertial coordinate system and the axes of the coordinate system represented by $\boldsymbol{X}'$, $\boldsymbol{Y}'$, $\boldsymbol{Z}'$ is a rotation with the angle ϕ around the axis i = X, Y or Z of the inertial system. Depending on the chosen axis, the rotation matrix $\boldsymbol{R}_i(\phi)$ is represented by one of the direction cosine matrices given in Equation 2.23.

A second rotation $\boldsymbol{R}_j(\theta)$ (j = X, Y or Z and j ≠ i) rotates the coordinate system $\boldsymbol{X}'$, $\boldsymbol{Y}'$, $\boldsymbol{Z}'$ into the next temporary system $\boldsymbol{X}''$, $\boldsymbol{Y}''$, $\boldsymbol{Z}''$. The rotation angle is θ and the rotation axis is one of the two axes which are not used in the first rotation.

Equally, the final coordinate system x, y, z results from the rotation $\boldsymbol{R}_k(\psi)$ which rotates the system $\boldsymbol{X}''$, $\boldsymbol{Y}''$, $\boldsymbol{Z}''$ with the rotation angle ψ. The rotation axis k = X, Y or Z (k ≠ j) can be the axis of the first rotation (k = i) or the unused third axis.

To finally obtain the orientation of the body system with respect to the inertial system, the rotation matrix $\boldsymbol{R}$, which is composed of the three individual rotation matrices, is required. This matrix varies according to the sequence of applied rotation (see Table 2). Two consecutive rotations about the same type of axis are not allowed, because this case results in a single rotation about that specific axis. Taking this rule into account, there exist twelve different sequences which can be divided into two groups:

Table 2: Distinction of Euler angles and Cardan angles according the sequences of the rotations (Bronstein et al., 2013).

Type of angles	Characteristics	Possible sequences
Euler angles	First and last rotation around the same type of axis	XYX, XZX, YXY, YZY, ZXZ, ZYZ
Cardan angles	Rotations about all three coordinate axes	XYZ, XZY, YXZ, YZX, ZXY, ZYX

Matrix $\boldsymbol{R}$ of the entire rotation is obtained by multiplication of the individual rotation matrices. Let the first rotation be around the Z axis with the angle ϕ, the second around the X axis with the angle θ and the final rotation around the Y axis by the angle ψ. Due to the application of rotations around all three axes, the rotation angles are known as Cardan angles. Consequently, $\boldsymbol{R}$ is defined as

$$\begin{aligned}\boldsymbol{R}_{ZXY}(\phi,\theta,\psi) &:= \boldsymbol{R}_Y(\psi)\boldsymbol{R}_X(\theta)\boldsymbol{R}_Z(\phi) \\ &= \begin{bmatrix} \cos\psi\cos\phi - \sin\theta\sin\psi\sin\phi & \cos\psi\sin\phi + \sin\theta\sin\psi\cos\phi & -\cos\theta\sin\psi \\ -\cos\theta\sin\phi & \cos\theta\cos\phi & \sin\theta \\ \sin\psi\cos\phi + \sin\theta\cos\psi\sin\phi & \sin\psi\sin\phi - \sin\theta\cos\psi\cos\phi & \cos\theta\cos\psi \end{bmatrix}.\end{aligned} \tag{2.25}$$

Using Euler angles for the rotation sequence ZYZ yields

$$\begin{aligned}\boldsymbol{R}_{ZYZ}(\phi,\theta,\psi) &:= \boldsymbol{R}_Z(\psi)\boldsymbol{R}_Y(\theta)\boldsymbol{R}_Z(\phi) \\ &= \begin{bmatrix} \cos\psi\cos\theta\cos\phi - \sin\psi\sin\phi & \cos\psi\cos\theta\sin\phi + \sin\psi\cos\phi & -\cos\psi\sin\theta \\ -\sin\psi\cos\theta\cos\phi - \cos\psi\sin\phi & -\sin\psi\cos\theta\sin\phi + \cos\psi\cos\phi & \sin\psi\sin\theta \\ \sin\theta\cos\phi & \sin\theta\cos\phi & \cos\theta \end{bmatrix}.\end{aligned} \tag{2.26}$$

Sequence ZYZ is illustrated in Figure 8. The original system (blue) is rotated into the target system (green) while forming two intermediate coordinate systems.

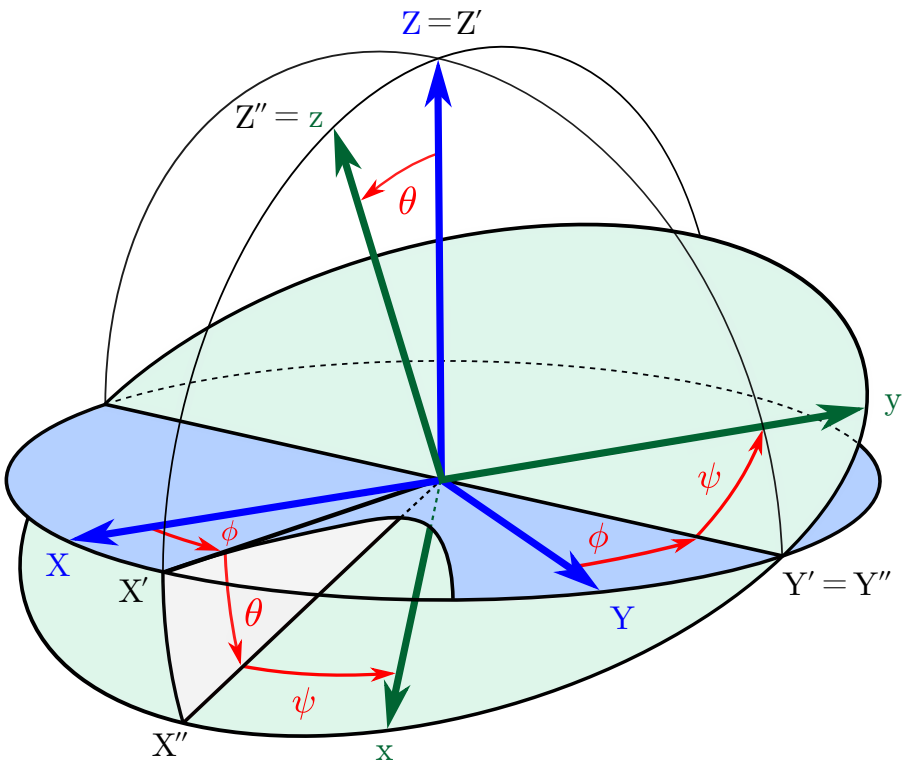

Figure 8: Coordinate rotation represented by Euler angles: first rotation with the angle ϕ about axis Z, second rotation with the angle θ about axis Y′, third rotation with the angle ψ about axis Z″.[6]

[6] Original version from `http://easyspin.org/documentation/eulerangles.html`, Last access: 2019-06-19

2.2.5 Comparison of attitude representations

Advantages and limitations of attitude parametrizations

There are several reasons for the usage of quaternions in attitude representation. They provide certain essential characteristics to correctly express the satellite's rotational orientation. The most important aspect is the prevention of gimbal lock. In both Euler angles and direction cosine matrix parametrization though, gimbal lock can arise in certain situations. In cases of gimbal lock, the vectors of the rotation axis of the first and third rotation are collinear, and this results in a loss of one degree of freedom in the rotation (Markley and Crassidis, 2014; Dam et al., 1998). All rotation sequences with $\sin\theta = 0$ result in gimbal lock.

Figure 9 illustrates the principle of gimbal lock. The outer blue frame represents the x axis, the middle red-colored gimbal the y axis and the green gimbal the z axis. In the original constellation a), all axes are perpendicular to each other. After a rotation of 90° around the y axis (symbolized by the red arrow), the blue and the green frame possess the same rotation axis (shown in b)). This situation impedes the clear determination of the rotation axes when subsequently rotating around the x or z axis.

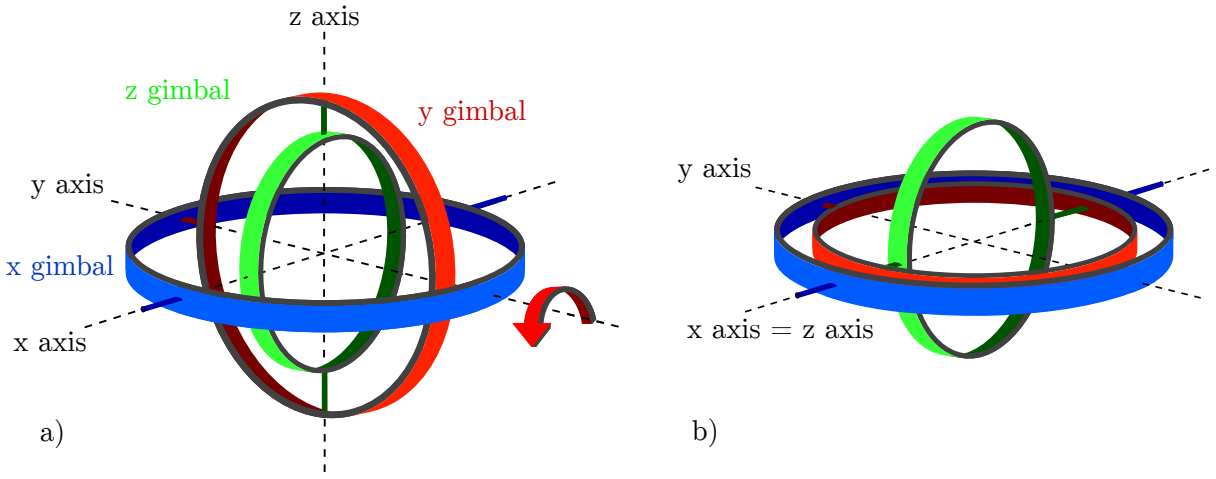

Figure 9: Occurrence of gimbal lock: (a) Initial situation with three coordinate axes being perpendicular to each other. (b) The x and z axis coincide after a rotation of 90° around the y axis.

A further benefit of quaternions is the more natural representation of rotations with a rotation axis and a rotation angle. Furthermore, quaternion mathematics provide optimal interpolation methods (see below). Quaternions allow a more compact parametrization compared to direction cosine matrix, because it only consists of four parameters instead of nine. Additionally, no time-consuming and computationally intensive trigonometric functions are needed. Composed rotations show a third mathematical benefit of quaternions. While 27 multiplications are required at the matrix multiplication in the direction cosine matrix and Euler angle representation, quaternion multiplication only needs 16 multiplications (Wertz, 2002).

Euler angles and direction cosine matrix parametrization have some benefits as well. They provide relatively easy implementation of matrix applications and mathematics appear to be less complicated and more intuitive than quaternion mathematics.

Table 3 lists advantages and limitations of Euler angles, direction cosine matrices and quaternions.

Table 3: Advantages and limitations of attitude parametrizations in the three-dimensional space (Wertz, 2002)

Parametrization	Advantages	Disadvantages
Euler angles	No redundant parameters (minimum of three parameters required)	No convenient product rule for successive rotations
		Singularities in some cases
		Trigonometric functions
Direction cosine matrix	More intuitive mathematics	Six redundant parameters
	No singularities	
	No trigonometric functions	
	Convenient product rule for successive rotations	
Quaternions	No singularities (gimbal lock)	One redundant parameter
	No trigonometric functions	Complicated mathematics
	Computationally less intense	
	Convenient product rule for successive rotations	
	Optimal interpolation methods	

Interpolation of rotation

The expression of the attitude or rotation between two rotations requires an interpolation of the rotation parameters. An interpolation can be performed with each parametrization. Though, not every parametrization fits equally well for an interpolation. The performance of an interpolation can be evaluated by two characteristics, the location of quaternions on a quaternion unit sphere (Euler angles and other parameter have to be converted into unit quaternions first) and the angular velocity of the interpolation curve. To receive an optimal rotation, the interpolated quaternion must be a unit quaternion and thus be located on the surface of the quaternion unit sphere.

Linear interpolation

Euler angles can be interpolated with a linear Euler interpolation and direction cosine matrices with linear matrix interpolation. In both cases, the interpolation curve disappears from the surface of the unit sphere and the angular velocity is not constant. Thus, both interpolations are not optimal.

Linear quaternion interpolation is not optimal as well, since interpolated quaternions are not unit quaternions in general.

Spherical linear quaternion interpolation

The limitations occurring in the linear interpolation are avoided when applying Spherical Linear Quaternion Interpolation (SLERP). This method provides unit quaternions as the result of the interpolation. Thus, the interpolation curve follows a great arc on the quaternion unit sphere (SLERP performs a great arc interpolation).

Let $\boldsymbol{q}_1$ and $\boldsymbol{q}_2$ be two rotation quaternions given at two epochs $t_1 = 0$ and $t_2 = 1$, respectively. The desired rotation quaternion shall be $\boldsymbol{q}$ at the epoch $t \in [0, 1]$ (this parameter is also called interpolation parameter). Dam et al. (1998) provides the following expression for the calculation of $\boldsymbol{q}_t$:

$$\boldsymbol{q}(\boldsymbol{q}_1, \boldsymbol{q}_2, t) = \boldsymbol{q}_1 \circ \left(\boldsymbol{q}_1^* \circ \boldsymbol{q}_2\right)^t . \tag{2.27}$$

The equivalent formula without exponentiation is

$$\boldsymbol{q}(\boldsymbol{q}_1, \boldsymbol{q}_2, t) = \frac{\boldsymbol{q}_1 \sin((1-t)\Omega) + \boldsymbol{q}_2 \sin(t\Omega)}{\sin(\Omega)}, \tag{2.28}$$

with

$$\cos(\Omega) = \langle \boldsymbol{q}_1, \boldsymbol{q}_2 \rangle = q_{1s}q_{2s} + q_{1x}q_{2x} + q_{1y}q_{2y} + q_{1z}q_{2z}. \tag{2.29}$$

Ω represents the angle between the quaternions $\boldsymbol{q}_1$ and $\boldsymbol{q}_2$, and $\langle \cdot \rangle$ is the corresponding dot product.

According to Dam et al. (1998), SLERP yields the shortest great arc between $\boldsymbol{q}_1$ and $\boldsymbol{q}_2$ on the unit quaternion sphere and provides constant angular velocity. Hence, SLERP performs an optimal interpolation.

2.3 Orbit perturbations

The orbit of a satellite can be determined precisely with different settings. The gravity field and all non-conservative forces interacting with the satellite are not considered in kinematic orbit determination (Svehla and Rothacher, 2003). In contrast, the dynamic approach includes all perturbing accelerations and provides a fully physical orbit. The reduced dynamic orbit determination is extended by additional empirical parameters which absorb unmodelled or unknown perturbations.

Precise orbit determination requires detailed investigation of perturbations acting on the satellite. These effects cause a variation of the satellite orbit compared to the theoretical, undisturbed path. In general, perturbing forces can be divided into two main groups: gravitational and non-gravitational effects.

2.3.1 Gravitational perturbations

The motion of satellites around the Earth can be expressed as a first approximation by the equation of the two-body problem (Doornbos, 2011). This approach assumes an undisturbed Keplerian motion and a spherically symmetric gravity field of the central body (Earth) which represents the only impact on the satellite:

$$\ddot{\boldsymbol{r}}_{kep} = -\frac{GM_\oplus}{r^2}\frac{\boldsymbol{r}}{r}, \tag{2.30}$$

where $\ddot{\boldsymbol{r}}_{kep}$ is the acceleration and $\boldsymbol{r}$ the satellite position in the reference system, G is the gravitational constant and $M_\oplus$ is the mass of the Earth.

Only taking gravitational effects into account, the above described assumption of the Earth gravity field deviates from the ideal case. Due to the Earth's rotation, the planet's shape is not a perfect sphere but slightly flattened at the poles and can be represented as a spheroid. Consequently, the Earth's gravity field is aspherical, too. Additionally, the gravity field varies temporally due to processes inside and on the surface of the Earth. These effects are considered by global gravity field models.

Beside the gravitational impact of the central body, third bodies (Moon, Sun and planets) cause accelerations on the spacecraft. These effects increase with the altitude of the satellite. Furthermore, third bodies are the initiator

of tides (e.g., solid-Earth tides, pole tides, ocean tides and atmospheric tides). For the Earth, the Sun and the Moon produce gravitational distortions which are occurring periodically due to the rotation of the Earth. Tides are indirect gravitational effects.

All gravity induced effects only affect the centers of mass of different bodies. Therefore, these accelerations are not depending on the attitude of the satellite.

2.3.2 Non-gravitational perturbations

In addition to gravitational effects, surface forces affect the position of the satellite. According to the name, these perturbations are not related to the satellite's center of mass but interact with its surface area. The area which is affected by a force varies during the satellite's motion around the Earth. To precisely calculate the resulting accelerations on the satellite, a suitable surface model and, to a more important extent, accurate attitude information is required (see Figure 10). In case of the Jason satellites, the spacecraft orientation and the rotation angles of both large solar arrays as well as the satellite macromodel, information on surface size and their optical properties are necessary. Only the knowledge of both parameters provides correct calculation of the surface and the occurring accelerations.

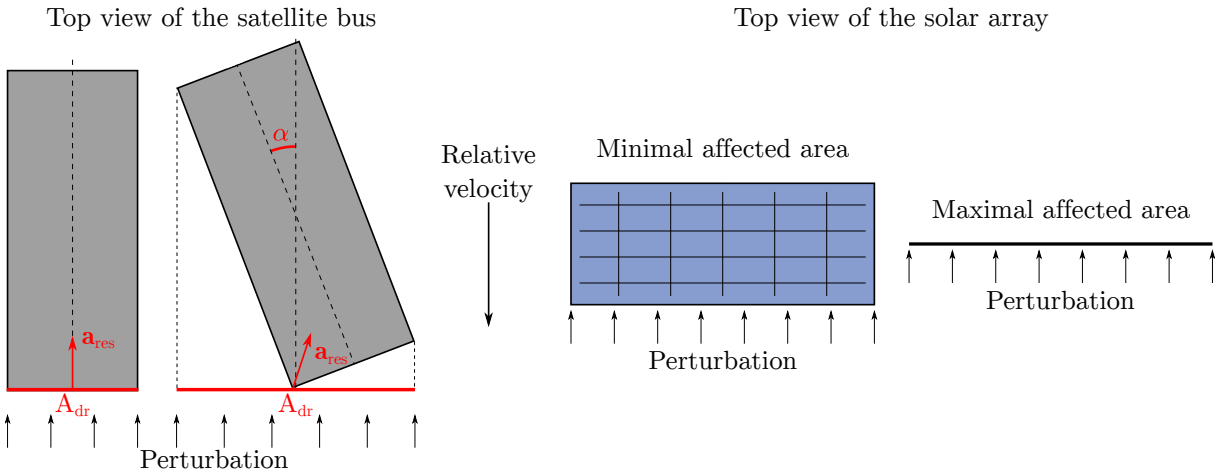

Figure 10: The cross-sectional area A_{dr} of the satellite surface, which is affected by the perturbation, and the resulting acceleration $\mathbf{a}_{res}$ depend on the attitude of the spacecraft bus (left) and the rotational orientation of the solar arrays (right).

The most important non-gravitational perturbations are:

- Atmospheric drag and perpendicular components (lift and side)
- Solar radiation pressure
- Earth re-radiation (albedo and infrared radiation) content

Aerodynamic acceleration

The particles and density of the Earth's atmosphere represent the main and most complex source of surface forces concerning near-Earth satellites (Doornbos, 2011). The principal component of aerodynamic perturbation acts in the direction of the relative velocity but in the opposite direction. Hence, the resulting acceleration on the satellite is negative and retards the spacecraft. Secondary components (lift and side accelerations) are

comparably smaller but have to be considered for non-spherical satellites. The impact of drag declines with increasing satellite altitude. The effect of drag is non-conservative (Vallado and McClain, 2007), because the satellite's total energy declines due to friction between the satellite surfaces and the particles in the atmosphere.

The influence of drag is studied by using orbital data of operation satellites which provide physical properties of the upper atmosphere. To precisely determine the impact of atmospheric perturbations, knowledge in molecular chemistry, thermodynamics, aerodynamics and meteorology and many more disciplines is required.

According to Panzetta et al. (2018), the general equation of aerodynamic drag is

$$\ddot{\boldsymbol{r}}_{adr} = -\frac{1}{2}\frac{c_D A_{dr}}{m}\rho_M \boldsymbol{v}_{rel}^2 \frac{\boldsymbol{v}_{rel}}{|\boldsymbol{v}_{rel}|}, \tag{2.31}$$

where c_D is the dimensionless aerodynamic drag coefficient, m is the satellite mass, ρ_M is the thermospheric neutral density and $\boldsymbol{v}_{rel}$ is the velocity of the satellite relative to the atmosphere. A_{dr} is the cross-sectional area of the satellite which is normal to the velocity vector and interacting atmosphere (see Figure 10). The spacecraft attitude is required to accurately determine the parameter A_{dr}.

Furthermore, the atmosphere is composed of several gases k which interact differently with the satellite surfaces. Depending on the used empirical thermospheric model and the satellite altitude, the gases are hydrogen (H), helium (He), atomic and molecular nitrogen (N, N_2), atomic and molecular oxygen (O, O_2) and argon (Ar). The total drag coefficient is obtained by the sum of the gas-specific coefficients $c_{D,k}$, weighted by the relative mass densities ρ_k:

$$\ddot{\boldsymbol{r}}_{adr} = -\frac{1}{2}\sum_i \frac{A_{dr,i}}{m}\frac{\sum_k \rho_k c_{D,k}}{\sum_k \rho_k}\rho_M \boldsymbol{v}_{rel}^2 \frac{\boldsymbol{v}_{rel}}{|\boldsymbol{v}_{rel}|}, \tag{2.32}$$

The factor $m/(c_D A_{dr})$ is also known as ballistic coefficient b and represents a measure of the sensitivity of the spacecraft to drag. Satellites with a large surface area and relatively small mass (balloon or nano-/micro-/minisatellites), which results in a small ballistic coefficient, experience a bigger influence due to atmospheric perturbations. In contrast, satellites with a big ballistic coefficient are less affected by drag (spherical satellites).

Solar radiation pressure

The influence of the solar radiation increases with higher satellite altitudes. This perturbation is non-conservative, too, and causes a force on the satellite surfaces which are exposed to the Sun. Newton's law of motion states the link between a force as the resulting acceleration.

As with the calculation of atmospheric drag, the total area $A_\oplus$ (composed of i surface elements of the macro-model) is required for rigorous determination of the acceleration. Hence, this perturbation is attitude depended as well. Additionally, shadowing effects have to be considered. Parts of the satellite can be covered by other components or the entire satellite can move through the shadow of the Earth or the Moon (eclipse). Furthermore, the Sun's exact position with respect to the satellite ($r_{sat\oplus}$) is required to determine the solar-incidence angle ϕ_{inc} between the surface normal ($\boldsymbol{n}$) and the incoming radiation ($\boldsymbol{s}$). The values of the solar radiation pressure (p_{sr}) vary due to variations in the solar activity. These variations contain the solar cycles which have a main period of approximately eleven years. c_{Rd} and c_{Rs} denote the diffuse and specular reflectivity coefficients of satellite surfaces, respectively, m is the satellite mass and c is the speed of light. Equation 2.33 provides the connection

between the solar radiation-based acceleration $\ddot{r}_{srp}$ for specular and diffuse reflection (Vallado and McClain, 2007).

$$\ddot{\boldsymbol{r}}_{srp} = -\sum_i \frac{p_{sr} A_{\odot,i} \cos\left(\phi_{inc,i}\right)}{mc} \left\{2\left(\frac{c_{Rd,i}}{3} + c_{Rs,i}\cos\left(\phi_{inc,i}\right)\right)\boldsymbol{n} + \left(1 - c_{Rs,i}\right)\boldsymbol{s}\right\} \tag{2.33}$$

Earth albedo and infrared radiation

Besides the radiation from the Sun, satellites are also influenced by radiation originating from the Earth. The Earth's radiation budget is balanced between incoming solar radiation and outgoing radiation. Latter component is composed of immediately reflected solar radiation (Earth albedo) and infrared radiation. The calculation of the Earth radiation pressure induced acceleration $\ddot{r}_{erp}$ requires a separation of the wavelength due to different interaction with the Earth's atmosphere.

The Earth albedo varies between 0.05 (ice and snow) and 0.8 (land masses) (Wertz, 2002) and each satellite component is affected differently by incoming radiation. Taking these circumstances into account, all wavelength-depended effects on the spacecraft surfaces have to be summed up to obtain the total Earth radiation pressure. As in both previous cases, the determination of the affected satellite area is based on precise attitude information. Subscript i represents the surface elements of the spacecraft macro model and j denotes the radiating surfaces of the Earth.

$$\ddot{\boldsymbol{r}}_{erp} = -\sum_i \sum_j \frac{p_{alb} A_{alb,ij} \cos\left(\phi_{inc,ij}\right)}{mc} \left\{2\left(\frac{c_{Rd,i}}{3} + c_{Rs,i}\cos\left(\phi_{inc,i}\right)\right)\boldsymbol{n} + \left(1 - c_{Rs,i}\right)\boldsymbol{s}\right\} \tag{2.34}$$

Note: The area, which is affected by non-gravitational perturbations, is in most cases not the same. While A_{dr} is normal to the relative velocity, $A_{\odot}$ and A_{alb} face the Sun and the Earth, respectively. Therefore, three varying satellite surfaces experience accelerations from different directions.

2.3.3 Other perturbations

Satellites experience many other perturbing forces which are considerably smaller but are required for precise orbit determination.

The Earth's magnetic field charges particles in the atmosphere and distorts incoming solar radiation which has an impact on the satellite. Particles with high energy are trapped in the Van Allen belts, which have the shape of a torus and surround the Earth in the equator region. A dip in the Van Allen belts causes the South Atlantic Anomaly (SAA). The SAA is roughly located over South America and the South Atlantic in an altitude of 250 km (Vallado and McClain, 2007).

Thrust impulses are perturbations as they produce changes in the satellite orbit. Therefore, a list of thrust events and the resulting mass change of the satellite is required to determine the effects on the spacecraft orbit.

Relativistic effects of near-Earth satellites (Petit and Luzum, 2010), satellite surface heating and onboard instrument vibrations can slightly influence the satellite position.

The total acceleration $\ddot{\boldsymbol{r}}$ of a near-Earth satellite is given by

$$\ddot{\boldsymbol{r}} = \ddot{\boldsymbol{r}}_g + \ddot{\boldsymbol{r}}_{ng} = \ddot{\boldsymbol{r}}_{kep} + \ddot{\boldsymbol{r}}_{ge} + \ddot{\boldsymbol{r}}_{3b} + \ddot{\boldsymbol{r}}_{rel} + \ddot{\boldsymbol{r}}_{drag} + \ddot{\boldsymbol{r}}_{srp} + \ddot{\boldsymbol{r}}_{erp} + \ddot{\boldsymbol{r}}_{other}, \tag{2.35}$$

with	$\ddot{\boldsymbol{r}}_g$	gravitational perturbations,
	$\ddot{\boldsymbol{r}}_{ng}$	non-gravitational perturbations,
	$\ddot{\boldsymbol{r}}_{kep}$	undisturbed Keplerian motion of the satellite,
	$\ddot{\boldsymbol{r}}_{ge}$	gravitational acceleration due to the Earth,
	$\ddot{\boldsymbol{r}}_{3b}$	gravitational acceleration due to third bodies,
	$\ddot{\boldsymbol{r}}_{rel}$	relativistic accelerations,
	$\ddot{\boldsymbol{r}}_{drag}$	acceleration due to aerodynamic drag*,
	$\ddot{\boldsymbol{r}}_{srp}$	acceleration due to solar radiation pressure*,
	$\ddot{\boldsymbol{r}}_{erp}$	acceleration due to Earth albedo and infrared radiation* and
	$\ddot{\boldsymbol{r}}_{other}$	other perturbing accelerations.

Attitude dependent perturbations are indicated with *.

2.4 Principle of Satellite Laser Ranging

Satellite laser ranging is one of the fundamental geodetic space techniques. The international coordination and scientific analysis of the observations is organized under the umbrella of the International Laser Ranging Service (ILRS). At this point, the author acknowledges its open data policy (Pearlman et al., 2002). The measurements are used for, e.g., the determination of satellite orbits, the estimation of station coordinates, the estimation of coefficients of the Earth's gravity field model or the calculation of Terrestrial Reference Frames (TRFs), the Earth's center of mass and scale and Earth Orientation Parameters (EOPs). The following section only briefly discusses the basic measurement principle of SLR. For more details please see Xu (2010).

SLR is determining the range from a crust-fixed ground station to a satellite orbiting around the Earth. Therefore, an optical telescope, which is coupled with a detecting device, is tracking the satellite. A laser pulse is emitted by a co-aligned transmit telescope, reflected from the satellite, which is equipped with corner cube reflectors, and registered by a sensitive light detector. The precisely measured time difference between the outgoing and incoming laser pulse is called time of flight. The basic equation for the range ρ between the station reference point and the reflector array of the satellite is

$$\rho = c \cdot \frac{\Delta t}{2}, \tag{2.36}$$

where c is the speed of light in vacuum and Δt is the time of flight.

Influences on the SLR measurement

To accurately determine the epoch of the incoming laser pulse, a sufficient number of photons have to be registered by the light detector. Various factors influence the rate of detected photoelectrons (the maximum number can vary between several hundreds and even less than one per pulse). Mechanical misalignment, not

entirely collinear telescopes, clock offsets, or instrumental and orbital biases can cause a slightly incorrect targeting of the satellite. In these cases, an operator has to manually adjust the measurement by adding correcting biases. Furthermore, the power level of the used laser, the aperture of the receiving telescope, and atmospheric conditions have a significant impact on the resulting measurement. Clouds or bad weather conditions can considerably decrease the transmittance of the atmosphere and scatter the laser pulse. Hence, SLR is a weather dependent technique. This characteristic has an important impact on the selection of the SLR station location. Besides the weather dependency, co-location advantages (astronomical observatories with additional geodetic techniques), station security and accessibility, or power supply are decisive aspects of the location selection.

To reduce the dependency to the above-mentioned insecurities, usually multiple single shots are combined to one averaged normal point.

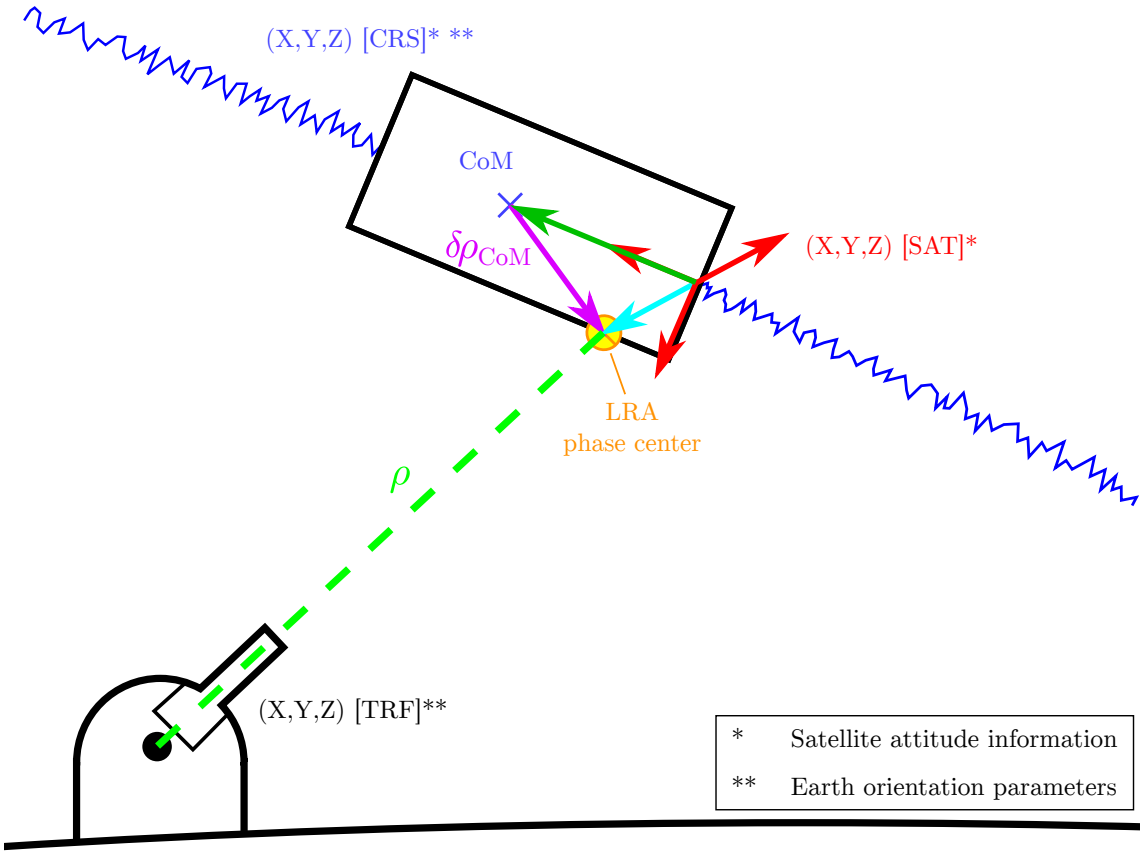

Figure 11: Principle of the geodetic space technique satellite laser ranging (SLR).

Range corrections

The dispersive nature of the troposphere causes a delay of the laser pulse. Correcting functions are optimized to the most common wavelength of 532 nm and valid for an elevation above 3°. The *atmospheric range correction* at low elevations can reach several meters which requires a high accuracy of the correction function. The DGFI-TUM uses the model adopted by Mendes and Pavlis (2004) which provides the handling of different laser wavelengths.

Due to the long path of the laser pulses through the troposphere, observations below a specific elevation are often discarded from data processing. This, however, reduces the geometrical arrangement of the measurements and therefore increases the correlations between measurement biases and the estimated station height (together with the scale of the TRF).

The SLR station is tracking a satellite during its orbit around the Earth (see Figure 11). The coordinates of the ground station are given in the TRF (black). In this coordinate system, the range between the station reference point (black dot) and the phase center of the laser reflector array (orange) is measured. The satellite orbit, which is determined in the CRS (blue), is basically representing the motion of the satellite's CoM around the Earth. Consequently, the SLR range has to be corrected by a *center-of-mass correction* (magenta arrow). This offset can only be calculated in the satellite reference system (red), in which the coordinates of the CoM (green arrow) and the phase center of the LRA (cyan arrow) are provided. The satellite's CoM varies with time due to the consumption of propellant. The transformation of the CoM correction from the satellite system to the CRS requires information about the satellite attitude. Additionally, the transformation between the CRS and the TRF is realized by EOPs.

Further range corrections are the SLR range and time biases. Uncertainties in the sensors for the determination of temperature, atmospheric pressure and relative humidity, or irregularities in the interval counter, which determines the epoch of the emitted and registered laser pulse, can cause station dependent biases. A range correction for a system delay or an error in the tie between the reference points of the station and the SLR telescope can be taken into account as well.

Finally, relativistic effects should be applied to obtain the correct range. The basic range equation has to be extended by the correction terms:

$$\rho = c \cdot \frac{\Delta t}{2} - \delta\rho_{atm} + \delta\rho_{CoM} - \delta\rho_{bias} - \delta\rho_{rel} - \delta\varepsilon, \tag{2.37}$$

where $\delta\rho_{atm}$, $\delta\rho_{CoM}$, $\delta\rho_{bias}$, $\delta\rho_{rel}$ are the corrections for atmosphere, the satellite's center of mass, a range bias and general relativity, respectively. $\delta\varepsilon$ contains unknown random errors.

3 Jason mission satellites

The Joint Altimetry Satellite Oceanography Network (Jason) is a satellite altimetry mission series. It is a cooperation between the National Aeronautics and Space Administration (NASA) and the French space agency Centre National D'Etudes Spatiales (CNES). The series continues the work of the Topography Experiment (TOPEX)/Poseidon mission and contains as of May 2019 the three altimetry satellites Jason-1, Jason-2 (also referred to as Ocean Surface Topography Mission (OSTM)) and Jason-3. Chapter 3.1 highlights the intention of the satellite missions, Chapters 3.2 and 3.3 describe the satellite bus and payload, respectively. Orbital characteristics are provided in Chapter 3.4. The nominal yaw steering model is explained in detail in Chapter 3.5. Finally, the orbital history of the Jason satellites is illustrated in Chapter 3.6.

3.1 Intention of the missions

The satellite missions Jason-1, Jason-2 and Jason-3 extend the time series of ocean topography measurements started with TOPEX/Poseidon. They provide a continuous data record for a better understanding of the processes and characteristics of the oceans. Multi-decadal ocean topography measurements deliver an insight into long-term changes of the climate and its impact on the sea.

The principal objectives of the missions are (Kramer, 2002):

- Monitoring of global ocean circulation,
- Investigation of the tie between the oceans and the atmosphere,
- Improvement of global climate predictions,
- Monitoring of phenomena such as El Niño/La Niña and ocean eddies,
- Measuring the global sea-level change and
- Improvement of ocean tide models.

Furthermore, measurements of the mean sea surface provide knowledge about the interaction of the Earth's gravity field and the oceans. Additionally, the satellites deliver insight into geophysical processes like plate tectonics, ocean bottom topography, movements of the Earth's mantle and others[7].

The satellite missions deliver the following major data products[8]:

- Sea surface topography
- Significant wave height

[7] https://www.aviso.altimetry.fr/en/missions/past-missions/jason-1/objectives.html, Last access: 2019-06-19
[8] https://directory.eoportal.org/web/eoportal/satellite-missions/j/jason-1, Last access: 2019-06-19

- Surface wind speed
- Ocean tides
- Vertically integrated atmospheric water vapor
- Vertically integrated ionospheric electron content

3.2 Spacecraft

The Jason spacecrafts are mini-satellites and use the Plate-forme Reconfigurable pour l'Observation, les Télécommunications Et les Usages Scientifiques (PROTEUS) bus. This lightweight platform is developed by CNES/Alcatel Space Industries for low-orbit satellite missions. The spacecraft is composed of two half satellites, a payload module and the PROTEUS platform[9,10]. The initial satellite mass is 489.1 kg (Jason-1), 505.9 kg (Jason-2) and 509.6 kg (Jason-3) (Cerri et al., 2019). The mass decreases with satellite lifetime due to the usage of hydrazine propellant for orbit acquisition and maintenance. The consumption causes a variation of the satellite's Center of Mass (CoM). The fuel tanks are constructed so that the CoM only moves along the X direction. The Y and Z coordinates of the CoM with respect to the satellite body frame are always close to zero (see Table 4)[11].

Table 4: Coordinates of the center of mass and the phase center of the laser reflector array with respect to the satellite reference system (Cerri et al., 2019).

		X [m]	Y [m]	Z [m]
Jason-1	Spacecraft CoM	0.9550	0.0000	0.0000
	LRA (Phase center)	1.1710	0.5980	0.6828
Jason-2	Spacecraft CoM	0.9768	0.0001	0.0011
	LRA (Phase center)	1.1940	0.5980	0.6838
Jason-3	Spacecraft CoM	1.0023	0.0000	-0.0021
	LRA (Phase center)	1.1943	0.5980	0.6829

The coarse attitude sensor system is composed of three-axis magnetometers, three magnetorquer bars and eight sun sensors. The determination of the fine satellite orientation is based on a gyro-stellar sensing concept. It consists of two 3-axes CALTRAC™ star trackers (one nominal and one redundant)[8] and three 2-axes gyroscopes (two nominal and one redundant). The star trackers are provided by CAL Corp, Canada. They can observe stars of magnitude 4.3 or brighter[12]. The actuators are represented by four reaction wheels.

Power supply is provided by two silicon solar panels (total array area of 9.8 m², compare Table 5) which produce 450 W (Jason-1) and 580 W (Jason-2 and Jason-3). The rotation axis of the left array is parallel to the −Y axis of the satellite body reference frame and the rotation axis of the right array is parallel to the Y axis. The dimensions of the PROTEUS bus are 1000 mm × 954 mm × 954 mm and the payload module measures 1218 mm × 954 mm × 954 mm. The overall dimensions of the entire satellite are 3360 mm × 9722 mm × 2033 mm. Dimensions are given in the order XYZ in the satellite body coordinate system (see Section 2.1.4). Detailed satellite construction plans are provided in Appendix F.

[9] https://directory.eoportal.org/web/eoportal/satellite-missions/j/jason-2, Last access: 2019-06-19
[10] https://directory.eoportal.org/web/eoportal/satellite-missions/j/jason-3, Last access: 2019-06-19
[11] https://ilrs.cddis.eosdis.nasa.gov/missions/spacecraft_parameters/center_of_mass.html, Last access: 2019-06-19
[12] https://www.jpl.nasa.gov/news/press_kits/jason1launch.pdf, Last access: 2019-06-19

Table 5: Area of the satellite surfaces of Jason satellites (Cerri et al., 2019).

	Spacecraft surface	Area [m²]
Jason-1	±X	1.6500
	±Y	3.0000
	±Z	3.1000
	Left/right solar array	4.9000
Jason-2 and Jason-3	±X	0.7830
	±Y	2.0400
	±Z	3.1050
	Left/right solar array	4.9000

Due to the high amount of radiation exposure, the satellites are planned for a mission duration of three years with a goal of five years. The effective lifetime is exceeded clearly (see Section 3.6). However, the satellite is set to Safehold Mode (SHM) in cases of technical issues with the instruments. The satellite is reinitialized in that state to prevent further damage of the components. No data, including attitude information, is available during the SHM.

Jason-1's entire mission is planned and managed by NASA and CNES. The operational mode of Jason-2 and Jason-3 was transferred to the National Oceanic and Atmospheric Administration (NOAA) and the European Organization for the Exploitation of Meteorological Satellites (EUMETSAT).

3.3 Payload

Each satellite is equipped with a certain composition of different instruments. They provide altimeter measurements, precise orbit determination and auxiliary data. The satellite instruments are shown in Figure 13 and an overview about the payload is provided in Table 6.

The solid-state radar altimeter is the mission's main instrument. It is a dual-frequency instrument using K_u-band (13.575 GHz) and C-band (5.3 GHz) and measures altimeter range (distance between the satellite and the surface of the Ocean), significant wave height, wind speed as well as ionospheric corrections and atmospheric electron content. Jason-1, Jason-2 and Jason-3 are equipped with a Poseidon-2 (CNES), Poseidon-3 (CNES) and Poseidon-3B (EUMETSAT) altimeter, respectively.

The Jason-1 Microwave Radiometer (JMR), Jason-2 Advanced Microwave Radiometer (AMR) and Jason-3 Advanced Microwave Radiometer-2 (AMR-2) are altimeter supporting instruments. They measure the concentration of water vapor in the atmosphere using three channels with the frequencies 18.7 GHz, 23.8 GHz and 34.0 GHz. The first channel delivers corrections for wind-induced enhancement of the ocean surface, the second channel measures atmospheric water vapor emission and the third channel supplies corrections for non-rainbearing clouds[13]. A combination of the three frequency signals provides atmospheric water vapor and liquid water content. Finally, the path delay correction for the altimeter radar signal can be obtained.

The Jason satellites carry three state-of-the-art tracking systems to fulfill the requirement of better-than-1.5 cm radial orbit accuracy (Cerri et al., 2010). The high accuracy is assumed to ensure Geophysical Data Record (GDR) products of high quality. Radial errors have a direct impact on the measurements of the Sea Surface

[13] https://www.aviso.altimetry.fr/en/missions/current-missions/jason-2/instruments/amr.html, Last access: 2019-06-19

Height (SSH). Therefore, Doppler Orbitography by Radiopositioning Integrated on Satellite (DORIS), Global Positioning System (GPS) and Satellite Laser Ranging (SLR) tracking systems are installed on the satellites. The highest POD accuracy is obtained when using the observations of all three tracking techniques.

Doppler Orbitography by Radiopositioning Integrated on Satellite (DORIS) is developed by CNES/Tompson and provides real-time location and precise orbit determination. It is based on a global network of about 60 ground beacons. Jason-1 is equipped with a two-channel, two-frequency (401.25 MHz and 2036.25 MHz) Doppler receiver of the second generation. Jason-2 and Jason-3 carry new generation DGXX and DGXX-S receivers, respectively.

The BlackJack based Global Positioning System (GPS) receivers are delivered by NASA/Jet Propulsion Laboratory (JPL) and support precise orbit determination. The receiver can track 16 GPS satellites simultaneously in dual-frequency mode and provides radial accuracy of 1.5 cm in post-processing. Jason-1 is furnished with a Turbo Rogue Space Receiver (TRSR) and both Jason-2 and Jason-3 with a TRSR-2 (also referred to as Global Positioning System Payload (GPSP)). GNSS provides upside observations of a satellite which reduces the impact of the atmospheric perturbations onto the GNSS signal.

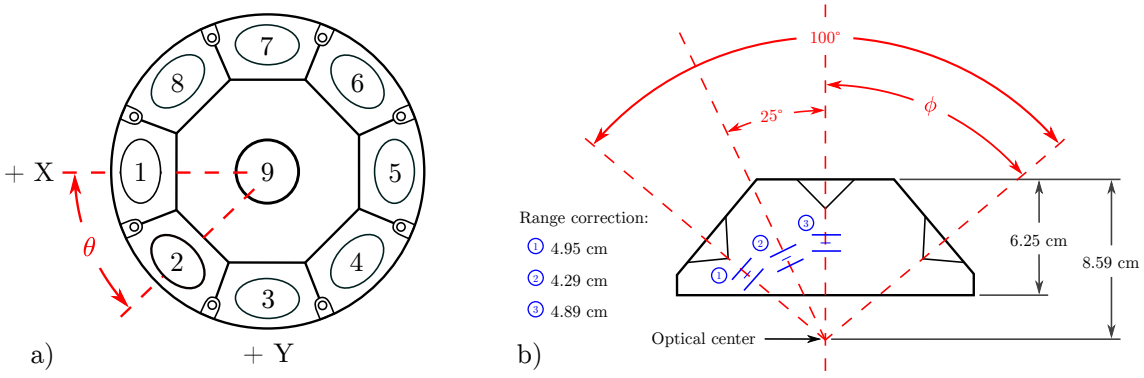

Figure 12: a) Sketch of the retroreflector array of Jason satellites composed of a center cube (9) and eight corner cubes (1−8). b) Dependency of the range correction according to the angle of incidence ϕ of the SLR impulse with respect to the nadir.[14]

All three satellites are equipped with a Laser Retroreflector Array (LRA). It is provided by NASA and represents the reference target for measurements performed by SLR ground stations. The LRA consists of nine quartz corner cubes with a center cube and eight surrounding side cubes (Figure 12)[15]. This arrangement provides an azimuthal field-of-view angle of 360° and approximately 50° around the perpendicular. The instrument is totally passive and is placed on the nadir-oriented side of the satellite to ensure permanent availability for measurements and prevent covering of other satellite components. Highly precise SLR observations are used for calibration and validation of the other tracking techniques. The limited number of ground stations and the sensitivity of the laser beam to the Earth's atmosphere hamper continuous satellite tracking. Therefore, normal points, which are obtained by a combination of multiple single shots, are provided by the ground stations between the SLR station's reference point (coordinates given in the TRF) and the optical center of the LRA (position given in the satellite fixed coordinate system, compare Figure 11). The intersections of the corner cubes' axes define the optical center. The effective range is obtained by shortening the observed distance by an offset depending on the contributing corner cubes. The retroreflectors are optimized for a wavelength of 532 nm (green)[8].

[14] Original version from `https://ilrs.cddis.eosdis.nasa.gov/docs/Jason-1_specs.pdf`, Last access: 2019-06-19

[15] `https://www.aviso.altimetry.fr/en/missions/current-missions/jason-2/instruments/lra.html`, Last access: 2019-06-19

The payload of Jason-2 and Jason-3 contains additional auxiliary instruments. The Environment Characterization and Modelisation-2 (Carmen-2) radiation detector (CNES) determines the influence of space radiation on other instruments of the satellites, particularly on the Ultra Stable Oscillator (USO) of the DORIS system. The USO experiences high radiation exposure especially in the South American Anomaly (SAA). The Light Particle Telescope (LPT) is an instrument of the Japan Aerospace Exploration Agency (JAXA) and supports radiation measurements of Carmen-2. Jason-2 is equipped with a Time Transfer by Laser Link (T2L2) detector for ultra-precise time transfer. It is used for comparison of distant clocks for correct dating of laser pulses.

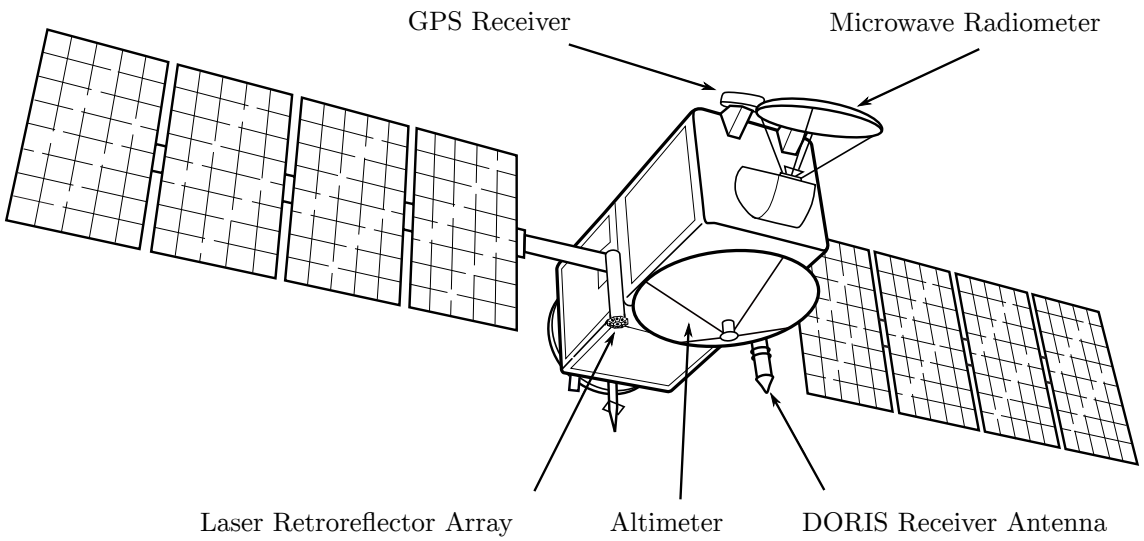

Figure 13: Geodetic payload of Jason satellites.[12]

Table 6: Instrument payload of Jason satellites.

	Radar altimeter	Radiometer	Location systems	Passenger instruments
Jason-1	Poseidon-2	Jason Microwave Radiometer (JMR)	**GPS**: Turbo Rogue Space Receiver (TRSR) **DORIS**: Second generation miniaturized receiver **SLR**: Laser Retroreflector Array	
Jason-2	Poseidon-3	Advanced Microwave Radiometer (AMR)	**GPS**: GPS Payload receiver (GPSP) **DORIS**: DGXX receiver **SLR**: Laser Retroreflector Array	Environment Characterization and Modelisation-2 (Carmen-2) Light Particle Telescope (LPT) Time Transfer by Laser Link (T2L2)
Jason-3	Poseidon-3B	Advanced Microwave Radiometer-2 (AMR-2)	**GPS**: GPS Payload receiver (GPSP) **DORIS**: DGXX-S receiver **SLR**: Laser Retroreflector Array	Environment Characterization and Modelisation-3 (Carmen-3) Light Particle Telescope (LPT)

3.4 Orbital characteristics

The Jason satellites possess the same operational orbit as TOPEX/Poseidon. It is almost circular, non-sun-synchronous and prograde. The orbital characteristics are identical for the three satellites and listed in Table 7.

Table 7: Orbital characteristics of Jason orbits.[16]

	Nominal orbit	Geodetic orbit
Semi-major axis	7714.43 km	7702.437 km
Eccentricity	0.000095	0.00013 to 0.00028
Inclination	66.04°	66.042°
Argument of periapsis	90.0°	
Inertial longitude of the ascending node	116.56°	
Mean anomaly	253.13°	
Reference altitude	1336 km (1309.5 km for Jason-2 since July 2017)	1324 km
Nodal period	6745.72 sec	6730 sec
Repeat cycle	9.9156 days	406.5 days
Geodetic sub-cycles (Bronner and Dibarboure, 2012)		3.97, 10.91, 47.6 and 179.5 days
Number of revolutions within a cycle	127	
Draconitic period (β') (Bronner and Dibarboure, 2012)	117.53 days	117.11 days
Inertial nodal rate	-2.08° per days	
Orbital speed	7.2 km/s	
Ground track speed	5.8 km/s	

The inclination of 66° limits observations to 66° North and 66° South. Nevertheless, the Jason satellites cover about 95 % of the Earth's ice-free oceans and provide a complete global sea surface snapshot about every ten days.

3.5 Nominal yaw steering model

The spacecraft attitude of three-axis stabilized altimetry satellites has to comply with two requirements: a constant nadir (Earth-pointing) orientation of the altimeter boresight and simultaneously a solar-pointing orientation of the solar arrays.

The first prerequisite is necessary to provide altimeter measurements of the ocean surface. The nadir of the satellite is represented by the Z axis in the body reference system and the yaw axis in the local orbital system (hereafter only the yaw axis is mentioned). Consequently, this axis steadily points normal to the reference ellipsoid. This so-called geodetic pointing is realized by roll and pitch angles. To ensure the nadir-pointing direction, only rotations around the yaw axis are allowed.

[16] `https://podaac.jpl.nasa.gov/JASON1`, Last access: 2019-06-19

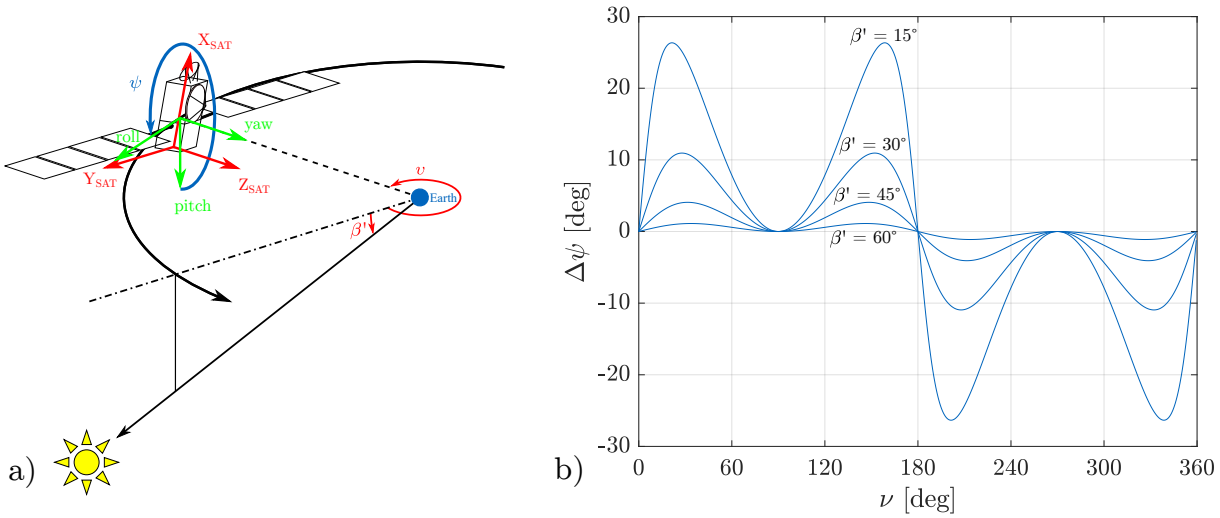

Figure 14: a) Definition of orbit parameter β' and ν.[17] b) Difference between nominal and ideal yaw depending on the angle β'.[17]

The second requirement of continuous Sun-pointing solar arrays provides optimal power supply for the satellite payload. The normal of the solar panels must direct to the Sun. Therefore, the panels rotate around an axis which is parallel to the Y axis of the satellite body system.

To maintain both orientations, a yaw steering algorithm and a solar array pitching algorithm were created by Perrygo (1987) for TOPEX/Poseidon. The attitude regime of Jason satellites is based on these algorithms. The fundamental parameters of the algorithms are β' and ν. The first variable represents the angle between the orbital plane of the satellite and the vector pointing from the Earth to the Sun (elevation of the Sun with respect to the orbital plane, compare Figure 14 a)). The main period of this angle is approximately 117.53 days (draconitic period). The second parameter ν defines the angle between the Earth-Sun vector projected onto the orbital plane and the Earth-satellite vector.

The ideal rotation angle ψ around the yaw axis is defined by the function

$$yaw_{ideal} = \psi_{ideal} = \arctan\frac{\tan\beta'}{\sin\nu}. \tag{3.1}$$

Great values of β' imply a small amplitude of the resulting yaw angle and cause a slow change of the spacecraft attitude. Small β' angles effect a fast variation of the orientation to maintain the Sun-pointing direction of the solar arrays.

Based on the ideal orientation and the angle β', the nominal yaw steering algorithm consists of four yaw modes (Table 8). A sinusoidal yaw steering regime is used when $|\beta'| > 15°$. This value of β' is used for the entire mission of Jason-1 and parts of Jason-2 and Jason-3. After July 14, 2017 and August 12, 2017 the angle is changed to 30° for Jason-2 and Jason-3, respectively (in the following, only 15° is used). In this regime, the satellite performs an oscillating rotation about the yaw axis (see Equation 3.2). This attitude control provides a perpendicular orientation of the solar panel rotation axis with respect to the Sun vector. The X_{SAT} axis of the satellite reference system points away from the Sun. However, the sinusoidal yaw regime is just an approximation of the ideal orientation which results in an offset between both modes of maximum 28° at $|\beta'| = 15°$ (Figure 14 b)).

[17] Original from Cerri et al. (2010)

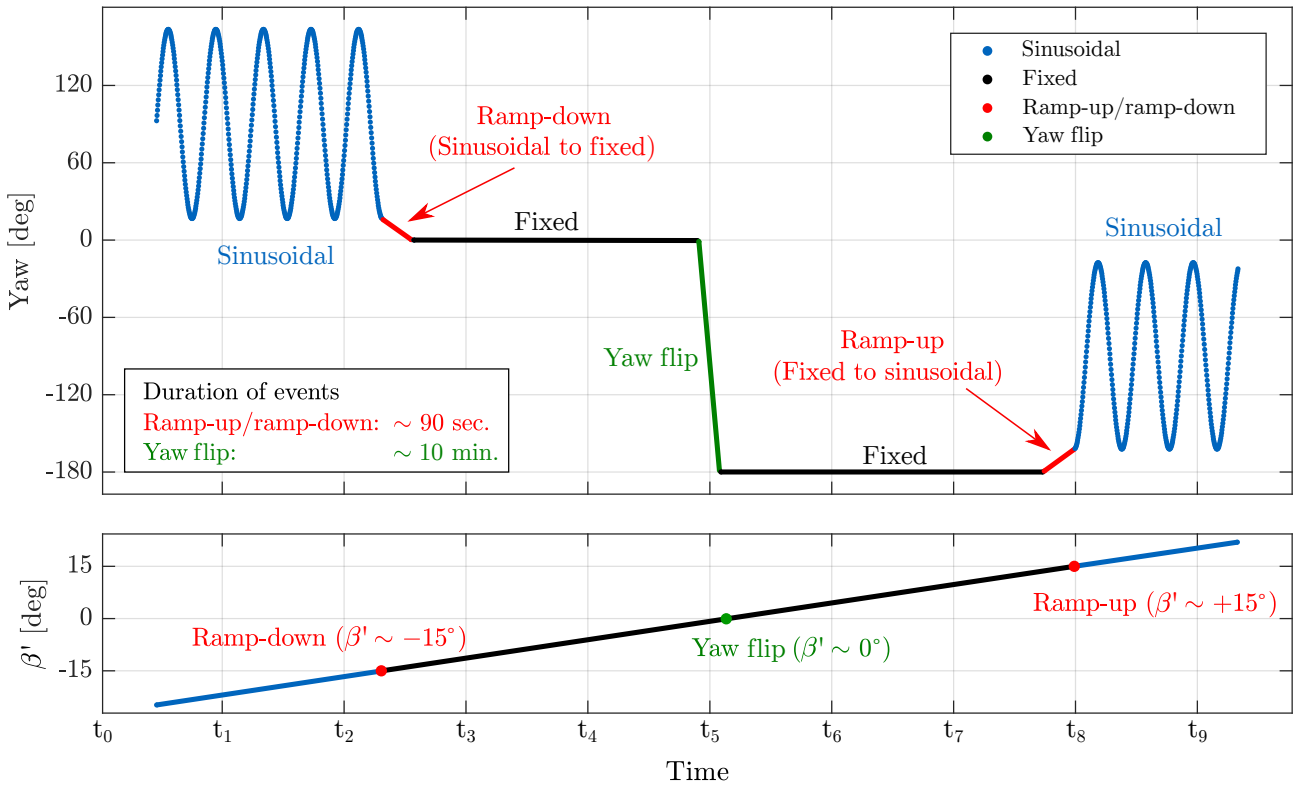

Figure 15: Principle of the nominal yaw steering model of Jason satellites (top) depending on the angle β' (bottom).

$$yaw_{nominal} = \psi_{nominal} = \begin{cases} 90° - (90° - \beta')\sin\nu & \text{, if } \beta' > 15° \\ -90° + (90° + \beta')\sin\nu & \text{, if } \beta' < -15° \end{cases} \tag{3.2}$$

To avoid excessive rotations, the yaw axis is fixed when $|\beta'| < 15°$. The yaw angle is set to $\psi = 0°$ and $\psi = 180°$ at positive β' (spacecraft is flying forward) and negative values (flying backward), respectively. The X_{SAT} axis is oriented with the satellite's along-track direction.

Consequently, a yaw-flip event has to be performed within the fixed-yaw regime (duration of the maneuver: ca. 10 minutes for $\beta' = 15°$ and 19 minutes for $\beta' = 15°$). At approximately $\beta' = 0°$, the spacecraft rotates 180° around the yaw axis. This is required to provide thermal control of sensitive payload instruments and protect coolers from direct solar illumination. The transitions from fixed to sinusoidal yaw and vice versa are called ramp-up and ramp-down events, respectively. Both events do not necessarily start at exactly $|\beta'| = 15°$ but can differ some degrees. The duration of these events is approximately 120 seconds for Jason-1, 90 seconds for Jason-2 and Jason-3 with $\beta' = 15°$ and 130 seconds with $\beta' = 30°$.

To accurately determine the spacecraft attitude, the precise starting and ending moments of these events (flip, ramp-up and ramp-down) are required and provided by the International DORIS Service (IDS)[18]. A schematic illustration of the principle of the nominal yaw steering model is provided in Figure 15.

[18] `ftp://ftp.ids-doris.org/pub/ids/satellites`, Last access: 2019-06-19

Table 8: Modes of the nominal yaw steering model of Jason satellites.

Yaw regime	Occurrence	Description
Sinusoidal	$\lvert\beta'\rvert > 15°$	Yaw sinusoidal law
Fixed	$\lvert\beta'\rvert < 15°$	Yaw = 0° if $\beta' > 0°$ Yaw = 180° if $\beta' < 0°$
Ramp-up	$\lvert\beta'\rvert \geqslant 15°$	Yaw fixed to sinusoidal
Ramp-down	$\lvert\beta'\rvert \leqslant 15°$	Yaw sinusoidal to fixed
Yaw flip	$\lvert\beta'\rvert \approx 0°$	Yaw = 0° if $\beta' > 0°$ Yaw = 180° if $\beta' < 0°$

3.6 Timeline of the missions

The three Jason satellites provide as of May 2019 almost 26 years of high precision information about the Earth. Figure 16 illustrates the duration of the satellite missions and the orbit constellations of the altimetry satellites.

Jason-1 was launched on December 7, 2001 and decommissioned on July 1, 2013. After reaching the operational orbit, Jason-1 was placed about one minute apart from TOPEX/Poseidon on the same orbit for nearly six months. This epoch allowed cross-calibration between the instruments of both satellites. Between September 20, 2002 and the decommissioning of TOPEX/Poseidon (October 9, 2005), these two satellites operated in a tandem mission. Therefore, TOPEX/Poseidon was shifted to an interleaved orbit which resulted in a time lag between the satellites of approximately five days. This orbit provides advantages for real-time applications[19].

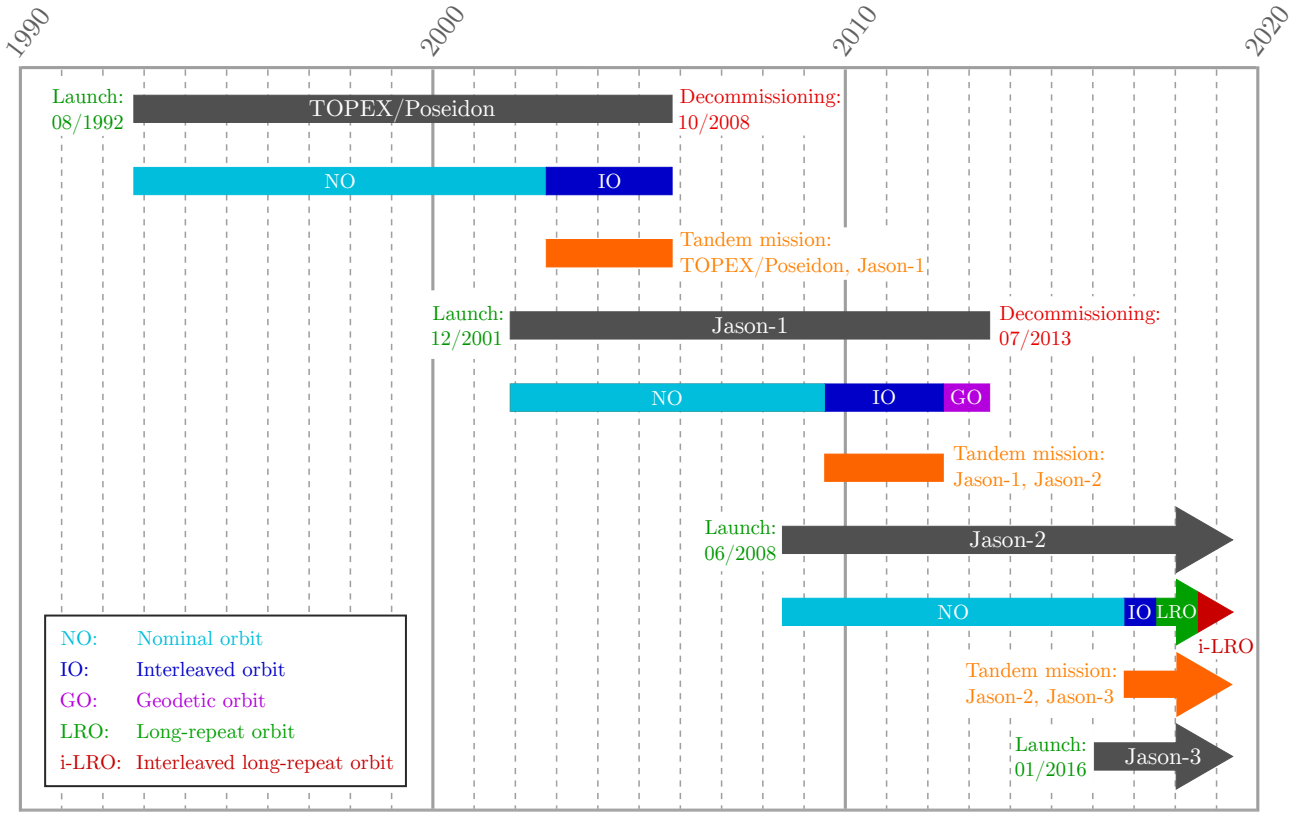

Figure 16: Timeline and orbit constellations of Jason satellites.

[19] https://www.aviso.altimetry.fr/en/missions/past-missions/jason-1.html, Last access: 2019-06-19

Jason-2 was launched on June 20, 2008 and is still operational. Jason-2 was placed about 55 seconds behind Jason-1 on the same orbit. After cross-calibration of the instruments, Jason-1 and Jason-2 were operated in a tandem mission, too. This constellation began in mid-February 2009 and lasted until the end of April 2012. In this time, Jason-1 was moved to the same interleaved orbit which TOPEX/Poseidon formerly used. After the occurrence of several technical problems and putting the satellite into SHM, Jason-1 was decided to be moved to a new drifting geodetic orbit. The operations in the geodetic orbit began on May 7, 2012. The reference altitude was lowered to approximately 1324 km and the satellite's new repeat orbit is 406 days. This orbit provides estimates of the marine geoid and ocean bottom topography (Bronner and Dibarboure, 2012). The new orbit will be the satellite's final graveyard orbit. Simultaneously, the orbit change prevents space debris and collisions with operating satellites in the nominal orbit.

Jason-3 was launched on January 17, 2016 and was located about 80 seconds apart of Jason-2 in the same orbit. The tandem mission of Jason-2 and Jason-3 began on October 14, 2016. Therefore, Jason-2 was moved to the interleaved orbit. On July 10, 2017, Jason-2 was commanded to a new long-repeat orbit (LRO) with an altitude of 1309.5 km[20]. One year later, in July 2018, Jason-2 was shifted to an interleaved LRO[21]. Due to the ongoing satellite mission of Jason-2 and Jason-3 the tandem mission is still operational. However, Jason-2 faces multiple technical issues recently and is often set in to SHM[22].

[20] https://www.aviso.altimetry.fr/en/missions/current-missions/jason-2/orbit.html, Last access: 2019-06-19
[21] https://www.ospo.noaa.gov/data/messages/2018/MSG1911654.html, Last access: 2019-06-19
[22] https://ids-doris.org/satellites/doris-satellite.html?code=JASON-2, Last access: 2019-06-19

4 Methodology

The first Chapter 4.1 provides information about the input data containing the satellite attitude. The detailed analysis and interpolation of attitude quaternions and solar panel angles is explained in 4.2. Chapter 4.3 describes the usage of the obtained attitude information for the computation of precise satellite orbits. To validate the differences between orbits calculated with an attitude model and an observation-based approach, SLR station coordinates are estimated based on the resulting orbits (4.5).

4.1 Description of attitude data

The input data, composed of attitude quaternions and angular positions of the solar arrays, is provided by CNES for the satellites Jason-1, Jason-2 and Jason-3[23]. The data is given in separated daily satellite attitude files and solar panel angle files which individually cover a total of 28 hours (overlap of two hours between two consecutive files). In this work, Jason-1 data is used in the period from December 2001 until June 2013 (entire satellite mission), Jason-2 data from June 2008 until March 2019 and Jason-3 data from February 2016 until March 2019.

The quaternion files provide the four quaternion elements (q_s, q_x, q_y, q_z) of the spacecraft and represent the satellite attitude with respect to the GCRS at epoch J2000.0 (see also Chapter 2.1.1). The solar panel angle files contain the commanded angular positions in radian of the left and the right solar array. The difference between commanded and measured panel positions is less than 1°. Both data sets are given in Temps universel coordonné (engl.: Coordinated Universal Time) (UTC) and parameters are provided approximately every 32 seconds (for detailed format description see Ferrage and Guinle (2009)).

4.2 Data processing

Even both quaternions and solar panel angles are provided every 32 seconds, the point in time is not necessarily the same. For an exact calculation of the perturbing forces and their effect on the satellite surfaces, a complete set of six parameters, four quaternion elements and two rotation angles, must be given at each available epoch. Hence, solar panel angles have to be interpolated at epochs that only occur in the quaternion files and vice versa, quaternion elements have to be interpolated at epochs which merely exist in the rotation angle files. The final products are GPS week-based attitude files which cover a period of nine days. A GPS week starts on Sunday at 00:00 UT, thus, an attitude file contains data from Saturday until Monday after next.

A processing flowchart of the upcoming described MATLAB-based program is provided in Appendix C.

[23] `ftp://cddis.gsfc.nasa.gov/doris/ancillary/quaternions/`, Last access: 2019-06-19

Data loading

Due to above defined conditions, an attitude file is assembled by nine daily quaternion files and nine daily solar panel angle files. For further processing, these 18 relevant files are determined and loaded. In this step, the in-file given UTC time scale is converted to reduced Julian date since epoch J2000.0.

Data analysis

After the data loading process, two separate data sets for both attitude quaternions and solar panel angles are provided. These data sets are subsequently analyzed according to several aspects.

In a first step, epochs are eliminated which occur twice in the data due to the overlapping of consecutive files.

Especially at the beginning of the satellite mission and the initialization of quaternion and solar panel angle determination, or in the case of sensor issues or SHMs, no data is available. Thus, only values of zero or gross errors occur in the data files. These defective epochs are removed as well.

In the following data inquiry, the important characteristic of unit quaternions, possessing the norm of one, is used. Quaternions differing more than $\pm 2 \cdot 10^{-6}$ from this constraint are detected as outliers and accordingly discarded. Figure 17 shows the resulting roll, pitch and yaw angles of corrupted quaternions not fulfilling this requirement (left panel). In cases of such big deviations from the intended norm, a normalization of the quaternions is not possible.

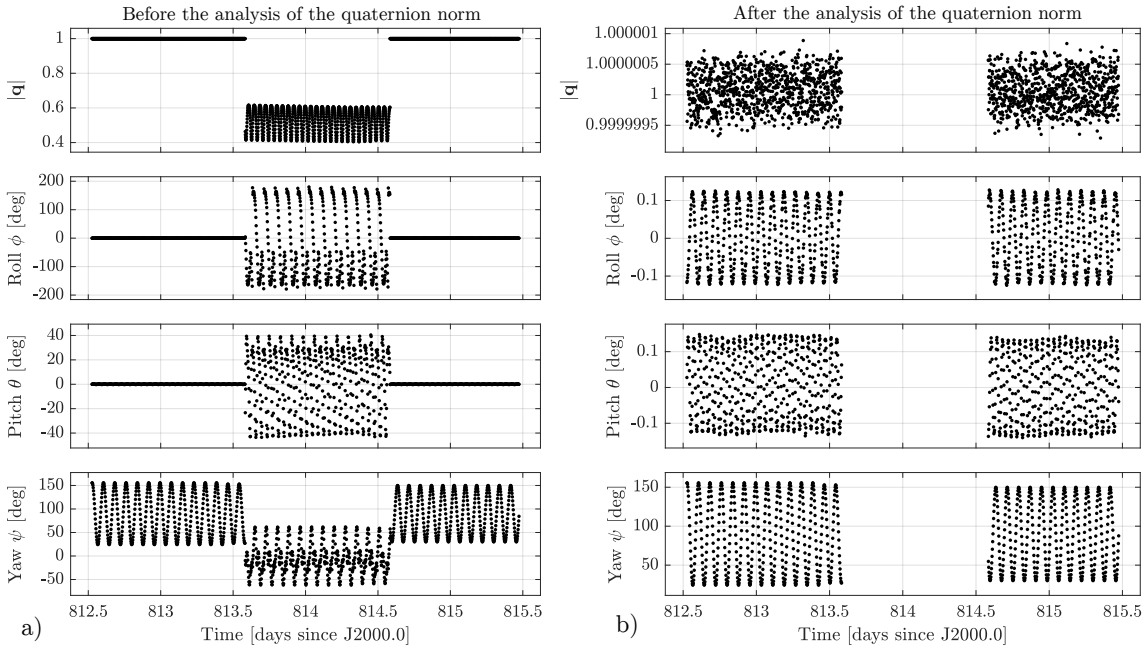

Figure 17: Analysis of the quaternion norm for the detection of outliers: a) Non-normalized quaternions cause extremely oscillating attitude angles. b) The corrected time series show the intended small roll and pitch angles.

Furthermore, the data sets contain periods of increased measurement sampling rate. In these periods, data is not provided at the usual sampling rate of about 32 seconds but every second or fraction of a second. Based on two criteria, a sufficient sampling rate of 32 seconds for further data usage and data storage reduction, these one-second periods are temporally resampled.

After the detection of intervals with high sample rate, the time difference of consecutive epochs is summed up until the threshold of 32 seconds is reached or exceeded. In the latter case, the epoch before passing the threshold

is selected, in the first case, the epoch at exactly 32 seconds is chosen. This practice is applied until the usual sample rate of approximately 32 seconds recommences. All epochs between the selected observations are not needed in the data set anymore but kept stored for the interpolation.

The principle of temporal resampling is shown in Figure 18. The plots cover the content of a quaternion file of 28 hours and depict the time difference δT between two consecutive epochs. The default sampling rate of approximately 32 seconds is shown in black and the interval of high sampling rate in red. The left-handed plots show the original data, the right-handed plots the temporal resampled result. While only covering 52 minutes of the entire period of 28 hours before the resampling, the interval of high sampling rate represents about 50% of the entire data. After applying the above explained procedure, the interval only provides ~3 % of the total amount of data.

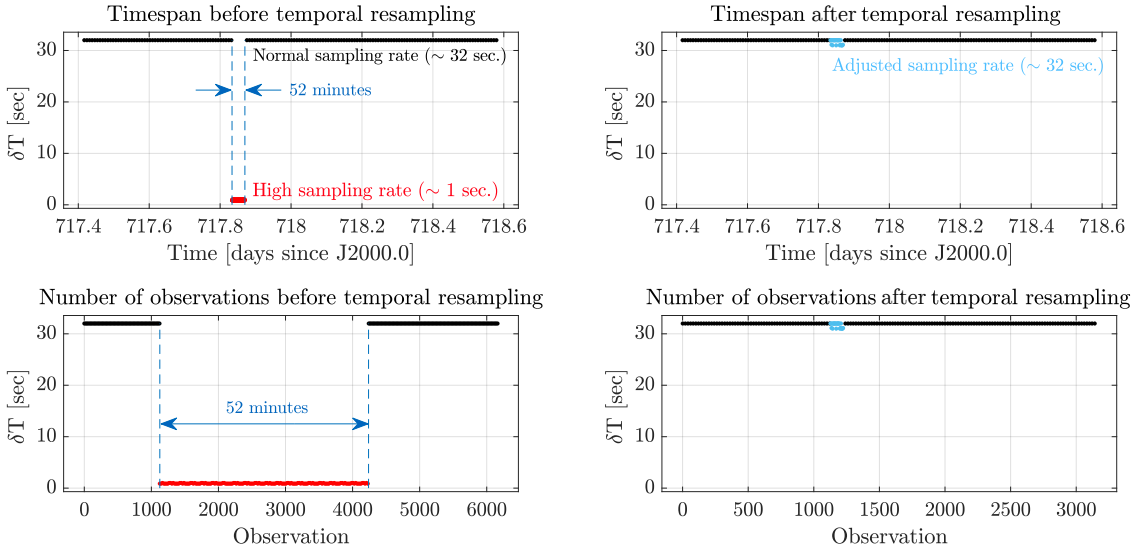

Figure 18: Comparison of the time difference and contributing number of observations of intervals with high sample rate before and after temporal resampling.

To avoid interpolation errors, epochs within data gaps are not interpolated. The threshold for data gaps is set to 66 seconds. This number of seconds allows the interpolation of a missing epoch in intervals of the regular sampling rate of approximately 32 seconds. This time difference is rounded up and applied before and after the missing epoch.

Let the time difference of two consecutive measurements in the solar panel angle data be 70 seconds. Consequently, all epochs in quaternion data, which are located within these 70 seconds, are not interpolated and discarded.

Data interpolation

After removing redundant, defective and unnecessary data, the data at missing epochs is interpolated.

For solar panel angles, linear interpolation is used. Let Θ_1 and Θ_2 be two solar panel angles given at the epochs t_1 and t_2, respectively. t_I is the epoch that is given in quaternion data and located between t_1 and t_2. The interpolated solar panel Θ_I is calculated by

$$\Theta_I = \Theta_1 + (t_I - t_1)\,\frac{\Theta_2 - \Theta_1}{t_2 - t_1}. \tag{4.1}$$

The attitude unit quaternions are interpolated with SLERP (Equation 2.28). This method provides an optimal quaternion interpolation (see Chapter 2.2.5).

To provide best possible interpolation in resampled data intervals, the original high-sampled data is taken into account. Figure 19 b) illustrates the principle of interpolation in periods of high sample rate. Only the scalar part of the quaternions is plotted. Epoch t_I is given in the solar panel angle data but not existing in quaternion data. Thus, a quaternion interpolation is applied at epoch t_I. The red dot represents the erroneous interpolation result when the cyan-colored neighbors in the temporally resampled data are used. The usage of the neighbors from the original, high sampled data (magenta) provides a significantly better interpolation result (green).

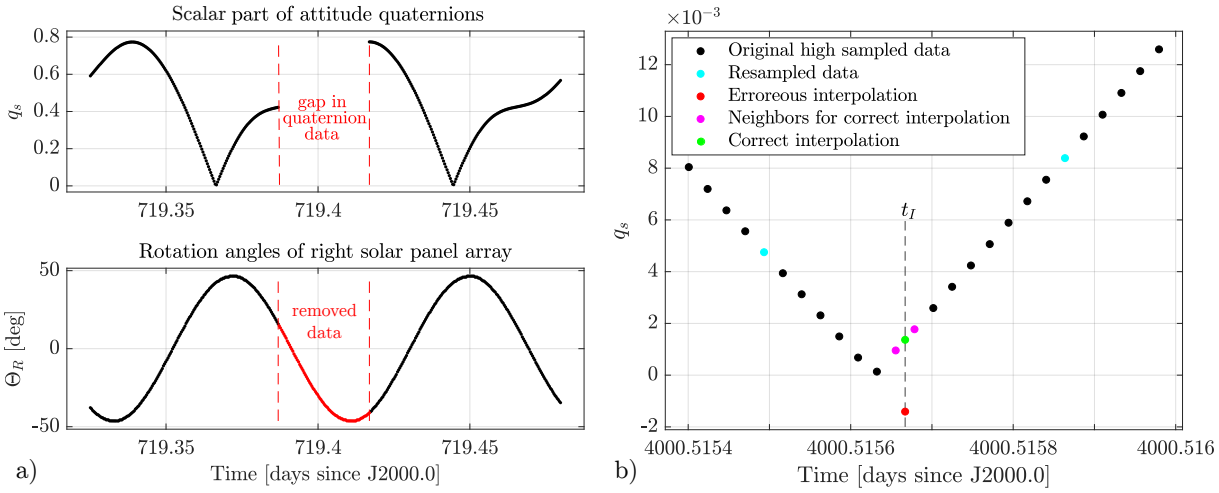

Figure 19: a) Elimination of the solar panel data in the case of a data gap in the quaternion time series.
b) Principle of interpolation in intervals of high sample rate. Difference between the interpolation result using the original and resampled data.

Output data

After attitude quaternion and solar panel angle interpolation, the separate data sets are combined. The resulting attitude file for a GPS week contains the content of nine daily files (220 hours). Detailed data structure and format description of the attitude files is provided in Appendix D.

4.3 Orbit calculation with DOGS-OC

The calculation program of satellite orbits and station coordinates is the DGFI-TUM developed software DGFI Orbit and Geodetic Parameter Estimation Software (DOGS). The software supplies the processing of observations of different geodetic space techniques and the combination of equation systems at different levels of the Gauß-Markov-model (Bloßfeld, 2015). The software consists of three libraries:

- DOGS-OC Orbit Computation library of DOGS
- DOGS-CS Combination and Solution library of DOGS
- DOGS-RI Radio Interferometry library of DOGS

The program DOGS-OC is used for the precise orbit determination of the Jason orbits. Tables 9−12 list the geophysical models and settings used for the estimation of reduced-dynamic SLR-only orbits.

Table 9: Geophysical background models for precise orbit determination of Jason satellite with DOGS-OC at DGFI-TUM.

Precise orbit determination	**Description**
Earth gravity field	EIGEN-6S (Förste et al., 2011) Static part: up to degree/order 120 Time variable part: up to degree/order 50
Lunar gravity field	Up to degree/order 10 (Konopliv et al., 2001)
Third body effect	DE-421: Mercury, Venus, Mars, Jupiter, Saturn, Sun, Moon (Folkner et al., 2008)
Solid Earth tides	IERS Conventions 2010 (Petit and Luzum, 2010)
Permanent tide	Conventional model (IERS Conventions 2010)
Ocean/atmospheric tides	EOT11a (Savcenko and Bosch, 2012) up to degree/order 30 + BB2003 (Biancale and Bode, 2006) + 62 admittance waves (Petit and Luzum, 2010)
Solid Earth pole tide	IERS Conventions 2010
Ocean pole tide	(Desai, 2002)
Non-tidal perturbations	Not applied
Solar radiation pressure	Constant radiation with eclipse modelling
Earth radiation pressure	Albedo and infrared (Knocke et al., 1988)
Atmospheric drag	JB2008 (Bowman et al., 2008) + External geomagnetic storm and solar flux indices
General relativistic correction	Schwarzschild, de Sitter Lense-Thirring (IERS Conventions 2010)
Thermal radiation	Applied[24]

Table 10: Geophysical background models for the calculation of station coordinates in DOGS-OC.

Station background models	**Description**
A priori station coordinates and velocities	SLRF2014 (Version: 24 October 2017)
A priori EOP values	IERS EOP 14 C04 With IERS 2010 daily/sub-daily corrections (sub-daily oceanic tide model (Ray et al., 1994))
Precession/nutation	IAU2000A/IAU2006 model up to degree 10 (Mathews et al., 2002)
Mean pole	Polynomial model (IERS 2010 Conventions)
Solid Earth tidal displacement	Anelastic model (IERS Conventions 2010)
Permanent tide	Conventional model (IERS Conventions 2010)
Ocean tidal displacement	EOT11a (Savcenko and Bosch, 2012)
Atmospheric tidal displacement	S1/S2 tidal model (Ray and Ponte, 2003)
Rotational deformation due to polar motion (Solid Earth pole tide displacement)	Secular pole model (IERS Conventions 2010)
Ocean pole tide displacement	(Desai, 2002)
Non-tidal displacement (atmospheric, oceanic, hydrological)	Not applied

[24] `https://ilrs.cddis.eosdis.nasa.gov/docs/Jason-1_specs.pdf`, Last access: 2019-06-19

Table 11: SLR measurement corrections applied in DOGS-OC for the calculation of Jason orbits.

SLR measurement corrections	**Description**
Tropospheric model for optical signals	Mendes-Pavlis with temperature correction (Mendes and Pavlis, 2004)
Retroreflector and timing instrument correction	Satellite-dependent CoM correction models (Cerri et al., 2019)
Relativistic range correction	IERS Conventions 2010
Station eccentricities	ILRS eccentricity file
Station discontinuities	ILRS discontinuity file
Range and time biases	ILRS data handling file

Table 12: Settings for the orbit integration, empirical parametrization, observation handling as well as utilized satellite characteristics for the POD of Jason satellites.

Orbit integration	
Reference frame of orbit integration	Geocentric Celestial Reference System (GCRS)
Integrator type	Predictor-corrector algorithm of Gauss-Jackson (7^{th} order)
Integrator step size	60 seconds
Integrator relative error bound	10^{-9}
Empirical parametrization	
Arc length	3.5 days (generally, maneuver-dependent)
Atmospheric acceleration scaling factor	Every 12 hours
1/rev empirical (OPR)	1 set per arc (sine/cosine terms; along-, cross-track direction)
Handling of maneuvers	Arc truncated before a maneuver and restarted after the end of a maneuver
Observations	
Observation weight	1 cm, no elevation dependent weighting applied
Elevation cut-off angle	5 degrees
LRA phase center offset	Constant range correction of 4.9 cm subtracted from the computed range
Satellite characteristics	
LRA optical center	see Table 4
Initial mass	see Section 3.2
Initial center of mass	see Table 4
Macro model	CNES Box-wing model (Ferrage and Guinle, 2009)

Initialization of the satellite orbits

To discuss the differences of satellite orbits, high orbit accuracy is an essential prerequisite. Therefore, a set of precise orbit elements at the beginning of each 3.5-days lasting arc is required. In this computation step, the SLR station coordinates are fixed. Additionally, the arcs should not contain any orbit maneuver or outliers. To fulfill these criteria, following processing steps are applied.

The very first arc of each satellite is initialized by externally predicted orbit elements. At the first calculation of each orbit arc, very big outliers of a magnitude of several meters are excluded. After achieving a converging orbit, adjusted orbit elements for the processed arc and starting elements for the next arc are provided. Subsequently, the next arc can be calculated with the estimated Keplerian parameters.

Nevertheless, some arcs diverge and interrupt the orbit generation. Reasons for a termination can be poorly estimated orbit elements, technical problems of an observing SLR station or orbit maneuvers. In the first case, the previous arc has to be recalculated and a new set of orbit elements has to be estimated. Technical issues at an SLR station can cause corrupted observations (e.g., time bias or range bias) which hamper the successful orbit convergence. The more observations such a station is contributing to an arc, the bigger is the disturbing influence on the orbit calculation. Arcs containing orbit maneuvers can also interrupt the orbit computation. Especially orbit inclination maneuvers, which change the orbit geometry by a certain extent, can cause a divergence of the orbit. In those cases, the arc has to be split (described in detail below) or once more, a new orbit arc after the maneuver has to be initialized by external elements.

The generation of the orbit elements of all arcs for the three Jason satellites, which cover a period of about 25 years, is a very time-consuming task. Satellite laser ranging is a very dynamical measuring technique which almost does not permit any automatic orbit initialization but rather requires manual adjustments of the orbits.

After obtaining starting elements of each arc, a maneuver adjustment and a refined outlier detection is applied.

Handling of maneuvers and safehold mode

In case of orbit maneuvers[25, 26], the original arcs of 3.5 days are split into two parts. The preceding arc (new arc 1) ends three minutes before the beginning of the maneuver and the subsequent arc (new arc 2) starts three minutes after the end of the maneuver (see Figure 20, case a)). To avoid new arcs covering less than 24 hours, the short resulting arcs are combined with adjacent regular arcs (cases b) and c)).

In situations of technical issues with the satellite payload, the satellite is set to SHM. In this time, all onboard instruments are shut down. This causes a major impact on the satellite attitude dynamics and control system and the solar arrays which cannot maintain the Sun-pointing orientation. Thus, the calculated atmospheric coefficients are not reliable. Due to these aspects, observations of the satellite in SHM are discarded.

Handling of outliers

After removing the gross outliers in the first calculation of the orbit, the observations are sorted by more stringent aspects. At the orbit calculation, the residuals between the observed and computed satellite position are minimized based on experiences at the ILRS analysis center at DGFI-TUM. If the difference between both satellite positions is bigger than 12 cm, the observation is detected as an outlier and subsequently discarded.

[25] `https://ids-doris.org/doris-system/satellites.html`, Last access: 2019-06-19
[26] `ftp://ftp.ids-doris.org/pub/ids/satellites`, Last access: 2019-06-19

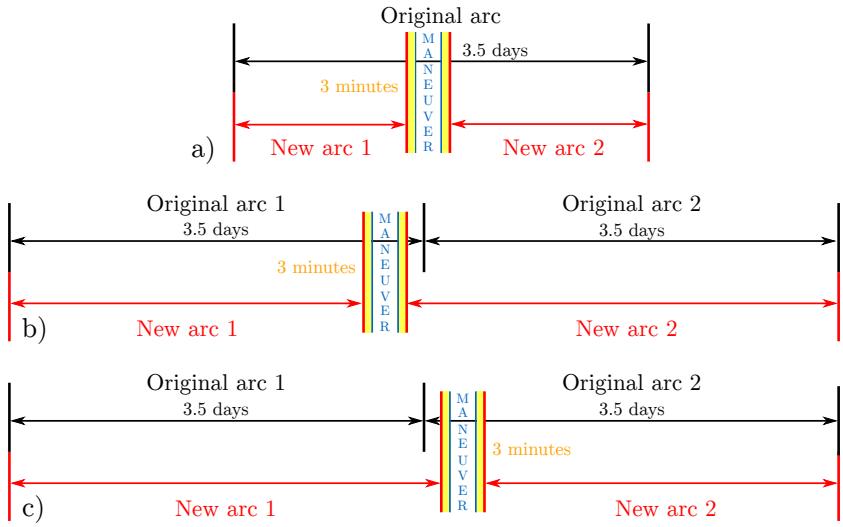

Figure 20: Maneuver handling in DOGS-OC: a) Splitting of a maneuver containing arc into two new arcs. b) + c) Combination of resulting arcs with less the 24 hours with adjacent regular arcs.

Stations with an overall RMS error of 10 cm and more are discarded, too. Furthermore, SLR observations are excluded from the orbit estimation which have an elevation angle of less than 5° above the horizon.

Iterative orbit adjustment

The elimination of observations with an RMS error bigger than 12 cm causes a slight correction of the orbit. As a result, residuals of formerly accepted observations can now be bigger than the threshold and vice versa, formerly discarded observations can fit better to the adjusted orbit. Consequently, the orbits have to be iteratively improved until all outliers are eliminated and only good observations are used for the orbit calculation. Like in the orbit initialization, the SLR station coordinates are kept fixed.

In total, the following intervals of Jason orbits are initialized, edited and iteratively adjusted:

- Jason-1: January 13, 2002 until June 29, 2013
- Jason-2: July 20, 2008 until January 9, 2019
- Jason-3: February 17, 2016 until January 9, 2019

Estimated parameters

Within the POD of each arc, a set of 19 parameters is estimated:

- Initial state vector (semimajor axis, eccentricity, inclination, argument of perigee, longitude of ascending node, mean anomaly)
- Solar radiation pressure scaling factor
- Earth albedo scaling factor
- Atmospheric acceleration scaling factor (every 12 hours)
- Once-per-revolution empirical acceleration of sine + cosine coefficients in along-track + cross-track direction

The calculated orbits are furthermore used to investigate the impact on derived geodetic parameters such as station coordinates when using the observed attitude compared to the nominal attitude.

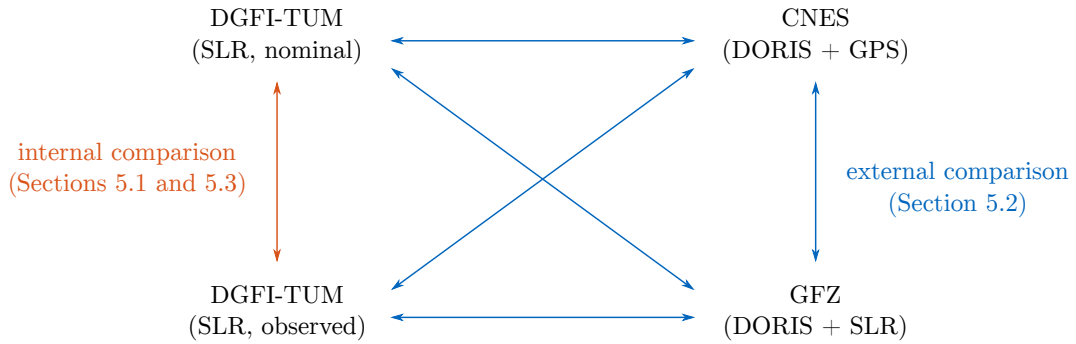

Figure 21: Overview about the orbit products of DGFI-TUM, GFZ and CNES and the comparison of the orbits.

4.4 Orbit validation

For the external orbit validation, DGFI-TUM SLR-only orbits are compared to solutions from GFZ and CNES. The GFZ Jason orbits are based on a combination of DORIS and SLR observations (Rudenko et al., 2018). The CNES orbits are based on DORIS and GNSS data (SLR is only used for orbit evaluation[27])[28].

To ensure the comparison of the same orbit position the time systems are adjusted and converted into UTC. The CNES orbit is given in a temporal resolution of 60 seconds (TAI), GFZ provides satellite position and velocity every 30 seconds (GPS time) and the DGFI-TUM orbits are recalculated with an integrator step size of one second (UTC).

To detect possible orbit systematics, intervals of up to five weeks are chosen at the beginning, the middle and the end of the satellite mission (see Table 13). Figure 21 provides an overview of the internal orbit comparison and external orbit validation. Best positions are provided in the TRF via the SP3c orbit data exchange format. The orbits are transformed from the TRF into the orbital reference system. The first transformation from the TRF into the Celestial Reference Frame (CRF) is realized by the usage of EOPs (compare Figure 11). In the CRF, the difference of the orbit positions is calculated and subsequently transformed into the orbital reference system of one of the satellites. The rotation matrix $\boldsymbol{R}_{CRF}^{ORB}$ is calculated with the formula provided in Equation 2.4. The vector of the orbit difference defines the satellite position of solution two with respect to the origin of solution one at that time.

$$\begin{aligned} \Delta\boldsymbol{X}_{ORB,12} &= \boldsymbol{R}_{CRF}^{ORB,1}\underbrace{\left(\boldsymbol{R}_{TRF}^{CRF}\boldsymbol{X}_{TRF,2} - \boldsymbol{R}_{TRF}^{CRF}\boldsymbol{X}_{TRF,1}\right)}_{\Delta\boldsymbol{X}_{CRF,12}} \\ &= \boldsymbol{R}_{CRF}^{ORB,1} \end{aligned} \tag{4.2}$$

with

$\Delta\boldsymbol{X}_{ORB}$	difference of the satellite position in the orbital reference system (radial, along-track, cross-track),
$\boldsymbol{R}_{CRF}^{ORB,1}$	rotation matrix from the CRF to the orbital system of the first satellite,
$\boldsymbol{R}_{TRF}^{CRF}$	rotation matrix from the TRF to the CRF (realized by EOPs),
$\boldsymbol{X}_{TRF}$	satellite position in the TRF and
$\Delta\boldsymbol{X}_{CRF}$	difference of the satellite position in the CRF.

[27] `ftp://ftp.ids-doris.org/pub/ids/data/POD_configuration_GDRE.pdf`, Last access: 2019-06-19
[28] `https://ids-doris.org/images/documents/Data-Structure-Formats.pdf`, Last access: 2019-06-19

Table 13: Intervals of Jason orbits used for the external validation of DGFI-TUM orbits. The starting and ending epoch is denoted in the format YYYY-MM-DD hh:mm:ss (UTC). No GFZ orbits are available for the last interval of Jason-2 and both intervals of Jason-3.

		Start		End		DGFI-TUM	GFZ	CNES
Jason-1	Interval 1	2002-01-24	00:00:28	2002-02-02	23:59:28	✓	✓	✓
	Interval 2	2007-03-04	23:59:27	2007-04-03	00:51:27	✓	✓	✓
	Interval 3	2012-01-29	00:00:26	2012-02-15	11:59:26	✓	✓	✓
Jason-2	Interval 1	2008-10-26	23:59:27	2008-11-08	01:24:27	✓	✓	✓
	Interval 2	2013-05-27	00:00:25	2013-06-20	17:14:25	✓	✓	✓
	Interval 3	2018-05-06	00:00:23	2018-05-31	17:27:23	✓	✗	✓
Jason-3	Interval 1	2016-02-28	00:00:24	2016-04-02	23:59:24	✓	✗	✓
	Interval 2	2018-05-06	00:00:23	2018-06-09	23:59:23	✓	✗	✓

The orbit differences in the nominal approach $\Delta \boldsymbol{X}_{ORB,N}$ and the observed attitude $\Delta \boldsymbol{X}_{ORB,O}$ are subsequently statistically investigated by following step:

1. Calculation of the overall mean and the standard deviation of the orbit differences calculated at each epoch i (analog for observed)

$$\mu_N = \frac{1}{n}\sum_{i=1}^{n} \Delta \boldsymbol{X}_{ORB,N,i} \qquad \text{and} \qquad \sigma_N = \sqrt{\frac{1}{n-1}\sum_{i=1}^{n} |\Delta \boldsymbol{X}_{ORB,N,i} - \mu_N|^2} \tag{4.3}$$

2. Absolute and relative change between nominal N and observed O

$$\begin{aligned} &\text{Absolute:} && \Delta\mu_s = |\mu_Q| - |\mu_N| && \text{and} && \Delta\sigma_s = \sigma_Q - \sigma_N \\ &\text{Relative:} && \Delta\mu_p = \left(|\mu_Q| - |\mu_N|\right)/|\mu_N| \cdot 100 && \text{and} && \Delta\sigma_p = \left(\sigma_Q - \sigma_N\right)/\sigma_N \cdot 100 \end{aligned} \tag{4.4}$$

4.5 Computation of station coordinates using DOGS-CS

In a last step, the effect of the observation-based orbits on derived geodetic parameters is investigated. Therefore, the Combination and Solution library of DOGS (DOGS-CS) is used. The estimation of geodetic parameters such as coefficients of the Earth's gravity field model or EOPs is not suggested due to a too high degree of correlation in the case of a single-satellite solution (Bloßfeld et al., 2018). Hence, only time series of estimated station coordinates are analyzed.

First, datum-free Normal Equations (NEQs) are computed with the Orbit Computation library of DOGS (DOGS-OC) based on the last iterated orbit solution described before. These are subsequently used in DOGS-CS for the following processing steps:

1. Accumulation of all arcs within one GPS week (computation of station coordinates and coefficients of the gravity field model at the mid of the week and equalization of the daily provided EOPs to the same values at the boundaries of the arcs).
2. Reduction of the satellite specific parameters (initial state vector, solar radiation pressure and Earth albedo scaling factor) in the NEQs.
3. Elimination of the empirical accelerations (once-per-revolution estimated sine + cosine coefficients in cross-track direction). This step provides a reduction of the correlation between coefficients of the Earth's

gravity field and EOPs (Bloßfeld et al., 2014). This step is somehow redundant to step 5 but allows to estimate reliable gravimetric parameters and EOPs if step 5 is omitted.

4. Application of constraints to internal orbit parameters such as atmospheric scaling factors and the remaining empirical along-track accelerations. Additionally, reduction of these parameters in the NEQs.
5. Elimination of the coefficients of the Earth's gravity field model and the EOPs.
6. Setup and addition of geodetic constraints for the orientation of the TRF (No-Net-Rotation (NNR) conditions based on a network of selected stations in the DTRF2014 (Seitz et al., 2016)).
7. Inversion of the constrained NEQs.

The obtained products are time series of weekly SLR station coordinates in the TRF which observed the satellites Jason-1, Jason-2 or Jason-3. The station position time series are transformed into a local horizontal system (N = North, E = East, U = Up), detrended, and outliers are rejected. Based on the resulting coordinates, a spectral analysis for selected stations is applied. The criterion for the choice of a station is a continuous tracking of all three Jason satellites.

Additionally, statistical quantities of the weekly least square adjustment procedure (e.g., the squared sum of the corrections and of the residuals as well as the a posteriori variance factor $\hat{\sigma}_0^2$) are investigated.

5 Results and discussion

In this chapter, the research results are provided and interpreted. The first Section 5.1 discusses the orbit differences caused by the usage of the nominal yaw model or the observed attitude for precise orbit determination. The external orbit validation with GFZ and CNES products is given in 5.2. Finally, the differences of the estimated SLR station coordinates and of the statistical characteristics of the least square adjustment are illustrated in Section 5.3.

5.1 Comparison of the nominal and observation-based orbits

With DOGS-OC, the satellite orbits of the Jason missions are calculated for a timespan of about 25 years. As described in the previous chapter, the orbits do not contain orbit maneuvers or outliers in SLR residuals and are iteratively adjusted. Erroneous observations are excluded from the orbit calculation according to the prior-mentioned criteria. Simultaneously, the maximum number of good observations is used for the orbit determination.

The percentage of excluded observations for each orbital arc is illustrated in Figure 22. For Jason-1, the number of excluded observations alternates on average from about 3-4 % up to 10 %. A clear improvement of the observation quality can be seen for Jason-2 since the beginning of 2010. The mean percentage decreased from about 7.7 % to about 1.5 %. This positive trend is continued with Jason-3. Enhanced tracking equipment and improved satellite payload might be one of the main reasons for this behavior.

Table 14 provides information about the eliminated observations per arc. The mean percentage of eliminated observations decreases with every satellite mission from Jason-1 (3.26 %) to Jason-3 (0.66 %). With an average of 1663 normal points, Jason-2 is tracked most of all three satellites.

The arc-wise orbit RMS using the nominal yaw steering model for the attitude realization is shown is Figure 23. The values reach from the sub-centimeter up to almost 5 cm. The 60-day average (about half the draconitic

Table 14: Results of the orbit comparison between nominal and observation-based attitude realization of the Jason satellites. The improvement of the arc RMS denotes the percentage of arcs which possess a smaller RMS using attitude observations. The overall mission improvement is given in the last column.

	Observations		Mission RMS [cm]		Improvement (N → O)	
	Mean used	Mean excluded	Nominal	Observed	Mission RMS	No. of arcs
Jason-1	1457	3.26 %	2.1486	2.0213	5.93 %	73.92 %
Jason-2	1663	2.41 %	2.1865	2.0056	8.27 %	84.65 %
Jason-3	1470	0.66 %	2.1753	2.0772	4.51 %	75.57 %
		See Fig. 22	See Fig. 23		See Fig. 25	

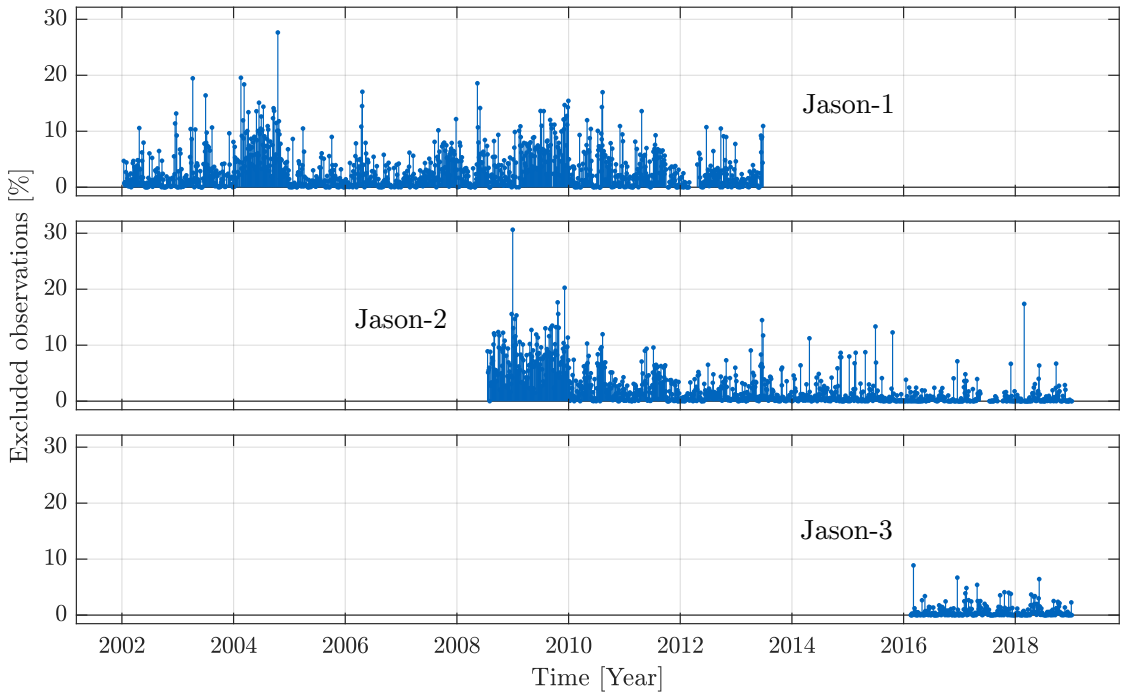

Figure 22: Percental amount of eliminated SLR observations per arc for the precise orbit determination.

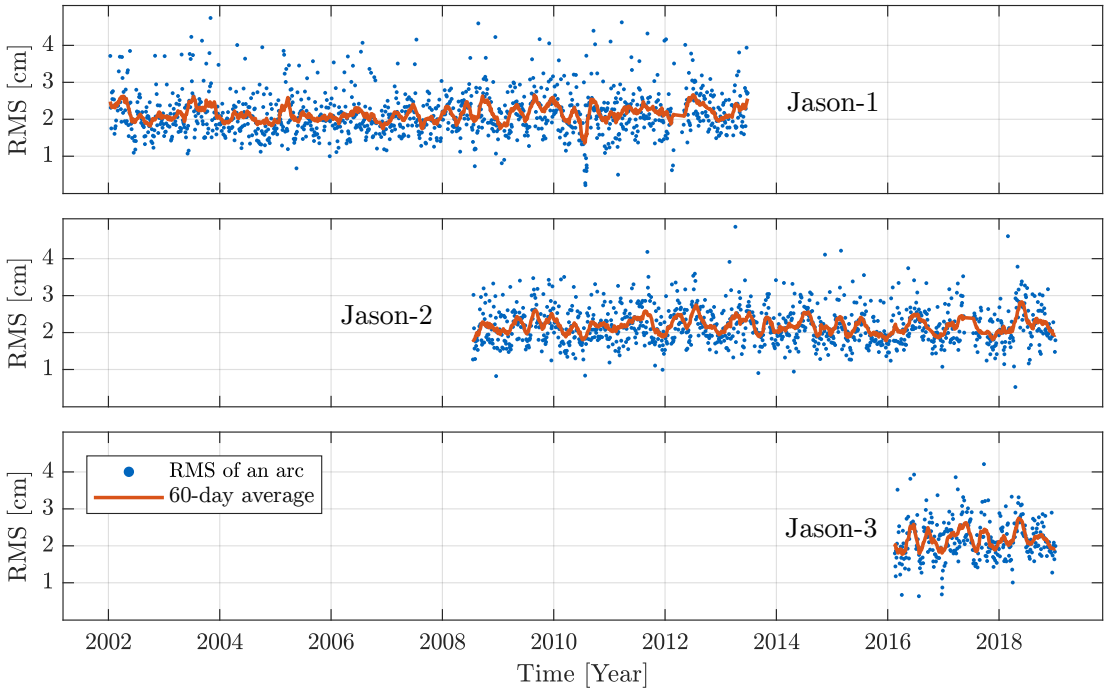

Figure 23: Arc-wise RMS of SLR fits of the SLR-only DGFI-TUM orbits for the Jason missions.

period of the Jason satellites) is located between 1.5 cm and 3 cm for all satellites. An RMS over 4 cm can be a result of a time or range bias in the SLR observations. Bad weather conditions at one satellite pass can also affect the accuracy of the entire station performance. In this case, multiple SLR observations have an RMS up to 12 cm or a station up to 10 cm. In both situations, the observations are not rejected and, thus, increase the overall arc RMS. Very short arcs (24 hours up to 48 hours, between satellite maneuvers) have significantly less SLR observations which results in an RMS up to 1 cm.

The relative change of the SLR fit RMS between both attitude realizations is given in Figure 24. Blue values

imply a smaller orbit RMS when using attitude quaternions and solar panel angles (improvement). The RMS decreases from nominal orbits to observation-based orbits according to the blue values. Vice versa, the RMS grows for the red colored arcs (degradation from nominal to observation-based orbits).

For all three satellites, most arcs have a smaller RMS error when realizing the satellite orientation by the observed attitude information. As shown in Table 14, 74 % of the arcs of Jason-1, 84 % of Jason-2 and 75 % of Jason-3 are better compared to the orbits calculated with the nominal yaw steering model. The biggest relative improvement and the smallest mean orbit RMS is obtained for the Jason-2 mission (compare Figure 25). The overall mission RMS decreases from 2.18 cm to 2.00 cm (-8.27 %). Jason-1 changes from 2.14 cm to 2.02 cm (-5.92 %) and Jason-3 from 2.17 cm to 2.07 cm (-4.51 %). Jason-3 has the smallest improvements and the biggest mean orbit RMS of the Jason satellites.

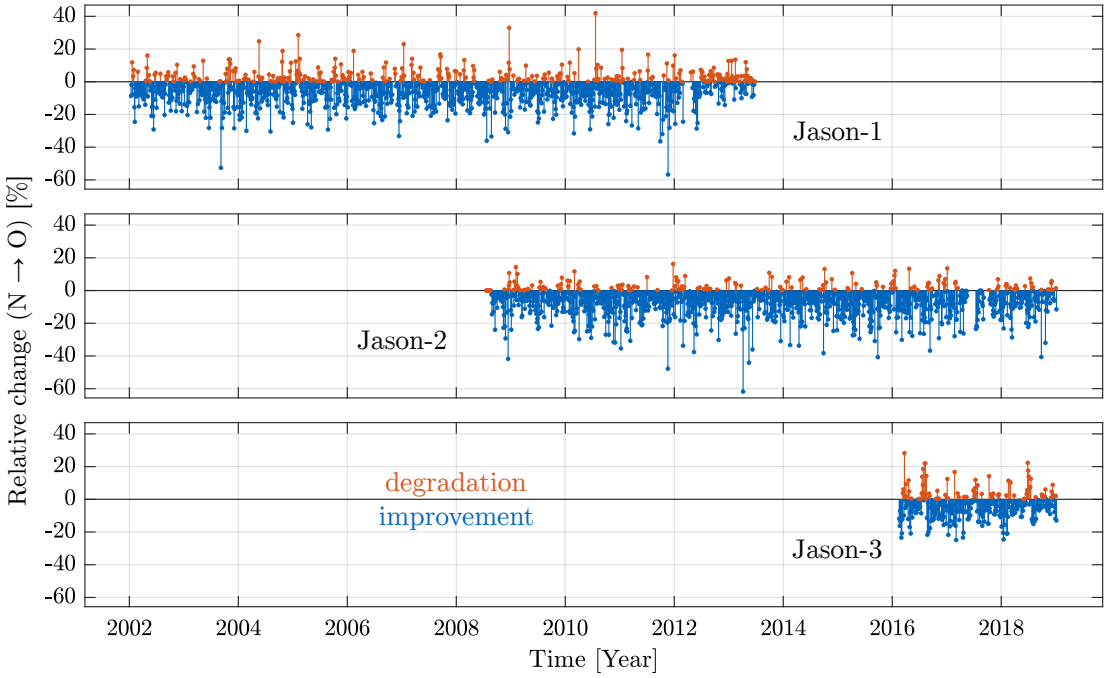

Figure 24: Relative change of the arc-wise RMS of SLR fits from nominal to observation-based attitude realization.

This effect might be caused by the high observation quality or errors in the background models, which are used to calculate the perturbations of the satellite or the displacements of station coordinates. The models (compare Tables 9 and 10) are mainly published until 2014 and generated with observation data until the publication year. In the case of Jason-3 (satellite launch and start of the mission in early 2016), these models only provide predictions. These models do not consider unforeseeable, unique or abrupt event (e.g., a displacement in the SLRF2014 due to an earthquake close to an SLR station after 2016 or increased solar activity).

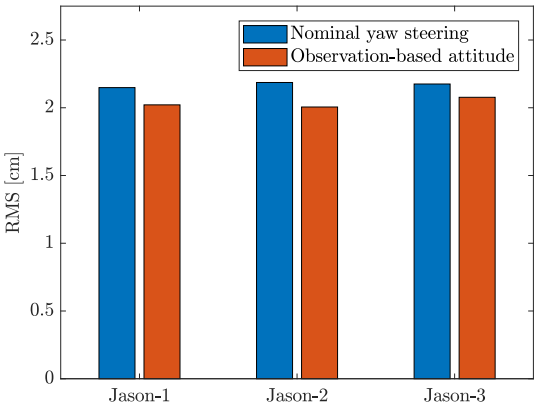

Figure 25: Mission orbit RMS of SLR fits of the Jason missions for the nominal and observation-based attitude approach.

Estimated parameters

The parameters, that are estimated within the orbit computation, are an indicator of the orbit accuracy, too. The mission averaged parameters solar radiation pressure, Earth albedo and atmospheric drag scaling factors, as well as the four empirical accelerations are illustrated in Figure 26. Each parameter has an optimal target value which is represented by a reference polygon (black). The estimated value is shown for the orbits calculated with the nominal yaw steering model (blue) and the observation-based attitude realization (red). Well estimated parameters form a polygon close to the reference polygon.

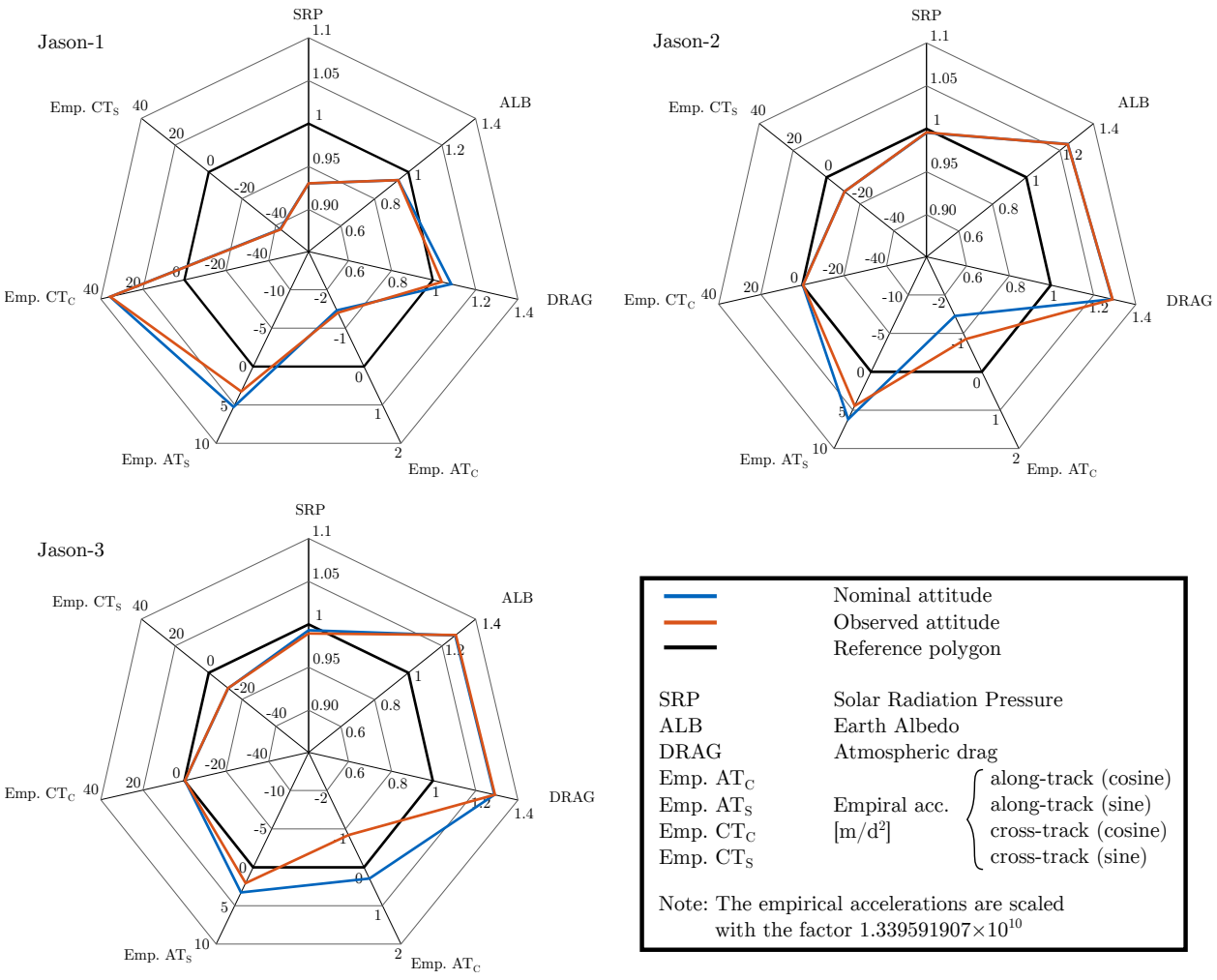

Figure 26: Estimated parameters within the POD of the Jason satellites. Quality of the parameters of the nominal approach (blue) and observed attitude (red) with respect to the ideal parameter value (black).

The solar radiation pressure for Jason-2 and Jason-3 is estimated more accurately compared to Jason-1. The opposite situation is given for both, the Earth albedo and atmospheric drag scaling factors. The empirical accelerations in the along-track direction of Jason-3 show smaller offsets to zero than those of the other satellites. This implies, that these parameters do not have to absorb that many accelerations which are not modelled by the remaining parameters. The cross-track component differs most between the satellites. The cosine parameter is close to zero and the sine component is at about -1.3007·10^{-9} m/s² for Jason-2 and Jason-3. The accelerations for Jason-1 are clearly bigger which indicates strong unmodelled (perturbing) accelerations in these directions. Remarkable aspects of the cross-track accelerations of Jason-1 are large values (compared to Jason-2 and Jason-3) and the opposite sign between the sine and the cosine component. The values for the nominal orbits are 4.8252·10^{-9} m/s² and -5.8724·10^{-9} m/s² for cosine and sine, respectively.

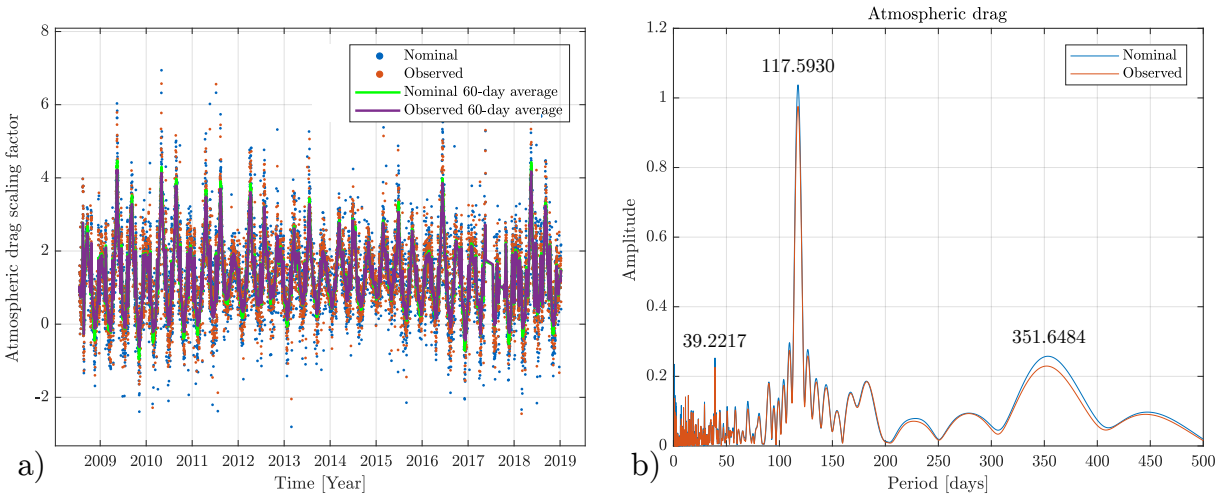

Figure 27: a) Estimated atmospheric drag scaling factor of Jason-2 for the nominal and observed attitude approach. b) Amplitude of the drag signal.

Furthermore, the parameters are investigated concerning systematic frequencies. Exemplary, the atmospheric drag scaling factor of Jason-2 is shown in Figure 27. The estimated arc-wise factors scatter in both orbit solutions from about -2.4 to 6.9. An optimal value for this parameter is close to 1.0 and negative values are not plausible (the atmosphere is always a decelerating perturbation). The overall mission average slightly increases from 1.29411 (nominal) to 1.3010 (observed). The 60-day average of the nominal arcs (green) contains greater amplitudes than the observation-based approach. Both time series clearly contain a strong periodic signal. A frequency analysis shows main periods at 117.59 days (draconitic period of the Jason satellites) and harmonics of this period at 351.65 days (times three) and 39.22 days (one third). The observation-based attitude modelling mitigates the signal amplitude for about 6 % (117.59 days) and 10 % for both draconitic harmonics. Further investigations should clarify why the draconitic harmonic is the most prominent signal in the atmospheric drag scaling factor time series of Jason-2 since other orbit parameter time series do not show such a significant draconitic signal content.

5.2 External orbit validation

Figure 28 shows orbit differences in the orbital reference system RTN exemplarily for the third Jason-1 interval. In all three comparisons, the smallest differences occur in the radial component with a range of ±5 cm. The cross-track and along-track positions deviate between ±10 cm and ±20 cm, respectively. Additionally, these two components show different behavior especially at the beginning and the end of the interval. This concludes a better coincidence of the GFZ and CNES orbits and differences in the precise orbit determination of DGFI-TUM. This investigation shows that the DGFI-TUM SLR-only Jason orbits are already of good quality compared to orbits computed by a combination of geodetic space techniques.

Detailed results of the external orbit validation are illustrated in Figure 29. In each satellite interval, the component-wise determined orbit differences (A = along-track, C = cross-track, R = radial) are averaged (Equation 4.3). The mean values and the standard deviation of the orbit difference with the usage of nominal DGFI-TUM orbits is provided in a). The orbit mean agrees in most selected orbit intervals between the different solutions. Only Jason-1 orbits contain mainly in the along-track direction larger offsets up to 2.5 cm. The comparison of DGFI-TUM and CNES (red) Jason-2 orbits contains the smallest differences.

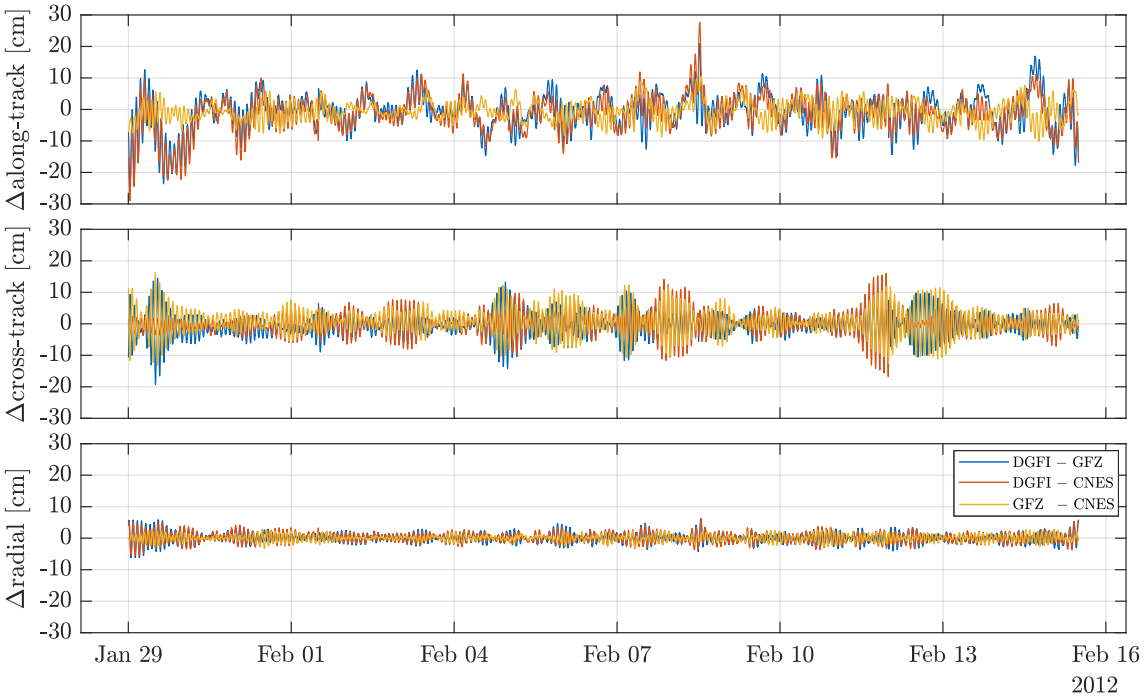

Figure 28: Jason-1 along-track, cross-track and radial orbit differences in the orbital reference system between the solutions of DGFI-TUM, GFZ and CNES.

The standard deviation of the orbit offsets implies that the radial component between the orbits fits the best. Vice versa, the along-track direction contains the largest discrepancies. Among the institute comparisons, the orbit solutions of GFZ and CNES are closer to each other compared to the DGFI-TUM orbits. This is mainly explained by the observation data used for precise orbit determination. The DGFI-TUM provides SLR-only orbits while the other products are computed with a combination of two geodetic space techniques (compare Figure 21). Furthermore, GPS and DORIS are continuous tracking systems and provide a clearly bigger amount of observations. The average number of 1663 SLR observations used for an orbit arc of Jason-2 (most tracked satellite) compared to 61266 DORIS observations is an important aspect for orbit accuracy. Additionally, the more homogeneous distribution of tracking stations in the case of DORIS[29] as compared to SLR also affects the orbit quality (compare Appendix E).

The absolute and relative changes from nominal to observation-based DGFI-TUM orbits are shown in Figure 29 b) and c), respectively. Negative values imply an improvement in the orbit comparison from nominal to observed. For GFZ and CNES, only one type of orbit is provided. Therefore, no orbit differences can be determined between these institutes, but only DGFI-TUM orbits can be compared considering better or less accordance to these orbits.

In general, the biggest absolute changes are obtained in the along-track direction. The orbit difference of Jason-1 is about 0.2-0.45 cm smaller. Jason-3 orbit positions differ in the mean by about 0.5 cm more in the observation-based attitude approach. However, the standard deviation is for almost all satellites and components smaller compared to nominal orbits. For all satellites, the biggest changes are obtained in the cross-track direction (up to 1.2 cm).

Despite of changes in the millimeter range, the other components improve by the same relative amount (bottom plot). The mean improvement of the standard deviation from nominal orbits to observations-based orbits is

[29] `https://ids-doris.org/doris-system/tracking-network/site-logs.html`, Last access: 2019-06-19

about 9.96 %. This indicates, that the usage of attitude observations for precise orbit determination enhances the orbit accuracy and thus, the SLR-only orbits fit better to solutions using continuous tracking techniques. Additionally, this result suggests the usage of the observations-based method by the other institutes.

The change of the orbit mean differences does not show a consistent behavior. Note here the logarithmic scale of the plot. The biggest changes of up to 500 % appear in Jason-2 intervals. This is caused by changes from 0.018 cm to -0.11 cm.

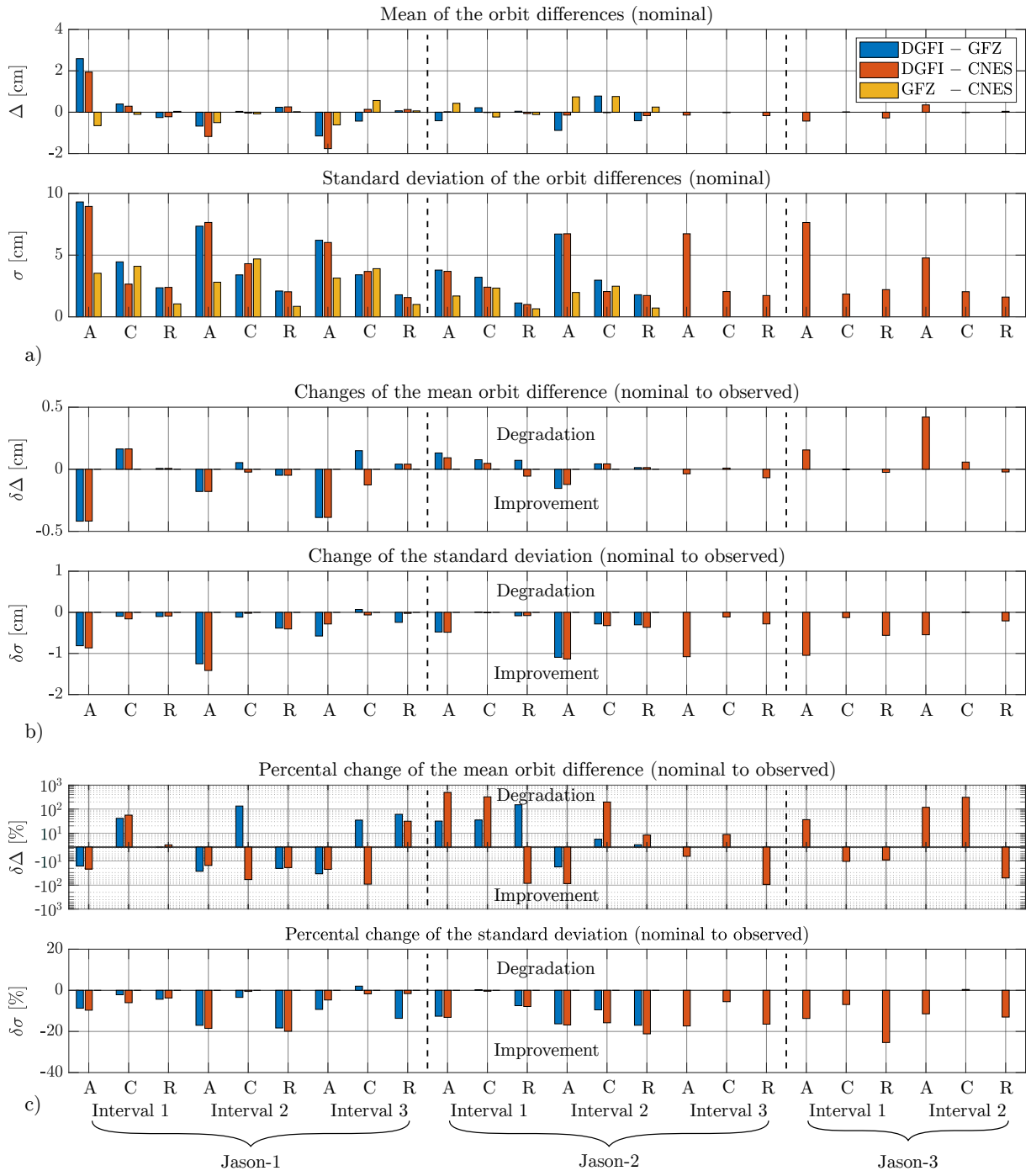

Figure 29: Results of the external orbit validation of the orbit components A = along-track, C = cross-track and R = radial for the intervals defined in Table 13. a) Mean and standard deviation of the component-wise orbit differences using DGFI-TUM orbits. b) Absolute and c) relative changes between the nominal and observation-based attitude realization.

5.3 Effect on station coordinate time series

The following investigation is based on the DGFI-TUM SLR-only nominal and observation-based orbits. The impact on arc-wise estimated SLR station coordinates is compared using both attitude realizations. The results of the spectral analysis of the SLR stations Graz, Greenbelt, Hartebeesthoek, Mt. Stromlo, Potsdam, Yarragadee and Zimmerwald are illustrated in Figure 30.

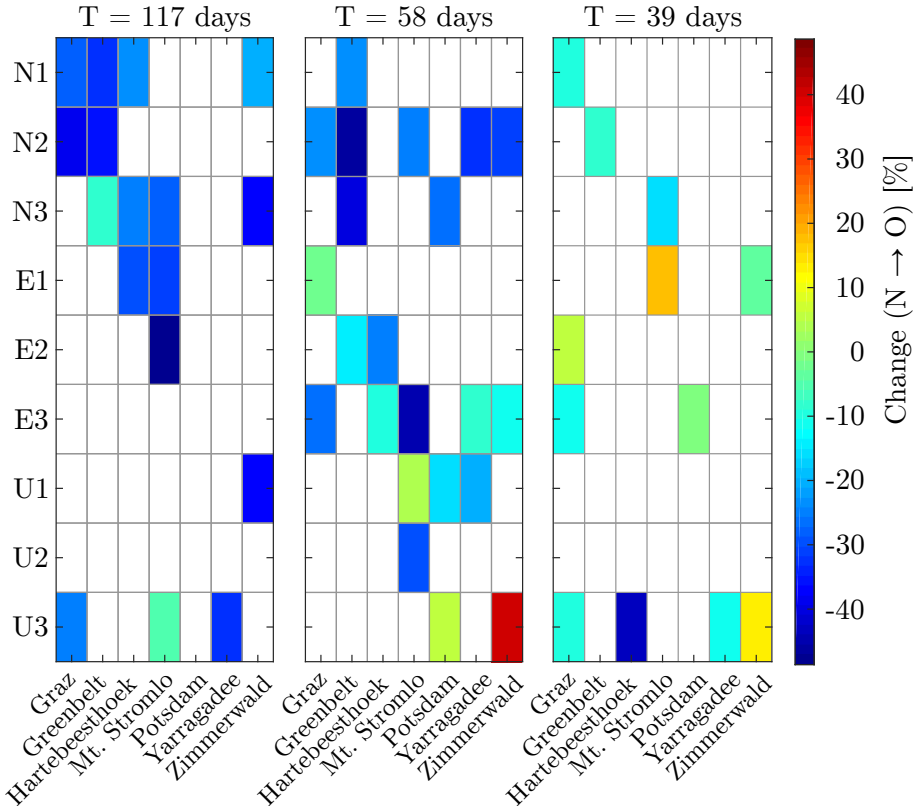

Figure 30: Relative change of the frequency amplitudes contained in the time series of estimated SLR station coordinates (N = North, E = East, U = Up). The harmonics of the draconitic period (117.53 days) of Jason satellites (1,2,3) are investigated. White-colored components do not contain draconitic harmonics.

As shown in the preview chapters, a periodic signal coinciding with the draconitic period of the Jason satellites is contained in the satellite orbits (by a larger extent in the nominal orbits). Thus, the fundamental period for this investigation is the draconitic period T ≈ 117 days and its harmonics 58 days (1/2 T) and 39 days (1/3 T). The rows in the figure represent the station components observed by the Jason satellites (e.g., N1 is the station's North component derived from Jason-1 observations). Colored elements indicate a periodic signal in the station time series. The specified periods occur in 27 % (17 of 63 for T), 35 % (1/2 T) and 19 % (1/3 T) of the station components. The contribution of affected coordinates is not homogeneous. The draconitic period occurs mainly in the North direction of the stations while the harmonics are present is all components. 30 % of the affected components are contributed by Jason-1 (N1 + E1 + U1), 25 % of Jason-2 and 45 % of Jason-3.

The colors define the relative change between the attitude approaches. The amplitude of blue-marked components is smaller using attitude observations for precise orbit determination. The improvements are up to 40 %. However, some directions show slightly increased amplitudes with a maximum of approximately 40 % in the Up coordinate of station Zimmerwald. The average amplitude reduction of each period is 29 % (T), 19 % (1/2 T) and 7 %

Table 15: Changes in the parameters a posteriori variance factor $\hat{\sigma}_0^2$, the sum of the squared corrections $v^T Pv$ and of the residuals $l^T Pl$ occurring at the estimation of SLR station coordinates based on either the nominal or the observation-based orbits.

	Jason-1			Jason-2			Jason-3		
	Nominal	Observed	N → O	Nominal	Observed	N → O	Nominal	Observed	N → O
$\hat{\sigma}_0^2$	2.8885	2.5451	-11.89 %	2.9733	2.4120	-18.88 %	2.5395	2.2887	-9.88 %
$v^T Pv$	16069	14388	-10.46 %	19165	15875	-17.17 %	16655	15359	-7.78 %
$l^T Pl$	8629	7671	-11.10 %	10244	8344	-18.54 %	7612	6866	-9.80 %

(1/3 T). No signal of draconitic harmonics is contained in the white-colored components.

These results show that the observation-based attitude realization benefits the accurate estimation of the SLR station coordinates. The reduction of orbit depending periods in the station positions allows better separation of geophysical and orbit originating signals.

The empirical quantities of the least square adjustment derived from the estimation of weekly determined SLR station coordinates are provided in Table 15. All three parameters (a posteriori variance factor $\hat{\sigma}_0^2$, the sum of the squared corrections $v^T Pv$ and of the squared residuals $l^T Pl$) improve from nominal to observation-based orbits for about 10 % (Jason-1 and Jason-3) and almost 20 % for Jason-2. A smaller variance factor implies a better fitting functional model of the estimation based on the provided observations (compare Figure 31). Additionally, the smaller corrections between the observed and computed SLR range (O-C) and the resulting residuals support this statement.

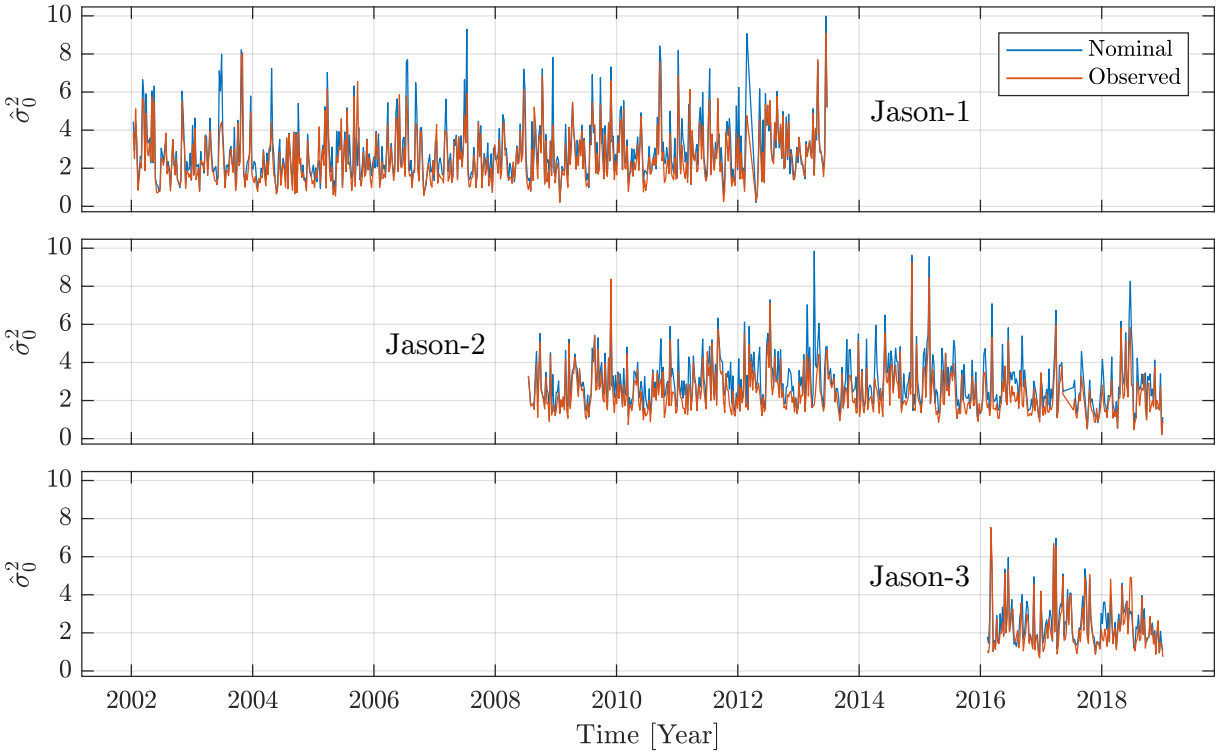

Figure 31: A posteriori variance factors resulting from the estimation of SLR station coordinates based on the nominal and observation-based determined orbit.

6 Conclusion and outlook

In this thesis, the differences in the attitude realization in the POD of the Jason satellites are investigated and the influences on satellite orbits and derived geodetic parameters are quantified and discussed. Therefore, satellite attitude information composed of attitude quaternions of the spacecraft body and rotation angles of the solar arrays is used in contrast to a defined nominal yaw steering model. The daily provided data is combined to weekly attitude files containing the full information about the satellite orientation at each time. The orientation data preprocessing includes the elimination of outliers, a temporal resampling of intervals containing high frequency sampled observations and the optimal interpolation of missing data.

Based on SLR observations of the Jason satellites over a timespan of approximately 25 years, precise orbits of the satellites are computed. The orbit determination comprises a gross and refined outlier detection as well as the removal of maneuvers by splitting the orbital arcs. The resulting orbits are subsequently recalculated using either the nominal yaw steering model for the Jason satellites or observation-based attitude information.

Both orbit solutions are internally compared according to the change of the arc-wise RMS of SLR fits and the overall mission RMS. The improvement of the SLR RMS fits from nominal to observation-based is 5.93 % (Jason-1), 8.27 % (Jason-2) and 4.51 % (Jason-3). The estimated parameters (such as atmospheric drag and Earth albedo scaling factors) within the POD of the nominal and observation-based orbits are investigated concerning the difference to the target values. Mismodelling of these parameter results in draconitic periods in the signal.

Both DGFI-TUM orbit realizations are validated with external solution of GFZ and CNES in the orbital system (along-track, cross-track, radial). GFZ and CNES orbits are based on a combination of SLR and continuously measuring tracking techniques. The standard deviations of the component-wise orbit differences are reduced on average by about 10 % using observation-based DGFI-TUM orbits.

Furthermore, the impact of both orbit solutions on estimated SLR station coordinates is investigated. Orbit specific periods (draconitic period and its harmonics of the Jason satellites) are reduced in the station coordinates using the observation-based satellite orbits. This allows a better separation of geophysical station displacements and station motions caused by uncertainties in the satellite orbits.

Despite of the extensive analysis of the observed satellite attitude data, the obtained results using real attitude information are clearly better than utilizing models describing an intentional orientation. While the nominal model in general defines the long-wavelength behavior of the satellite, observation-based data benefits the consideration of short-wave signals in the satellite orbit. The usage of the actual attitude information allows a much more accurate determination of the perturbing forces. Hence, the calculated satellite position is closer to the actual position and the differences between the observed and computed SLR observations are smaller.

Furthermore, two aspects potentially benefit the altimetry measurements: First, an improved satellite attitude corrects the position of the onboard altimeter in the CRF. This implies an improvement of the measured altimetry range. Additionally, the pointing and consequently the georeferencing of the altimeter measurement footprint is

more precise. It can be assumed that the altimetric measurements benefit in a similar way the station coordinates do.

The potentially enhanced altimetry measurements can be used for the recalculation of products such as sea surface topography, significant wave heights and ocean tides. Using corrected measurements should clearly increase the reliability of the mean observed global and local sea level change.

In this thesis, only SLR observations are used for the computation of the satellite orbits. In future investigations, a combination of all three geodetic tracking techniques for the orbit determination should be evaluated. DORIS and GNSS provide a considerably larger number of satellite observations. Thus, the benefit of using attitude observation data in combination with these tracking techniques should be compared to the SLR-only results. To quantify the enhancement of the observation-based attitude approach at different orbit geometries, the investigation should be extended for other satellite missions. Therefore, the preprocessed observation data and the experience in data processing might be useful for other institutes.

The implementation of the observation-based attitude realization for GNSS and DORIS satellites is a currently discussed topic in this year's workshops of the IDS and the International GNSS Service (IGS)[30, 31]. This illustrates the contemporary objective of this thesis.

The improved orbits might benefit other scientific disciplines, too. At DGFI-TUM, the improved orbits should be used in altimetry research area for the computation of global sea level products. The corrected time series of station coordinates can be used to improve geophysical models. The combination of multiple satellite orbits allows to investigate the impact of the observation-based orbits on further derived uncorrelated geodetic parameters such as EOPs and coefficients of the Earth's gravity field model. Finally, beneficial or adverse effects on the TRF can be further discussed.

At the beginning of this thesis, the research question

> **Are attitude observations helpful to further improve the precise orbit determination of near-Earth satellites?**

was raised. Based on the findings of the prior described investigation, it can be clearly stated that attitude observations help to further improve the precise orbit determination. Moreover, in this thesis, it was shown that an enhanced satellite attitude handling entails an improvement of the POD and further beneficially effects derived geodetic or geophysical parameters.

[30] `https://ids-doris.org/ids/reports-mails/meeting-presentations.html#ids-awg-04-2019`, Last access: 2019-06-19

[31] `http://www.acc.igs.org/workshop2019.html`, Last access: 2019-06-19

Appendices

Appendix A: Conversions between attitude parametrizations

Each parametrization of the attitude can be converted into the other parametrizations. The formula is provided in this appendix.

Direction cosine matrix to quaternion

The rotation quaternion can be calculated from a direction cosine matrix $\boldsymbol{R}$ with

$$\begin{aligned} q_s &= \pm\frac{1}{2}(1 + R_{11} + R_{22} + R_{33})^{1/2}, \\ q_x &= \frac{1}{4q_s}(R_{23} - R_{32}), \\ q_y &= \frac{1}{4q_s}(R_{31} - R_{13}), \\ q_z &= \frac{1}{4q_s}(R_{12} - R_{21}). \end{aligned} \tag{A.1}$$

Quaternion to direction cosine matrix

The quaternion elements can be used to determine the direction cosine matrix according

$$\boldsymbol{R}(\boldsymbol{q}) = \begin{bmatrix} q_s^2 + q_x^2 - q_y^2 - q_z^2 & 2(q_x q_y + q_s q_z) & 2(q_x q_z - q_s q_y) \\ 2(q_x q_y - q_s q_z) & q_s^2 - q_x^2 + q_y^2 - q_z^2 & 2(q_y q_z + q_s q_x) \\ 2(q_x q_z + q_s q_y) & 2(q_y q_z - q_s q_x) & q_s^2 - q_x^2 - q_y^2 + q_z^2 \end{bmatrix}. \tag{A.2}$$

Alternatively, the diagonal elements of the matrix can be obtained by

$$\begin{aligned} R_{11} &= 2\left(q_s^2 + q_x^2\right) - 1 = 1 - 2\left(q_y^2 + q_z^2\right), \\ R_{22} &= 2\left(q_s^2 + q_y^2\right) - 1 = 1 - 2\left(q_x^2 + q_z^2\right), \\ R_{33} &= 2\left(q_s^2 + q_z^2\right) - 1 = 1 - 2\left(q_x^2 + q_y^2\right). \end{aligned} \tag{A.3}$$

Euler angles to direction cosine matrix

The direction cosine matrix can be obtained by matrix multiplication of the three individual rotation matrices. In doing so, the rotation sequence has to be considered (see Equations 2.25 and 2.26).

Direction cosine matrix to Euler angles

The Euler angles depend on the rotation sequence and are calculated differently in each sequence. For the matrices $\boldsymbol{R}_{313}$ and $\boldsymbol{R}_{312}$ (Equations) 2.25 and 2.26, the formula is:

$\boldsymbol{R}_{313}$:

$$\phi = -\arctan\left(\frac{R_{31}}{R_{32}}\right), \quad \theta = \arccos(R_{33}), \quad \psi = \arctan\left(\frac{R_{13}}{R_{23}}\right) \tag{A.4}$$

$\boldsymbol{R}_{312}$:

$$\phi = -\arctan\left(\frac{R_{21}}{R_{22}}\right), \quad \theta = \arcsin(R_{23}), \quad \psi = \arctan\left(\frac{R_{13}}{R_{33}}\right) \tag{A.5}$$

Direction cosine matrix to Euler axis and angle

The Euler angle θ is expressed by the elements of the direction cosine matrix $\boldsymbol{R}$ by

$$\cos\theta = \frac{1}{2}[tr(\boldsymbol{R}) - 1], \tag{A.6}$$

where $tr(\boldsymbol{R})$ denotes the trace of matrix $\boldsymbol{R}$ (sum of the diagonal elements).

The formula for the Euler axis $\boldsymbol{e}$ is

$$e_1 = \frac{R_{23} - R_{32}}{2\sin\theta}, \quad e_2 = \frac{R_{31} - R_{13}}{2\sin\theta}, \quad e_3 = \frac{R_{12} - R_{21}}{2\sin\theta}. \tag{A.7}$$

It is required that $\sin\theta \neq 0$. Equation $\cos\theta = \frac{1}{2}[tr(\boldsymbol{R}) - 1]$ yields two solutions for the Euler angle, which have a different sign. Using both solutions, θ and $-\theta$, result in the Euler axes $\boldsymbol{e}$ and $-\boldsymbol{e}$, respectively. Both rotations are equivalent to each other.

Euler axis and angle to direction cosine matrix

The Euler axis and angle can be represented as direction cosine matrix as in Equation 2.9.

Appendix B: Examples for the rotation with direction cosine matrices and quaternions

This appendix provides examples for a vector rotation for both using a direction cosine matrix and a rotation quaternion. Furthermore, a composed quaternion rotation is given.

Example 1: Rotation with a direction cosine matrix

$$\boldsymbol{v}_I = \begin{bmatrix} 1 \\ 2 \\ 3 \end{bmatrix} \tag{A.8}$$

$$\boldsymbol{R}_I^B(\theta) = \begin{bmatrix} \cos\theta & 0 & -\sin\theta \\ 0 & 1 & 0 \\ \sin\theta & 0 & \cos\theta \end{bmatrix}, \quad \theta = 90^\circ \tag{A.9}$$

$$\boldsymbol{v}_B = \boldsymbol{R}_I^B \boldsymbol{v}_I = \begin{bmatrix} 0 & 0 & -1 \\ 0 & 1 & 0 \\ 1 & 0 & 0 \end{bmatrix} \begin{bmatrix} 1 \\ 2 \\ 3 \end{bmatrix} = \begin{bmatrix} -3 \\ 2 \\ 1 \end{bmatrix} \tag{A.10}$$

Example 2: Rotation with a rotation quaternion

Using the formula from Appendix A

$$\boldsymbol{v}_I = \begin{bmatrix} 0 \\ 1 \\ 2 \\ 3 \end{bmatrix} \tag{A.11}$$

$$\begin{aligned} q_s &= \pm\frac{1}{2}(1 + A_{11} + A_{22} + A_{33})^{1/2} = \sqrt{\frac{1}{2}}, \\ q_x &= \frac{1}{4q_s}(A_{23} - A_{32}) = 0, \\ q_y &= \frac{1}{4q_s}(A_{31} - A_{13}) = \sqrt{\frac{1}{2}}, \\ q_z &= \frac{1}{4q_s}(A_{12} - A_{21}) = 0. \end{aligned} \tag{A.12}$$

$$\boldsymbol{q}_I^B = \sqrt{\frac{1}{2}} \begin{bmatrix} 1 \\ 0 \\ 1 \\ 0 \end{bmatrix} \tag{A.13}$$

$$\boldsymbol{v}_B = \boldsymbol{q}_I^B \circ \left(\boldsymbol{v}_I \circ \boldsymbol{q}_I^{B*}\right) = \sqrt{\frac{1}{2}}\begin{bmatrix}1\\0\\1\\0\end{bmatrix} \circ \left(\begin{bmatrix}0\\1\\2\\3\end{bmatrix} \circ \sqrt{\frac{1}{2}}\begin{bmatrix}1\\0\\-1\\0\end{bmatrix}\right) = \begin{bmatrix}0\\-3\\2\\1\end{bmatrix}, \tag{A.14}$$

where $\circ$ implies a quaternion multiplication.

Example 3: Composed rotation quaternion $\boldsymbol{q}$ of two consecutive rotations $\boldsymbol{q}_1$ and $\boldsymbol{q}_2$

Let a composed rotation of direction cosine matrices be

$$\boldsymbol{R} = \boldsymbol{R}_1\boldsymbol{R}_2 = \begin{bmatrix}\cos\theta & 0 & -\sin\theta\\ 0 & 1 & 0\\ \sin\theta & 0 & \cos\theta\end{bmatrix}\begin{bmatrix}\cos\theta & \sin\theta & 0\\ -\sin\theta & \cos\theta & 0\\ 0 & 0 & 1\end{bmatrix} = \begin{bmatrix}0 & 0 & -1\\ -1 & 0 & 0\\ 0 & 1 & 0\end{bmatrix}, \tag{A.15}$$

with $\theta = 90°$.

The equivalent composed quaternion rotation performed with

$$\boldsymbol{q}_1 = \sqrt{\frac{1}{2}}\begin{bmatrix}1\\0\\1\\0\end{bmatrix} \text{(Rotation about y axis)}, \quad \boldsymbol{q}_2 = \sqrt{\frac{1}{2}}\begin{bmatrix}1\\0\\0\\1\end{bmatrix} \text{(Rotation about z axis)} \tag{A.16}$$

is

$$\boldsymbol{q} = \boldsymbol{q}_1 \circ \boldsymbol{q}_2 = \sqrt{\frac{1}{2}}\begin{bmatrix}1\\0\\1\\0\end{bmatrix} \circ \sqrt{\frac{1}{2}}\begin{bmatrix}1\\0\\0\\1\end{bmatrix} = \frac{1}{2}\begin{bmatrix}1\\-1\\1\\1\end{bmatrix}. \tag{A.17}$$

Appendix C: Flowchart of the attitude processing program

The following Figure 32 shows the flowchart of the MATLAB-based program which is described in Chapter 4.2 and processes the generation of GPS-weekly attitude files for the Jason satellites.

The user first defines the variables *satellite*, *gpsWeek*, *gpsDays* and *gapTol*. *gpsDays* indicates the number of days which are included in the GPS week. The minimum is seven days and the number must be odd. Consequently, nine days result in an additional day before and after the GPS week. *gapTol* defines the amount of seconds which represent a gap in the data. In these gaps no interpolation is performed due to increased interpolation errors.

The input parameters are subsequently validated (`fkt_checkInput()`). In case of not correctly defined variables, the program stops.

For all asigned GPS weeks, the following tasks are executed: first, the respective data is loaded (`fkt_loadData()`). This step contains the determination of the dates of all available quaternion and solar panel angle files. Furthermore, the first day of the pending GPS week (`fkt_findDayStart()`) and the associated body and solar panel files (`fkt_findFileStart()`) are investigated. The data is imported by the function `fkt_readFiles()`.

If no files or no data is provided for the GPS week, an error is thrown (`fkt_error()`) and the next GPS week will be processed.

The second step analyzes the separate data sets according to several aspects (`fkt_dataAnalysis()`):

1. Double epochs are eliminated,
2. Invalid data is discarded,
3. Outliers are eliminated (these are imported in user-defined files),
4. Quaternions differing from the norm 1 are discarded,
5. Intervals of high observation rate are temporally resampled (`fkt_highSampleRate()`),
6. Data within gaps of the other data set is deleted (`fkt_deleteGaps()`),
7. Missing epochs in one data set with respect to the other one are determined,
8. Neighbours of missing epochs in resampled intervals are extracted for accurate interpolation (`fkt_getHRFneighbours()`) and
9. Chronological arrangement of the data sets for correct interpolation.

Afterwards, the missing epochs in quaternions (`fkt_interpBody()`) and solar panel angles (`fkt_interpSolp()`) are interpolated, both data sets are combined (`fkt_arrangeData()`), and an output file is generated for the satellite attitude of the GPS week. For the format of the output files, see Appendix D.

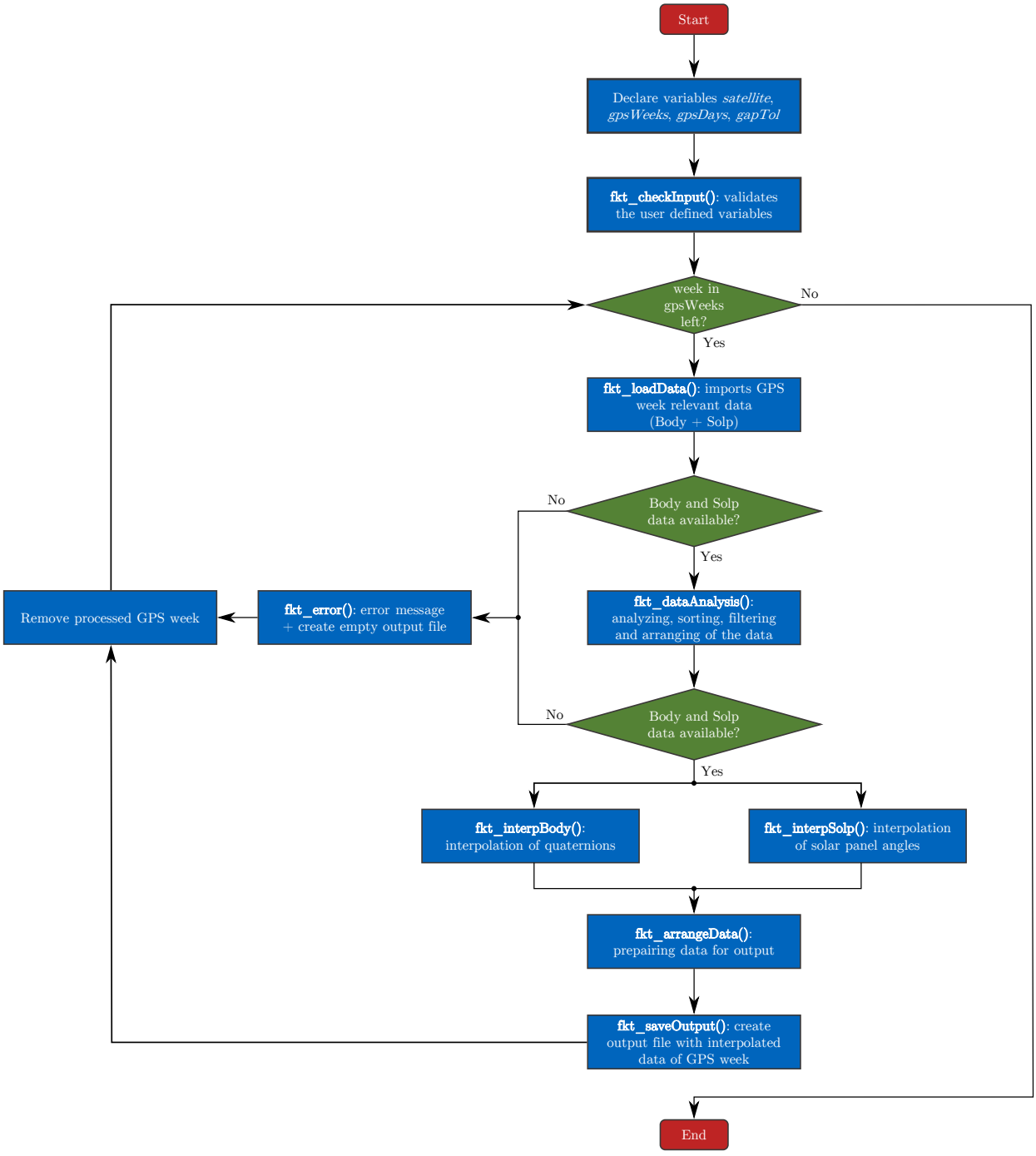

Figure 32: Flowchart of the program which is creating combined GPS week-based attitude files.

Appendix D: Output data format

This appendix lists detailed information about the content of the weekly provided attitude files. In total nine columns are given which are separated by a space character. Table 16 shows the data format. F marks a floating-point number and I an integer number. A blank space is inserted between two columns.

Table 16: Format description of GPS week-based attitude files.

Column 1	F17.10	Time [days since J2000.0]
Column 2	F11.6	Scalar part q_s of the attitude quaternion
Column 3−5	F11.6	Vector part $\boldsymbol{q}_v$ (q_x, q_y, q_z) of the attitude quaternion
Column 6+7	F11.6	Rotation angle of the left and right solar panel array [radians]
Column 8	I1	Interpolation flag 0 Both quaternion and rotation angles are existing 1 Quaternion is interpolated 2 Solar panel angles are interpolated
Column 9	I7	ILRS satellite ID Jason-1 0105501 Jason-2 0803201 Jason-3 1600201

The ILRS ID is composed of the last two digits of the launch-vehicle launch year, a launch vehicle number in that year (3 digits), and a 2-digit payload sequence number for the specific launch. The ILRS ID originates from the international designator (COSPAR designator), a satellite specific designation of the UN Committee on Space Research (COSPAR). The COSPAR designator contains the launch year, a 3-digit year relating launch number and an up to 3-letter code specifying the type of the object.

Example (spaces are visualized by 'X'):

```
XX3094.2575192363XXXX0.671346XXXX0.259941XXXX0.023411XXX-0.693670XXX-0.017193XXXX0.017192X1X0803201
```

Appendix E: SLR station network

Figure 33 shows the map of all SLR stations available for the calculation of Jason orbits between 2002 and 2018.

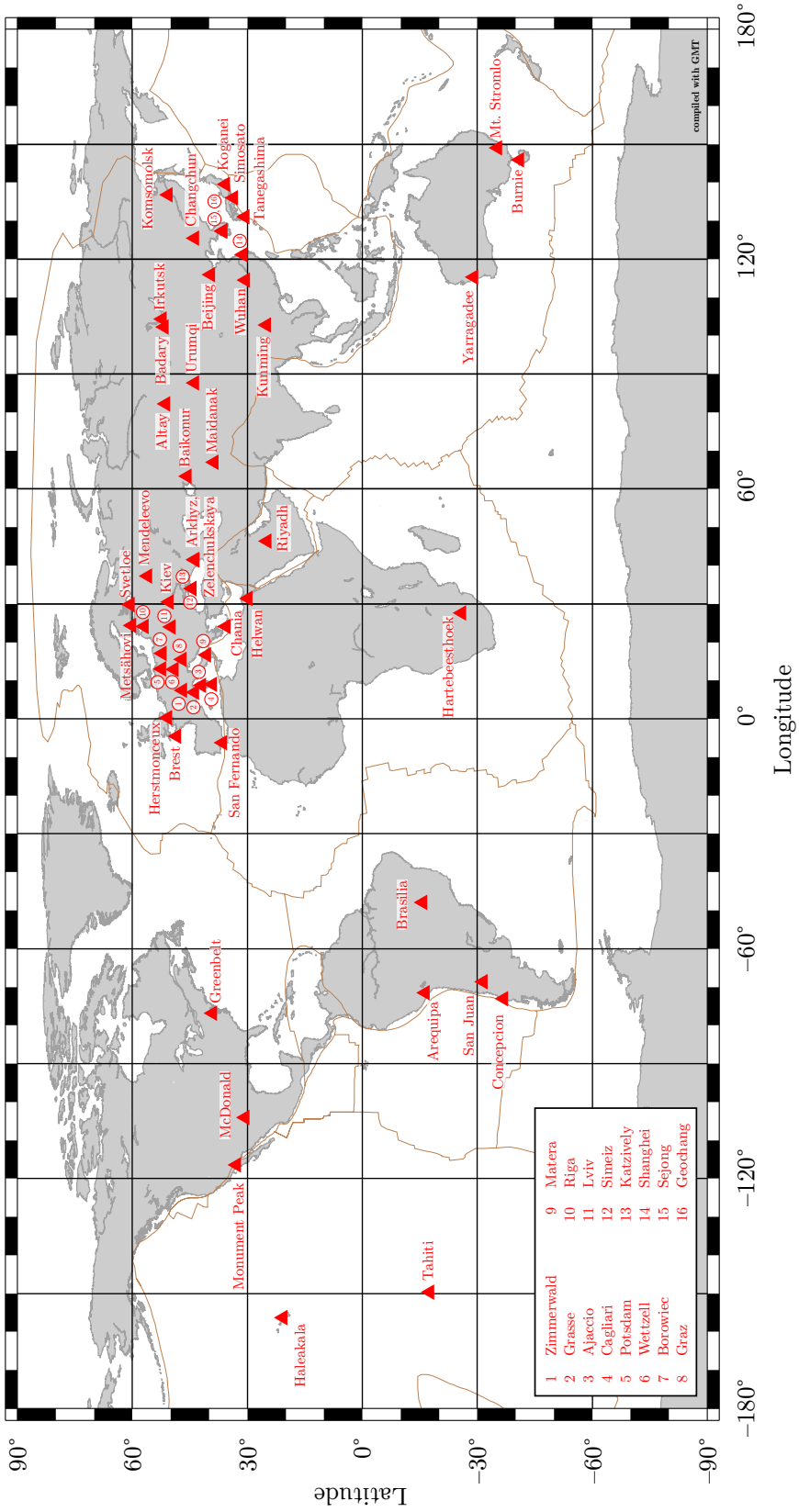

Figure 33: Available SLR station network for the determination of Jason orbits.

Appendix F: Jason-1 satellite configuration

Figure 34 shows the deployed configuration of Jason-1 satellite[32].

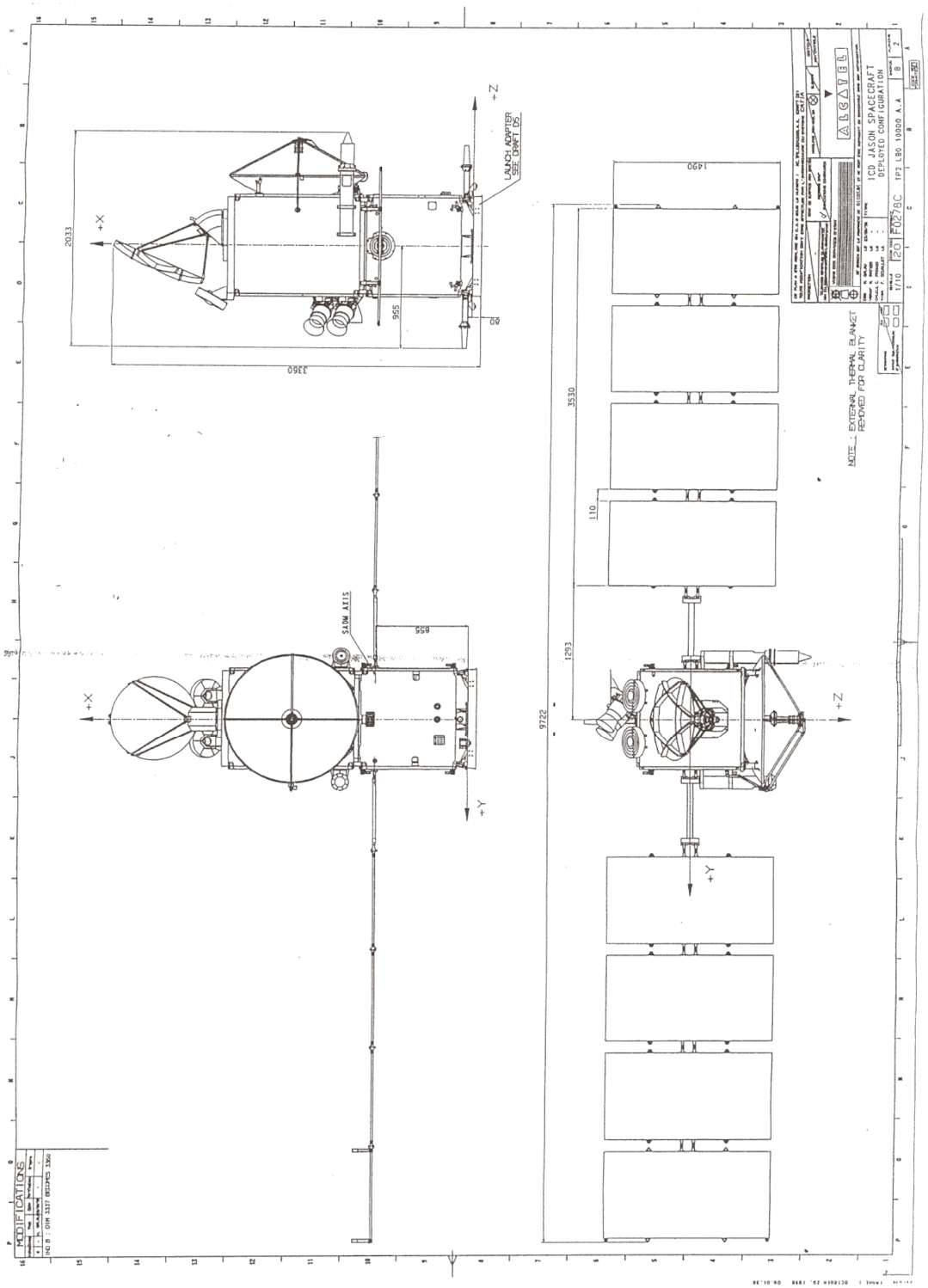

Figure 34: Deployed Jason-1 satellite configuration. The dimensions of the spacecraft are provided in the satellite reference system (in this thesis denoted as X_{SAT}, Y_{SAT} and Z_{SAT}). The origin of the coordinate system is the center of the attachment ring.

[32] IDS documentation: Modelling of DORIS 2GM instruments, CNES, Available online at `ftp://ftp.ids-doris.org/pub/ids/satellites/DORIS_instrument_modelling_2GM.pdf`

List of Abbreviations

AMR	Advanced Microwave Radiometer	27
AMR-2	Advanced Microwave Radiometer-2	27
Carmen-2	Environment Characterization and Modelisation-2	29
CNES	Centre National D'Etudes Spatiales	25--29, 35, 40, 43, 44, 47, 51, 52, 57, 73, I, III
CoM	Center of Mass	4, 24, 26, 40
COSPAR	Committee on Space Research	65
CRF	Celestial Reference Frame	43, 57
CRS	Celestial Reference System	7, 24
DCM	Direction Cosine Matrix	9
DGFI-TUM	Deutsches Geodätisches Forschungsinstitut	23, 38, 39, 41, 43, 44, 48, 51--54, 57, 58, 73, 74, III
DOGS	DGFI Orbit and Geodetic Parameter Estimation Software	38
DOGS-CS	Combination and Solution library of DOGS	38, 44
DOGS-OC	Orbit Computation library of DOGS	38--40, 42, 44, 47, 73, 74
DOGS-RI	Radio Interferometry library of DOGS	38
DORIS	Doppler Orbitography by Radiopositioning Integrated on Satellite	28, 29, 43, 52, 58
DTRF	DGFI-TUM Terrestrial Reference Frame	45
EOP	Earth Orientation Parameter	22, 24, 39, 43--45, 58
EUMETSAT	European Organization for the Exploitation of Meteorological Satellites	27
FK5	Fifth Fundamental Catalogue	4
GCRS	Geocentric Celestial Reference System	4, 7, 35, 40
GDR	Geophysical Data Record	27
GFZ	GeoForschungsZentrum Potsdam	43, 44, 47, 51, 52, 57, 73, 74, I, III

GNSS	Global Navigation Satellite System	6, 28, 43, 58
GPS	Global Positioning System	28, 29, 35, 38, 43, 44, 52, 63--65, 73, 74
GPSP	Global Positioning System Payload	28
IAU	International Astronomical Union	4
ICRS	International Celestial Reference System	3, 4
ID	Identifier	65
IDS	International DORIS Service	32, 58
IERS	International Earth Rotation and Reference Systems Service	4, 39, 40
IGS	International GNSS Service	58
ILRS	International Laser Ranging Service	22, 40, 41, 65
J2000.0	Modified Julian Date timescale starting January 1, 2000, $12^h\ 0^m\ 0^s$ TDB	4, 35, 36, 65
Jason	Joint Altimetry Satellite Oceanography Network	25
JAXA	Japan Aerospace Exploration Agency	29
JD	Julian Date	4
JMR	Jason-1 Microwave Radiometer	27
JPL	Jet Propulsion Laboratory	28
LPT	Light Particle Telescope	29
LRA	Laser Retroreflector Array	6, 24, 28
LRO	long-repeat orbit	34
NASA	National Aeronautics and Space Administration	25, 27, 28
NEQs	Normal Equations	44, 45
NNR	No-Net-Rotation	45
NOAA	National Oceanic and Atmospheric Administration	27
OSTM	Ocean Surface Topography Mission	25
POD	Precise Orbit Determination	1, 28, 40, 42, 50, 57, 58, 73, 74, I
PROTEUS	Plate-forme Reconfigurable pour l'Observation, les Télécommunications Et les Usages Scientifiques	26
RMS	Root Mean Square	42, 47--49, 57, 73, 74, I
SAA	South American Anomaly	29

SHM	Safehold Mode	27, 34, 36, 41
SLERP	Spherical Linear Quaternion Interpolation	17, 18, 38
SLR	Satellite Laser Ranging	2, 3, 22--24, 28, 29, 35, 38, 40--43, 45, 47--49, 51--55, 57, 58, 66, 72--74, I, III
SLRF	Satellite Laser Ranging Frame	39, 49
SP3c	Standard Product 3 format, Version c	43
SSH	Sea Surface Height	27
T2L2	Time Transfer by Laser Link	29
TAI	Temps Atomique International (engl.: International Atomic Time)	43
TDB	Temps Dynamique Barycentrique (engl.: Barycentric Dynamical Time)	4, 70
TOPEX	Topography Experiment	25, 30, 31, 33, 34
TRF	Terrestrial Reference Frame	22--24, 28, 43, 45, 58
TRSR	Turbo Rogue Space Receiver	28
UN	United Nations	65
USO	Ultra Stable Oscillator	29
UT	Universal Time	35
UTC	Temps universel coordonné (engl.: Coordinated Universal Time)	4, 35, 36, 43, 44, 74
VLBI	Very Long Baseline Interferometry	3

List of Figures

List of Tables

Bibliography

Arias E. F., Charlot P., Feissel M., Lestrade J.-F. (1995) The Extragalactic Reference System of the International Earth Rotation Service, ICRS. In: Astronomy and Astrophysics 303, pp. 604–608

Biancale R., Bode A. (2006) Mean annual and seasonal atmospheric tide models based on 3-hourly and 6-hourly ECMWF surface pressure data. GeoForschungsZentrum (GFZ) Scientific Technical Report STR06/01, DOI: 10.2312/GFZ.b103-06011

Bloßfeld M., Gerstl M., Hugentobler U., Angermann D., Müller H. (2014) Systematic effects in LOD from SLR observations. In: Advances in Space Research 54, pp. 1049–1063, DOI: 10.1016/j.asr.2014.06.009

Bloßfeld M. (2015) The key role of Satellite Laser Ranging towards the integrated estimation of geometry, rotation and gravitational field of the Earth. Ph.D thesis, Deutsche Geodätische Kommission (DKG) Reihe C, No. 745, Verlag der Bayerischen Akademie der Wissenschaften, ISBN: 978-3-7696-5157-7

Bloßfeld M., Rudenko S., Kehm A., Panafidina N., Müller H., Angermann D., Hugentobler U., Seitz M. (2018) Consistent estimation of geodetic parameters from SLR satellite constellation measurements. In: Journal of Geodesy, 92(9), 1003–1021, DOI: 10.1007/s00190-018-1166-7

Bronner E., Dibarboure G. (2012) Technical Note about the Jason-1 Geodetic Mission. CNES, JPL. Ref: SALP-NT-MA-EA-16267-CNv1.0. Available online at `ftp://podaac.jpl.nasa.gov/allData/jason1/L2/docs/Technical_Note_J1_Geodetic_Mission.pdf`, Last access: 2019-06-19

Bowman B. R., Tobiska W. K., Marcos F. A., Huang C. Y., Lin C. S., Burke W. J. (2008) A new empirical thermospheric density model JB2008 using new solar and geomagnetic indices. AIAA/AAS Astrodynamics Specialist Conference, AIAA 2008-6438, Honolulu, Hawaii, DOI: 10.2514/6.2008-6438

Bronstein N. I., Semendjajew K. A., Musiol G., Mühlig H. (2013) Taschenbuch der Mathematik. Eighth edition, Haan-Gruiten: Verlag Europa-Lehrmittel, ISBN: 978-3-8085-5673-3

Cerri L., Couhert A., Ferrage P. (2019) DORIS satellites models implemented in POE processing. First edition, 14th review, Ref.: SALP-NT-BORD-OP-16137-CN. Available online at `ftp://ftp.ids-doris.org/pub/ids/satellites/DORISSatelliteModels.pdf`, Last access: 2019-06-19

Cerri L., Berthias J. P., Bertiger W. I., Haines B. J., Lemoine F. G., Mercier F., Ries J. C., Willis P., Zelensky N. P., Ziebart M. (2010) Precision Orbit Determination Standards for the Jason Series of Altimeter Missions. In: Marine Geodesy 33 (S1), pp. 379–418. DOI: 10.1080/01490419.2010.488966

Dam E. B., Koch M., Lillholm M. (1998) Quaternions, Interpolation and Animation. Technical Report, Copenhagen (Department of Computer Science, University of Copenhagen). Available online at `http://web.mit.edu/2.998/www/QuaternionReport1.pdf`, Last access: 2019-06-19

Desai S. D. (2002) Observing the pole tide with satellite altimetry. In: Journal of Geophysical Research 107(C11):7-1-7-13, DOI: 10.1029/2001JC001224

Doornbos E. (2011) Thermospheric Density and Wind Determination from Satellite Dynamics. ISBN: 978-90-9026051-8

Ferrage P., Guinle T. (2009) Jason1&2 / Descriptions of the Quaternion and Solar Panel Files. CNES, Ref: SALP-IF-M/IDS-EA-15938-CN. Available online at `ftp://ftp.ids-doris.org/pub/ids/ancillary/`

quaternions/jason1_2_quaternion_solar_panel.pdf, Last access: 2019-06-19

Folkner W. F., Willimas J. G., Boggs D. H. (2008) Planetary ephemeris DE421 for Phoenix navigation. IOM 343R-08-002

Förste C., Bruinsma S., Shako R., Marty J. C., Flechtner F., Abrikosov O., Dahle C., Lemoine J. M., Neumayer K. H., Biancale R., Barthelmes F., König R., Balmino G. (2011) EIGEN-6 - A new combined global gravity field model including GOCE data from the collaboration of GFZ-Potsdam and GRGS-Toulouse. In: Geophysical Research Abstracts 13, EGU2011-3242-2, European Geosciences Union General Assembly 2011

Großekatthöfer K, Yoon Z. (2012) Introduction into quaternions for spacecraft attitude representation. Berlin (Department of Astronautics and Aeronautics, Technical University of Berlin). Available online at http://www.tu-berlin.de/fileadmin/fg169/miscellaneous/Quaternions.pdf, Last access: 2019-06-19

Knocke P. C., Ries J. C., Tapley B. D. (1988) Earth radiation pressure effects on satellites. AIAA/AAS Astrodynamics Conference, AIAA 88-4292, Minneapolis, Minnesota, DOI: 10.2514/6.1988-4292

Konopliv A. S., Asmar S. W., Carranza E., Sjogren W. L., Yuan D.-N. (2001) Recent gravity models as a result of the Lunar Prospector Mission. In: Icarus 150(1):1-18, DOI: 10.1006/icar.2000.6573

Kramer H. J. (2002) Observation of the Earth and Its Environment. Survey of Missions and Sensors. Fourth edition, In: Engineering Online Library, Berlin Heidelberg New York: Springer-Verlag, ISBN: 3-540-42388-5

Markley F. L., Crassidis J. L. (2014) Fundamentals of Spacecraft Attitude Determination and Control. In: Space technology library 33, New York: Springer-Verlag, ISBN: 978-1-4939-0801-1

Mathews P. M., Herring T. A., Buffett B. A. (2002) Modelling of nutation and precession: New nutation series for nonrigid Earth, and insights into the Earth's Interior. Journal of Geophysical Research, 107(B4), DOI: 10.1029/2001JB000390

Mendes V. B., Pavlis E. C. (2004) High-accuracy zenith delay prediction at optical wavelengths. In: Geophysical Research Letters 31:L14602, DOI: 10.1029/2004GL020308

Montenbruck O, Gill E. (2012) Satellite orbits - Models, Methods and Applications. Fourth edition, Berlin Heidelberg New York: Springer-Verlag, ISBN: 978-3-540-67280-7

Panzetta F., Bloßfeld M, Erdogan E., Rudenko S., Schmidt M., Müller H. (2018) Towards thermospheric density estimation from SLR observations of LEO satellites: a case study with ANDE-Pollux satellite. In: Journal of Geodesy 93(3), DOI: 10.1007/s00190-018-1165-8

Pearlman M. R., Degnan J. J., Bosworth J. M. (2002) The international laser ranging service. In: Advances in Geosciences 30(2), pp. 135-143, DOI: 10.1016/S0273-1177(02)00277-6

Perrygo C. (1987) TOPEX satellite yaw maneuvers. IOC 968:SE:87-074, Germantown, Maryland: Fairchild Space Company

Petit G., Luzum B. (2010) IERS Conventions (2010). IERS Technical Note 36, International Earth Rotation and Reference Systems Service (IERS), Frankfurt am Main: Verlag des Bundesamts für Kartographie und Geodäsie, ISBN: 3-89888-989-6

Ray R. D., Ponte R. M. (2003) Barometric tides from ECMWF operational analysis. In: Annales Geophysicae 21:1897-1910, DOI: 10.5194/angeo-21-1897-2003

Ray R. D., Steinberg D. J., Chao B. F., Cartwright D. E. (1994) Diurnal and semidiurnal variations in the Earth's rotation rate induced by oceanic tides. In: Science, 264(5160), pp. 830-832, DOI: 10.1126/science.264.5160.830

Rudenko S., Schöne T., Esselborn S., Neumayer K. H. (2018) GFZ VER13 SLCCI precise orbits of altimetry satellites ERS-1, ERS-2, Envisat, TOPEX/Poseidon, Jason-1, and Jason-2 in the ITRF2014 reference frame.

GFZ Data Services, DOI: 10.5880/GFZ.1.2.2018.003

Savcenko R., Bosch W. (2012) EOTI11A-Empirical Ocean Tide model from multi-mission satellite altimetry. Report No. 89, Munich (Deutsches Geodätisches Forschungsinstitut (DGFI), Technical University of Munich)

Seeber G. (2003) Satellite Geodesy - Foundations, methods, and applications. Second completely revised and extended edition, Berlin, New York: de Gruyter, ISBN: 3-11-017549-5

Seitz M., Bloßfeld M., Angermann D., Schmid R., Gerstl M., Seitz F. (2016) The new DGFI-TUM realization of the ITRS: DTRF2014 (data). Deutsches Geodätisches Forschungsinstitut, Munich, DOI: 10.1594/PANGAEA.864046

Stammer D., Cazenave A. (2017) Satellite Altimetry Over Oceans and Land Surfaces. Boca Raton, London, New York: CRC Press Taylor & Francis Group (Earth Observation of Global Changes), ISBN: 9781498743457

Svehla D., Rothacher M. (2003) Kinematic and reduced-dynamic precise orbit determination of low earth orbiters. In: Advances in Geosciences, European Geosciences Union 2003(1), pp. 47-56. HAL Id: hal-00297368

Taff L. G. (1985) Celestial Mechanics. A Computational Guide for the Practitioner. New York: Wiley, ISBN: 0471893161

Urban S. E., Seidelmann, P. K. (Ed.) (2012) Explanatory Supplement to the Astronomical Almanac. Third edition, Mill Valley, California: Univ. Science Books, ISBN: 978-1891389856

Vallado D. A., McClain W. D. (2007) Fundamentals of Astrodynamics and Applications. Third edition, 1st print, In: Space technology library 21, Hawthorne, California: Microcosm Press, ISBN: 978-1881883142

Wertz J. R. (2002) Spacecraft Attitude Determination and Control. Reprint, In: Astrophysics and Space Science Library 73, Computer Sciences Corporation, Dordrecht: Kluwer Academic Publishers, ISBN: 9027712042

Xu, G. (2010) Sciences of Geodesy - I. Advances and Future Directions. Berlin Heidelberg New York: Springer-Verlag, ISBN: 978-3-642-11740-4